XUV Calibrations and Electron Background Reduction for the ROSAT Wide Field Camera

by

Stephen Richard Milward

Thesis submitted to the University of Leicester for
the degree of Doctor of Philosophy, December 1986.

X-ray Astronomy Group,
Department of Physics,
University of Leicester.

Declaration

I hereby declare that no part of this thesis has been previously submitted to this or any other university as part of the requirements for a higher degree. The work described here was conducted by the undersigned except for contributions of colleages indicated in the text.

S R Milward

S. R. Milward, November 1986.

Dedication

To my wife and family

Acknowledgements

It is a pleasure to thank my supervisor, Dick Willingale, for the advice and encouragement he was able to offer during the preparation of this thesis and during the research programme it describes. Thanks are also due to the many members of the X-ray Astronomy group and the department of physics who contributed their experience and expertise. Contributions of data and figures are acknowledged in the text, where apropriate.

I especially wish to thank John Spragg, Tony Abbey, and Dave Watson for their technical help during the experimental part of the work descibed; Martin Barstow, for his colaboration with the imaging detector measurements; George Fraser, for helpful discussions about photocathode behaviour; and Dick Willingale, for help in interpreting mirror reflectivity results.

Finally, I thank Prof. K. A. Pounds for giving me the oportunity to study at Leicester under a SERC research studentship, and Alan Wells for his guidence as manager of space projects at Leicester.

Publications

Some of the results included in this thesis are included in other publications, these are listed here and the chapter in which the work is included is indicated.

1) M. A. Barstow, G. W. Fraser, S. R. Milward; 'X-ray Instrumentation in Astronomy' J. L. Culhane, Editor, Proc. SPIE 597, 352–361. (Chapter 5)
2) S. R. Milward, M. R. Sims, R. Willingale; XUV Reflectivity Measurements on the ROSAT Wide Field Camera Mirrors. Proc. Workshop on Advanced Technology Reflectors for Space Instrumentation, June 1986. (Chapter 6)
3) R. Willingale, S. R. Milward, M. R. Sims; Performance of the ROSAT Wide Field Camera Mirrors. In preparation. (Chapter 6)

CONTENTS

Chapter 1

The ROSAT Wide Field Camera

Chapter 2

A XUV Source and Monochromator for the WFC Calibration and Testing Programme

Chapter 3

The Monochromator and Penning Source Combination

Chapter 4

The Production of a Laboratory Transfer Standard for the Measurement of WFC Detector Quantum Efficiencies

Chapter 5

The Calibration of a WFC Detector

Chapter 6

The Measurement of Mirror Reflectivities

Chapter 7

WFC Particle Background Reduction

Chapter 8

Electron Diverter Performance

Chapter 9

Conclusions and Future Work

Chapter 9

Conclusions and Future Work

CHAPTER 1

The ROSAT Wide Field Camera.

1.10 Introduction.

Astronomy in the wavelength range 1 to 100nm, covering the soft X-ray to ultraviolet regions of the electromagnetic spectrum, is impossible from ground level because the atmosphere is very strongly absorbing at these wavelengths. The reason for the opacity is that electronic transitions within atoms are stimulated by photon energies corresponding to UV light right through to X-rays. Between 1 and 100nm, therefore, astronomical observations must be made above the atmosphere which means resorting to satellite borne instrumentation if any prolonged measurement is to be made.

A consequence of the interaction of the light with matter in this part of the spectrum is that, for wavelengths less than 30nm, the refractive indicies of metals are less than one and, consequently, the reflection coefficients at normal incidence approach zero. It becomes necessary, therefore, to adopt either grazing incidence optics or multilayer interference optics for soft X-ray and XUV astronomy. Indeed, in the soft X-ray band, some considerable success has been achieved in operating telescopes using grazing incidence mirrors on the Einstein and EXOSAT observatories. This was possible because detector and filter technologies were sufficiently mature, which was not so, until recently, at longer wavelengths.

Like the atmosphere, the inter stellar medium is strongly absorbing in the XUV; recent estimates of the absorption length in the galactic plane put the limit of observable sources within a few hundreds of parsecs of the sun. It is possible, therefore, that many objects may be detectable. This is contrary to the indications of earlier attempts to assess the opacity of the inter stellar medium which suggested that XUV astronomy would be limited to very local sources.

The XUV band thus remains, with the sub-millimetre waveband, one of the few largely unexplored areas of astronomy. Those observations that have been made have either been non-imaging measurements or else have been of short duration on sounding rockets. Nevertheless, several sources have been positively indentified, these include:

i) HZ43 and Feige 24, both hot DA type white dwarfs.
ii) SS Cygni, a cataclysmic variable.

iii) Proxima Centauri, a dwarf M-type flare star.

Objects which are bright in the XUV must have black body temperatures in the range 4×10^4 to 4×10^5K, or, they must be thermal bremsstrahlung plasma sources with temperatures of 10^6 to 10^7K. Examples of candidates for black body type sources are: hot white dwarfs, O-B subdwarfs, UV stars, planetry nebula nuclei, and neutron stars. Possible thermal bremsstrahlung sources might be: supernova remnants, stellar coronae, flare stars, close accreting binaries, and the inter stellar medium.

Observations of XUV sources will thus give information, not just about the sources themselves, but about the distribution of material in the local intersteller medium and the cosmic sky background.

1.20 The ROSAT Mission.

ROSAT, short for Roentgensatellit, is a German satelite experiment due for launch in the late 1980's dedicated to X-ray astronomy (W. C. Roentgen discovered X-rays in 1895.) The main instrument on board will be the 830 mm aperture X-ray telescope (XRT) which covers the spectral range 2 keV to 0.1 keV (0.6 to 5 nm)[1]. Figure 1.20:1, reproduced from reference 1, shows the optical layout of four nested grazing incidence Wolter type I mirrors[2] 2400mm from the focal plane. Three imaging detectors are included in the focal plane, two are position sensitive proportional counters[3] and the third is a Microchannel plate (MCP) detector, the High Resolution Instrument (HRI) as used on the Einstein X-ray observatory[4].

The principal mission objective is the first all-sky survey with an imaging instrument in the XRT waveband. This will extend to fainter sources those surveys conducted with the non-imaging Uhuru and Ariel 5 satelites and the partial survey conducted by the Einstein observatory. Subsequently the observatory will undertake pointed observations of selected sources at high resolution using the HRI detector.

During the planning of the ROSAT mission, space on the satellite was made available for a guest experiment to compliment the XRT. A wide field camera operating in the waveband 6-30 nm was successfully proposed by a consortium of UK groups comprising: The University of Leicester, The Rutherford- Appleton Laboratory (RAL), Birmingham University, Imperial College of Science and Technology (ICST*), and University College London Mullard Space Science Laboratory (MSSL). The Wide Field Camera (WFC) is depicted in figure 1.20:2, it is co-aligned with the XRT axis, but is independent of the main experiment in that it has its' own thermal protection and star tracker and relies on the spacecraft only for electrical power and telemetry facilities. The WFC will provide the first all-sky survey in the XUV waveband.

*Original proposal was by University of Leicester

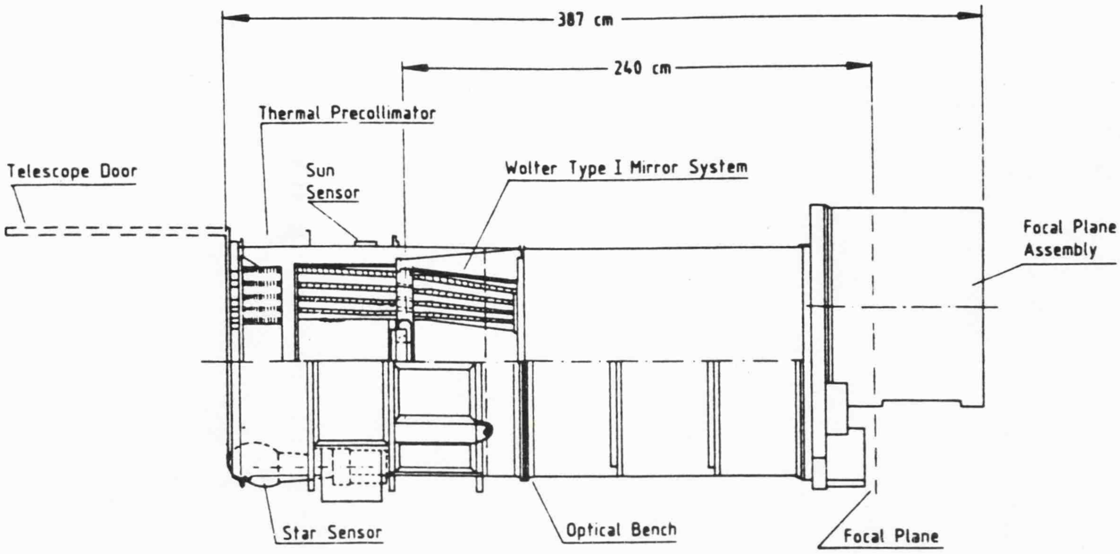

Figure 1.20:1 Section through the ROSAT XRT showing the nest of four Wolter type I grazing incidence mirrors in relation to the focal plane. From reference 1.

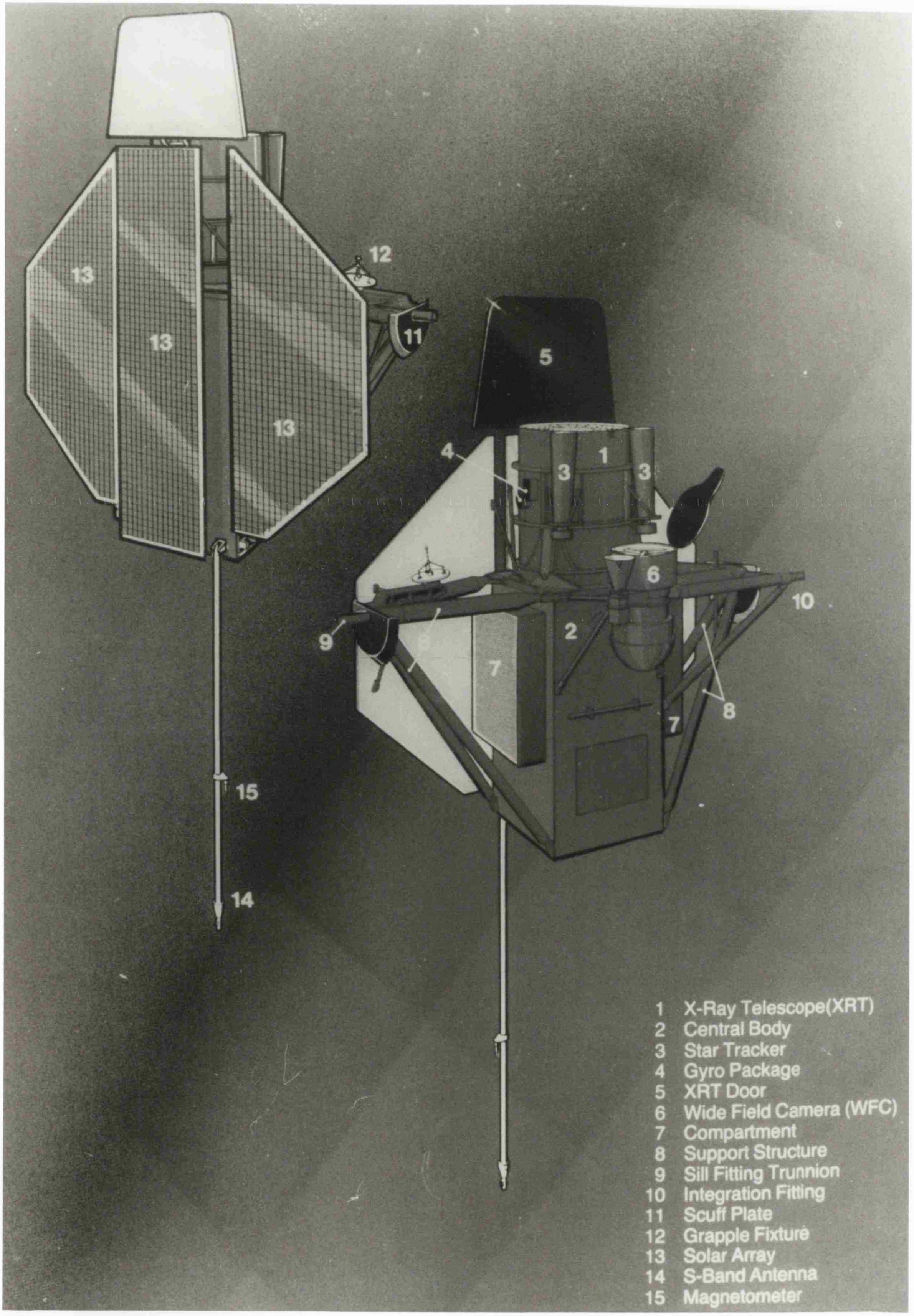

Figure 1.20:2 The WFC mounted on the ROSAT spacecraft.

1.30 The Wide Field Camera.

Figure 1.30:1a shows a cut-away drawing of the WFC on which the main components are indicated. Of these, the mirrors, filters, and detectors comprise the camera optics (figure 1.30:1b).

The grazing incidence mirrors were designed at Leicester[5], and are of Wolter-Swartzschild type 1 configuration, this design being the one that allows the largest field of view for a given overall system length. A nest of three mirrors, each comprising two reflecting surfaces, provides an enhanced collection efficiency for a given maximum mirror diameter. Each nested shell was manufactured in one piece, from a non-age hardening forged aluminium alloy, and the two reflection profiles were precision machined before being diamond turned at the Cranfield Unit of Precision Engineering (CUPE).

Diamond turning produced the Wolter-Swartzschild surfaces to within $\pm 1\mu m$ of specification with a surface finish with peak to valley variation of $0.6\mu m$ dominated by the turning marks. The mirrors were then in turn pre-lapped and nickel coated by Ferranti Astron Ltd. Further lapping and polishing, followed by gold coating lead to the finished mirrors[6].

Figure 1.30:2 is reproduced from reference 5 and shows the predicted variation of RMS blur circle radius, a measure of mirror resolution, with off-axis angle for three different focal surfaces. Of those shown, the curved focal surface, with a radius of curvature of 167mm, is clearly superior.The curved focal surface of the mirrors has lead to the development, at Leicester, of detectors fabricated from meniscus concave microchannel plates which are ceasium-iodide sensitised in the WFC waveband[7]. These detectors are discussed further in chapter 5.

Between mirrors and detectors, figure 1.30:1a shows a filter wheel carrying 8 filters of two diameters and varying thickness and composition. The larger diameter filters are for the survey phase of the mission, to enable full use of the field of view, whereas the smaller filters will be used during pointed observations when sources will occupy the centre of the field only and the instrument sensitivity will extend to 80 nm. WFC filters were designed and developed at RAL[8] and are made of layers of Lexan (a polycarbonate plastic developed by General Electric Plastics) supported on stainless steel mesh and overcoated with various materials. Table 1.30:1 shows the filter compositions and pass bands planned at the time of writing.

In addition to the WFC optics described above, several other systems are essential for the effective use of the instrument. The Protection and Calibration System (PCS), for example, serves to protect the sensitive MCP detectors from operation in high particle background regions.

Development of the PCS has been the task of ICST, it consists of two particle detectors pointing in the direction of observation: one Geiger-Muller tube sensitive to electrons of energy greater than about

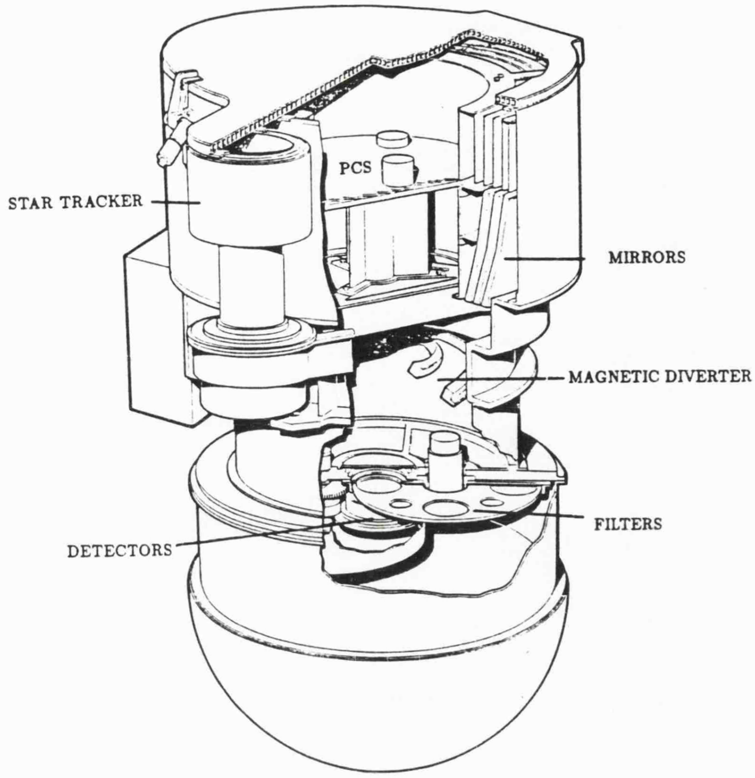

Figure 1.30:1a A cut-away drawing of the WFC showing its principal elements. From reference 11.

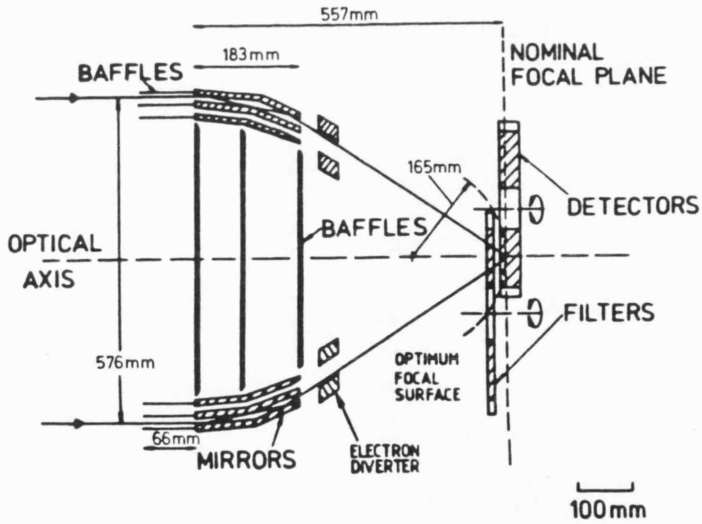

Figure 1.30:1b Schematic diagram of the WFC showing the main optical components. From reference 11.

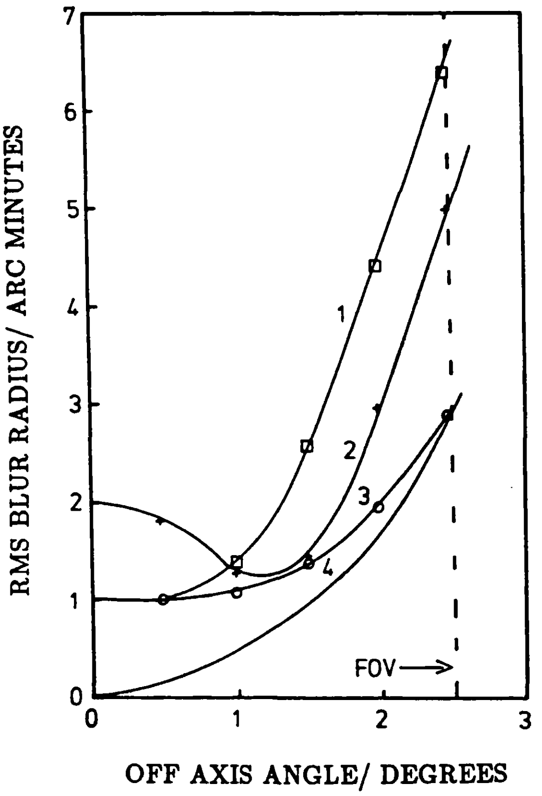

Figure 1.30:2 The variation of RMS blur-circle radius with off-axis angle. From reference 8.

Filter	Mode	Materials	Approximate bass band (f.w.h.m.)
1	Calibration	Spectrosil, aluminium narrow band interference filter	1710–1940 Å
2	Survey	3000 Å Lexan + 2000 Å carbon	70–112 Å
3	Pointed	500 Å Lexan + 2000 Å tin†	550–800 Å
4	Survey	5000 Å Lexan + 2000 Å carbon	70–112 Å
5	Pointed	MgF_2, aluminium narrow band interference filter	1300–1750 Å
6	Survey	2000 Å Lexan + 9000 Å beryllium	112–130 Å
7	Pointed	2000 Å Lexan + 1500 Å aluminium	170–210 Å
8	Survey	3000 Å Lexan + 9000 Å beryllium	112–130 Å

† Filter for which thicknesses of components are as yet uncertain.

TABLE 1.30:1 WFC Filter Materials and Pass Bands.

50 keV and a Channel Electron Multiplier (CEM) to detect softer particles. These detectors enable the WFC on-board computer to shut off the MCP high voltage when the WFC enters an area of high background. Protection of MCP detectors from excessive count rates prevents premature gain loss, as is discussed more fully in chapter 7.

The calibration role of the PCS is performed by a pair of quartz-enveloped mercury lamps which provide ultraviolet light with which to stimulate the detectors, via the calibration filter included on the filter wheel (table 1.30:1), enabling detector performance to be monitored.

In addition to the PCS, further electron background protection is afforded by a magnetic screen, studied jointly at ICST and Leicester, this is considered in chapters 7 and 8.

The star tracker illustrated in figure 1.30:1a is essentially a wide field camera in miniature operating in the visible part of the spectrum. Its function is to provide data upon which a spacecraft attitude solution may be obtained, ie it measures the pointing direction of the WFC. The star tracker will be provided by SIRA Ltd. The WFC structure and its thermal control are the responsibility of Birmingham University, and MSSL are responsible for the command and data handling system. Other tasks are shared among consortium members.

1.40 Wavebands.

As has already been mentioned, the WFC will operate mainly in the waveband 6–30nm, but others are available depending on the choice of filters and to some extent calibration in these wavebands is desirable. The following acronyms are commonly used in dividing up the wavelength band 0.2–200nm:

1) Soft X-ray for 0.2–5nm (6keV–250eV)
2) XUV for 5–30nm (250–40eV)
3) EUV (extreme ultraviolet) for 10–90nm (125–15eV)
4) VUV (Vacuum ultraviolet) for 50–200nm (25–6eV)

The above abbreviations will be used throughout this thesis, though it should be noted that the boundaries of these wavebands are only a guide and may differ somewhat from those prefered by others.

1.50 The Calibration and Evaluation of WFC Components.

If the WFC is to make worthwhile observations it is essential that its performance is thoroughly investigated. In particular, it is important that the three elements which limit WFC sensitivity, namely the filters, detectors, and mirrors, are well calibrated. The filter transmission in a variety of wavebands must be defined, as should detector quantum efficiencies, and mirror reflectivities.

This thesis will concentrate on the work required to complete the detector and mirror calibrations at Leicester.

Firstly the establishment of a suitable XUV source and monochromater is recounted and their use and performance is described. The production of a quantum efficiency standard is then reported as is its use to provide the first quantum efficiency measurements of a CsI coated MCP detector in the XUV. A comparison is made between the empirical results and a published model of photocathode behaviour. Mirror reflectivity measurements in the Soft X-ray and XUV bands are described and the results compared with predictions based on optical constants and with results published by others.

In addition to experimental work, the impact of the inclusion of a magnetic screen is assessed, by computer simulation, on low energy electron background in the WFC. Finally, the implications for WFC sensitivity of the reported measurements, together with published filter transmission data, are discussed.

CHAPTER 2

An XUV Light Source and Monochromator for the WFC Calibration and Testing Programme.

2.10 Sources of XUV

The waveband which is of greatest importance as far as the ROSAT WFC is concerned is the so called XUV band which lies between the limits of 5 and 30nm, or using equation 2.10:1, between 250eV and 40eV.

$$E(eV) = 1243.125/\lambda(\text{nm}) \qquad 2.10:1$$

Photons in this energy range are produced either as a result of electron transitions within atoms or within ions in which case the light is emitted in the form of a line with sharply defined bandwidth, or as a result of the acceleration of 'free charges' in which case the spectrum is broadband in nature. Examples of the former are the emission lines in the low energy XUV regime emitted by singly ionised atomic species in sources like the Hollow Cathode Discharge (HCS)[1]. Higher energy XUV lines are obtained from the inner electron transitions of the lighter elements as in, for example, the characteristic lines from conventional X-ray tubes[2], or from the outer electron transitions of the multiply charged ions found in Tokamaks[3], Penning discharges[4], and HCS's[5].

Continuum spectra are obtained from X-ray tubes in addition to lines and from sources such as synchrotrons, in both cases the acceleration of electrons is the emission mechanism. Black body radiation can also be a continuum XUV source, but the temperatures involved (10^5–10^6K) are prohibitively high for laboratory sources but can be attained in laser plasma experiments.

2.20 Requirements for the WFC Test Programme

XUV light is required by the WFC test programme for the following specific purposes:

1) Measurement of reflectivity of the grazing incidence mirrors, together with assessment of the surface finish (roughness) and profile.
2) Measurement of Microchannel Plate (MCP) detector quantum efficiencies.
3) Filter transmission measurements.
4) Vacuum ultraviolet (VUV) scattering measurements for a variety of WFC surfaces.

All the above measurements must be carried out at numerous wavelengths between the soft X-ray and UV wavebands so that the instrument response in the soft X-ray and XUV wavebands can be characterised and its susceptibility to UV and geocoronal XUV leakage evaluated. Mirror measurements were to be performed in the Leicester University Mirror Test Facility (MTF), which will be described in detail in chapter 6, whereas detector work was to be done in the Detector Test Facility (DTF). In addition to the MTF and DTF a monochromator/source combination was required to provide the necessary spot wavelengths for the callibration. The next few sections describe the source and the monochromator and list the criteria adopted to establish their suitability.

2.30 The Penning Discharge Source (PS)

The Penning discharge[6] has been used for many years as an ionization vacuum pressure gauge. A Penning discharge is established when a high electric potential exists between plane electrodes which have a magnetic field perpendicular to their surfaces. The magnetic field enhances the excitation of atoms by increasing the number of collisions undergone by the electrons in the discharge.

Since the 1950's, ion sources using the Penning Ionization Gauge (PIG) principle have been used by nuclear researchers to provide their accelerators with high currents of highly charged heavy ions[7]. These devices became the subject of spectroscopic study in the EUV in the 1960's[8], an interest which was extended into the XUV in the '70's[9]. The Penning source was investigated in the late 1970's[10] as a possible laboratory source for astronomical instrumentation and a great many useful lines were reported between 30nm and 5nm.

The properties observed by Finley et al. which particularly recommended the PS for the WFC programme are listed below:

1) Full coverage of the VUV and XUV wavebands from about 150nm to at least 10nm.
2) A high degree of temporal stability (albeit with an initial warm-up period during which an erratic discharge is observed).
3) Predominantly a line source which enhances the monochromaticity when used with a monochromator.
4) Although cathode sputtering occurs, monochromator contamination was observed to be low.
5) The source used was compact which meant that the discharge region could be close to the monochromator entrance slit resulting in a relatively high photometric efficiency.

2.40 The Physics of Penning Ionization Gauge Discharges.

2.41 The Cold Cathode Discharge.

There is much to be learned about the behaviour of a PIG discharge by first considering the processes occuring inside a 'simple' cold cathode discharge tube. Figure 2.41:1 shows such a tube and a simple circuit for controlling current. As the voltage between the electrodes is increased several modes of discharge become discernable, these are illustrated on the current-voltage curve of figure 2.41:2.

As the tube voltage is increased from zero no steady current is dawn, instead, low current pulses are observed which result from the creation of charge carriers within the gas by ionizing processes such as cosmic ray tracks. The frequency and magnitude of current bursts may be increased by illumination of the cathode with light, the extent of the change depending on the workfunction of the cathode material and the frequency of the light.

If the voltage is further increased the current pulses continue to intensify until a critical value of the voltage V_b is reached. At V_b, a rapid increase in current is observed for very small increases in voltage and the discharge is found to be self sustaining, i.e. it no longer requires illumination of the cathode or other ionizing phenomena to maintain it. At V_b, each electron created in the gas gains sufficient energy to generate several ions, so that enough ions strike the cathode to make the probablity of electron production by secondary emission unity. Thus for every electron which loses its energy in an ionizing collision another is liberated at the cathode to be accelerated to energies where it may ionize also. As the current increases (by increasing the applied voltage), characteristic light and dark regions appear in the tube such as the 'negative glow' and the 'Faraday dark space' due to excitation of atoms by the flow of energetic electrons.

Eventually further increase in discharge current is met by a decrease in the running voltage. This is a consequence of the build up of a positive space charge near the cathode which results from the tendancy of electrons to undergo ionizing collisions as soon as they have sufficient energy. Ionization close to the cathode means that although electrons are accelerated away quickly, ions drift more slowly due to their higher mass causing a build up. The space charge leads to most of the applied voltage being dropped across a region close to the cathode, known as the *cathode fall*, with the effect that the electric field is increased so the the ionization efficiency increases lowering the running voltage.

With the increasing current more and more photons and ions strike the cathode producing electrons by photoelectric and secondary emission, resulting in further ionization and thus more ions and photons etc. A small increase in voltage therefore dramatically increases the discharge current. The large electron

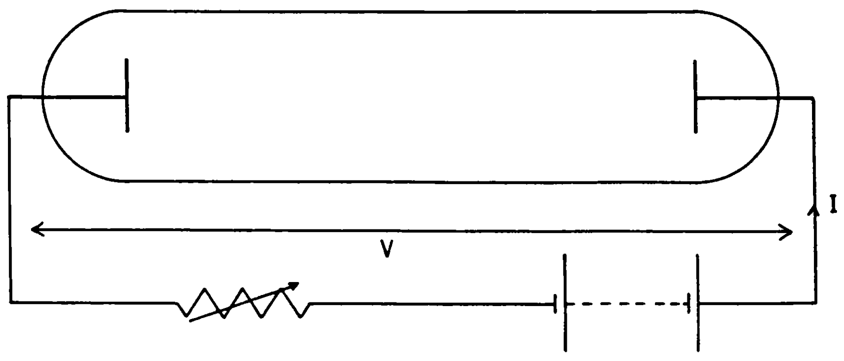

Figure 2.41:1 A simple cold cathode discharge tube with stablising resistor.

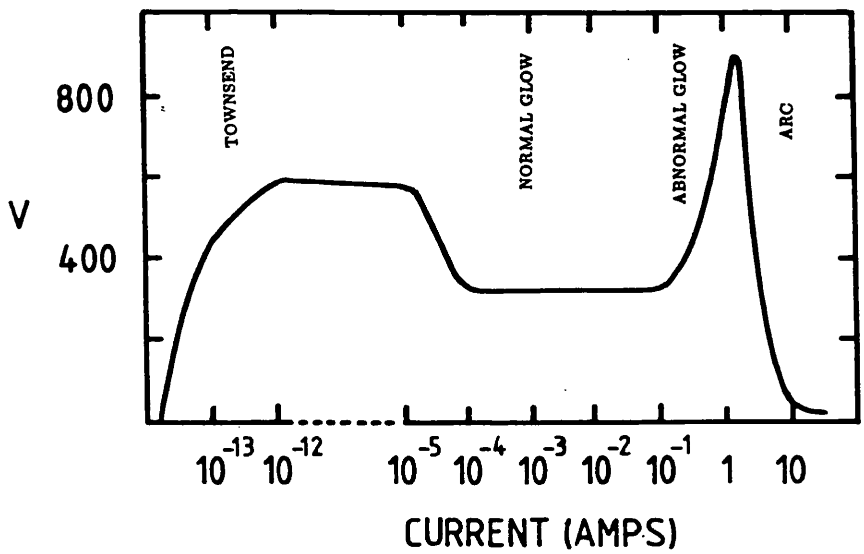

Figure 2.41:2 The current-voltage curve of a typical cold cathode discharge, showing the characteristic discharge modes. From reference 11.

current and consequent excitation of atoms and ions results in a very luminous discharge termed a 'normal glow' discharge. Figure 2.41:3, reproduced from reference[11] shows the current and charge densities, electric potential, electric field, and luminous intensity characteristic of a glow discharge.

The discharge in the normal glow covers more of the cathode surface as the current increases, until all the surface is enveloped. At this point the cathode fall increases and the voltage needed to maintain the discharge rises. The discharge is now called an 'abnormal glow' discharge.

Finally, a further fall in running voltage is observed with increasing current through enhanced electron emission from the cathode as it is heated by ion bombardment. When cathode temperature and gas temperature affect the discharge it becomes an arc discharge.

Glow discharges in some gases, notably the inert gases, may run at a lower voltage than predicted on the basis of ionization purely by electron collision. Inert gases are found to have metastable excited states of high energy which may contribute to ionization by the reaction:

$$2M^* = M + e^- + M^+$$

This process requires the collision of two metastable atoms and so the probability of ion production by this means is density dependent. At low density the probability of an encounter between two metastables is small compared with the probability of a de-exciting collision with the tube walls. Metastable ionization by this, the Penning effect[12], is therefore only of importance at high densities.

The situation is more complex if even small quantities of contaminants are present. For example, of the two reactions:

$$2Ne^* = Ne + e^- + Ne^+$$

$$2(16.6) = 21.5 + \Delta E \Rightarrow \Delta E = 11.7eV$$

and

$$Ne^* + Ar = Ar^+ + e^- + Ne$$

$$16.6 = 15.6 + \Delta E \Rightarrow \Delta E = 1.0eV$$

the second is more probable since the energy change involved is smaller. Because of this reaction only 0.1% of argon in neon can significantly reduce the running voltage of a glow discharge. This gas mixture is called a Penning mixture.

The pressures involved probably mean that metastables do not significantly contribute to the PIG discharge when running at low pressures, but they may be important during the striking of the discharge

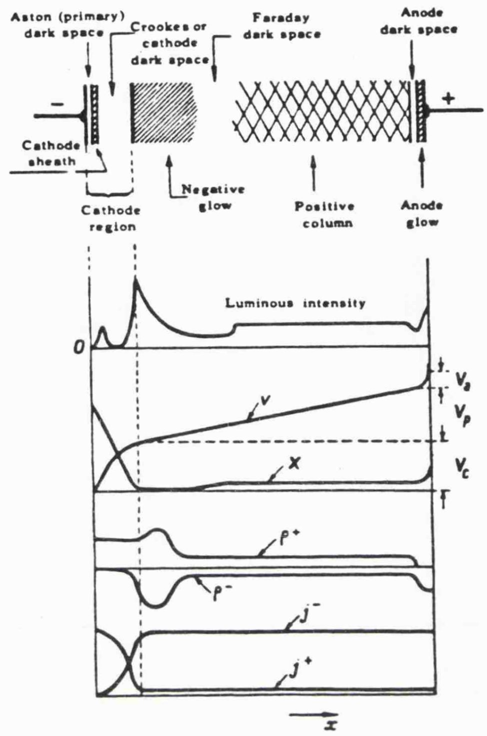

X=ELECTRIC FIELD

Figure 2.41:3 Current and charge density, electric potential, electric field, and luminous intensity in different regions of a glow discharge. From reference 11.

at higher pressure. For this reason, and their additional cost, it is unlikely that Penning mixtures will be of much value in the PIG.

2.42 Discharges in Magnetic Fields.

If a magnetic field of some 100's to 1000's of gauss is applied axially to the discharge tube of figure 2.41:1, the phenomena described above largely persist but ion and, particularly, electron paths across the field are restricted. Diffusion of charge to the tube walls is thus impeded[13] but the motion of particles along the field axis isn't as electrons are constrained to follow helical paths along the field lines. This increases the path length of the electrons in the discharge resulting in an increased ionization probability. For this reason a discharge at a given current can be sustained by a lower voltage at any particular pressure, and the onset of each discharge mode occurs at a lower pressure than in the absence of the magnetic field.

Where a cylindrical anode is employed as in figure 2.42:1, with the cylinder axis along the magnetic field, motion of electrons across the field to the anode is restricted. Under these circumstances it is thought that the necessary movement of charge to the anode to maintain the discharge is brought about by density variations in the plasma due to instability[13].

The situation with the PIG discharge is of two such tubes placed back to back, figure 2.42:2. The result is that the positive column, or plasma, fills the hollow anode and the cathode fall occurs in a 'sheath' close to each cathode. Electrons accelerated by the cathode fall propogate in a beam through the anode following helical paths and undergoing collisions, some of which result in ionization or excitation of residual gas atoms with an accompanying loss of energy. Having lost energy, electrons passing through the anode towards the opposite cathode lack sufficient energy to pass through the cathode fall to the cathode and so are reflected to pass through the anode again.

Electrons may thus oscillate back and forth between the cathodes, perhaps many times, and it is for this reason that it is thought that the build up of high charge state ions in the plasma is by a step-wise ionization process. The cross sections for production of multiply charged ions by single collision are too small to account for the observed ion populations, and in any case this mechanism would require a higher electron temperature in the plasma than has been observed[14].

Ion production by PIGs has been used in accelerator physics as a source of multiply charged heavy ions[7]. Ion currents from such sources are extracted either through a hole in one cathode or through a slit in the anode cylinder using a pulling electrode biased at 10–50 kV with respect to the ion source[15, 16].

A consequence of multiply charged ion production, and the high voltage operation of PIGs at low pressure, is the sputtering of material from the cathode surfaces by the energetic ion beam.

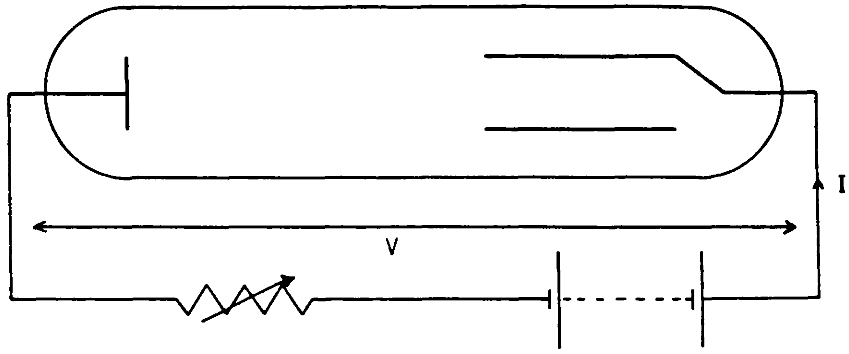

Figure 2.42:1 Discharge tube with a cylindrical anode co-axial with a magnetic field.

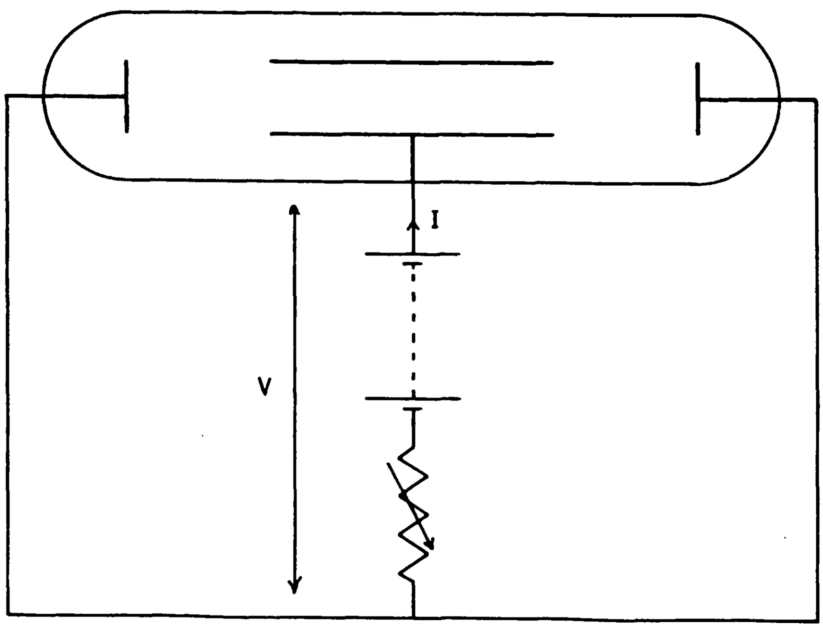

Figure 2.42:2 PIG geometry with two cathodes either side of a cylindrical anode and with a magnetic field orientated along the cylinder axis.

This may be of benefit or a hindrance depending on the application, since although loss of material from the cathodes severly reduces their life it also allows a build up in the plasma of ion species of the cathode material. Often, gaseous forms of cathode materials are not available, eg. aluminium, in which case generation of ions or emission lines may require the sputtering of materials into the plasma[4]. For the application described in this thesis, aluminium was used as the cathode material as aluminium ions exhibit a useful emission line spectrum in the 10–20nm waveband[10], the sputtering characteristic of PIGs was therefore of prime importance.

2.50 The Test Programme PS.

The PS procured for the WFC test programme was obtained from the Rutherford Appleton Laboratory (RAL) in Oxfordshire and is based on a source first produced for the Culham Laboratory. A detailed diagram of the PS is shown in figure 2.50:1 and the principal features of note are the replaceable cathodes and anode pieces, the four sintered Samariun-Cobalt permanent magnets (two behind each cathode), which provide the magnetic field normal to the electrodes, and the gas feed line for the supply of the discharge gas. The source is constructed mainly of two materials, the magnets are bonded to mild steel back plates which carry the brass cathode assemblies and a brass anode holder is sandwiched between them, steel bolts through both base plates serving both to hold the source together and to complete the magnetic circuit. The anode holder is insulated from the cathodes by two polytetrafluoroethene (PTFE) spacers and holds the pumping and monochromator ports. Both cathode and anode assemblies are provided with channels through which cooling water may flow.

Electrical power is supplied to the lamp from a 3kV 1Amp. stablised power supply by means of heavy duty co-axial cables. A series resistance of 300 Ohms is included in the power supply as a further means of stabilisation when high voltage break down occurs inside the PS. The negative H.T. lead is connected to one of the cathodes (both being connected together by six bolts) and the positive lead is connected to the anode which is earthed.

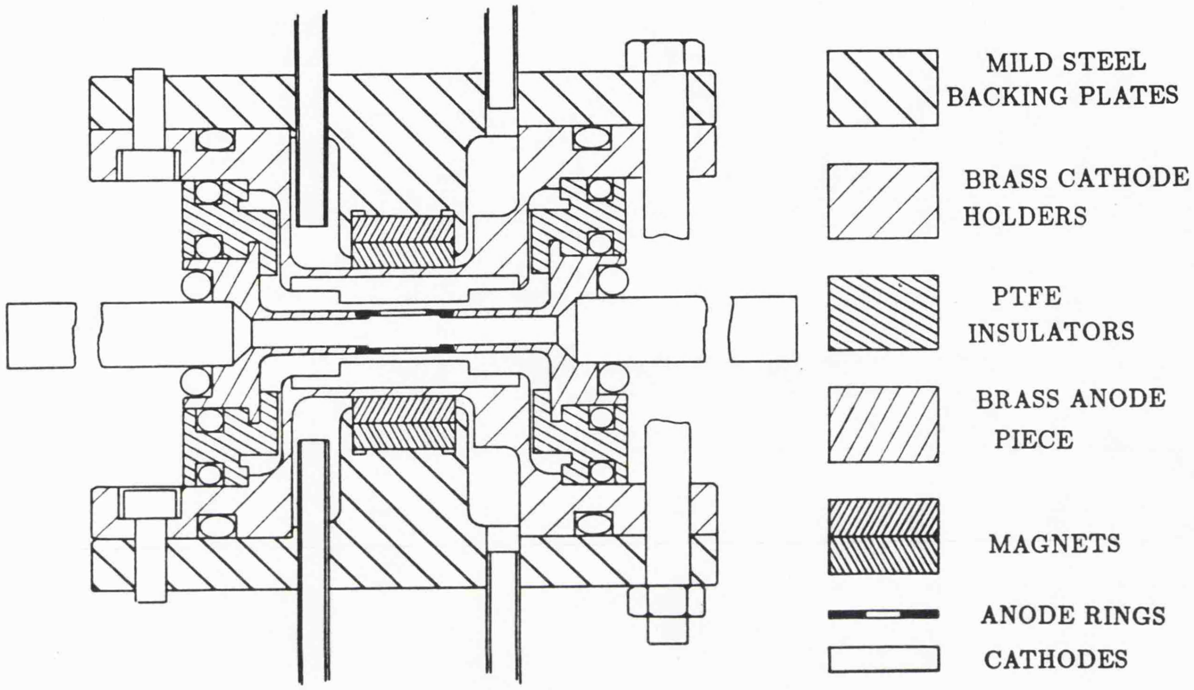

Figure 2.50:1 A section through the Penning source showing its principal components.

2.60 The XUV Monochromator.

It has already been mentioned that a monochromator was required with which to perform many of the calibration tests necessary on various WFC components, notably the mirrors and the CsI coated MCP detectors. The requirement for a stationary exit beam so that it would mate with the existing mirror and detector test facilities, and the need for a low cost device meant that the monochromator had to be designed in house by Dr. R. Willingale and D. Watson and by the manufacturers, Astron Developments Ltd. The result was a compact instrument which was based around a concave grating of radius of curvature 1m on a Rowland circle of radius 0.5m. The exit slit was fixed with respect to the grating whilst the entrance slit was constrained to move, via a lead screw and radius arm mechanism, around the Rowland circle ie. the opposite arrangment to that normally employed. The lead screw was driven directly by a stepper motor an arrangement which was not without drawbacks as will be made apparent in Section 3.32. When the stepper motor was driven the source table moved around the Rowland circle, scanning a non-linear wavelength scale with time.

A grating blazed at 30nm was chosen with 300 lines per mm, the amount of movement in the source slit position then allowed complete coverage in wavelength from 200nm through zeroth order to about -5nm. A minus wavelengh indicates a slit position closer to the grating than at zeroth order, i.e. an outside order spectrum rather than an inside order. In fact, the short wavelength limit of the instrument was defined by the fall in grating reflectivity with wavelength.

Resolution was not of prime importance as the light source to be used was a line source, a resolution of about 0.1nm was thought acceptable compared with a theoretical grating resolution of 0.002nm at 30nm.

Figure 2.60:1 shows the main external features of the monochromator. The grating mount and exit slit assembly are situated within the main vacuum body to which the entrance slit flange is connected via an edge welded high vacuum bellows. Provision was made for up to four sets of exit slits to be installed and any of these can be selected using the linear motion feedthrough. The entrance slit, or source, flange is shown in figure 2.60:2 and it contains only one slit which is adjustable by removing the slit plate and re-setting the slit gap with feeler gauges. The slit position with respect to the Rowland circle can be adjusted by moving the whole flange on its fixing bracket.

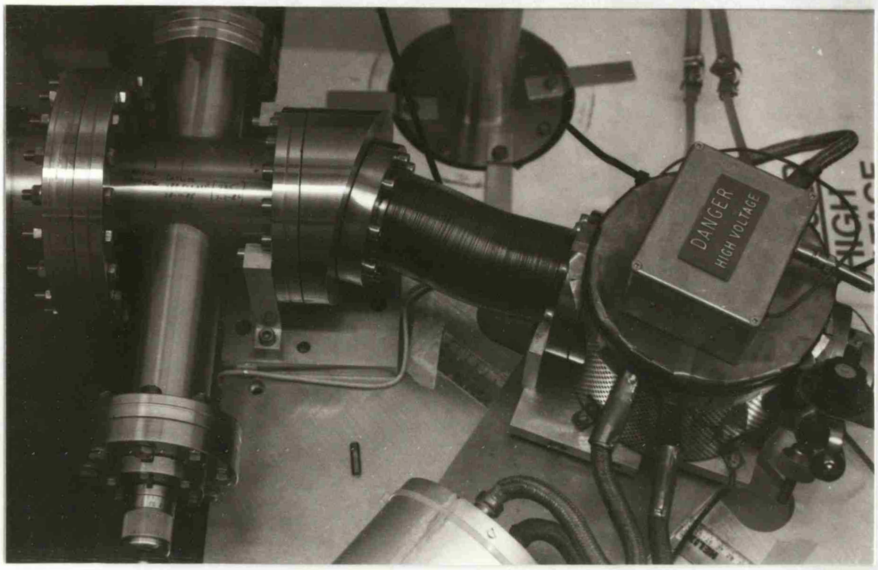

Figure 2.60:1 A photograph of the monochromator showing its main external features including: the vacuum body with slit selection feedthrough, bellows, source flange, and base plate.

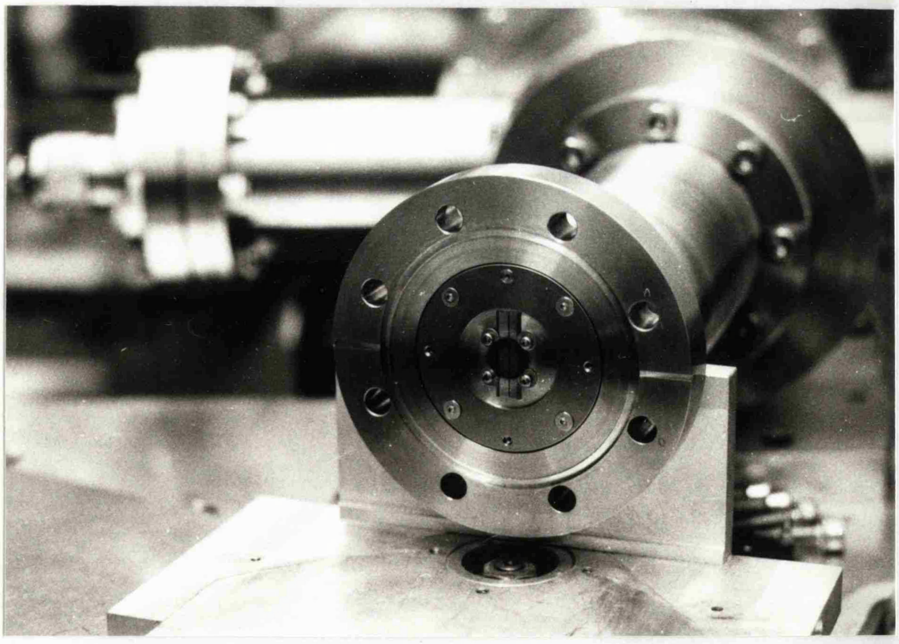

Figure 2.60:2 A photograph of the monochromator source flange showing the single entrance slit and mounting plate.

2.61 Optical Alignment of the Monochromator.

The lay-out of the monomchromator's optical components with respect to the Rowland circle is illustrated by figure 2.61:1 in which the angles a and b satisfy the equation[17]:

$$m\lambda = d(sin(a) - sin(b)) \qquad 2.61:1$$

where m is the spectral order and d is the grating constant. A treatment of the grating equation is to be found in any optics text (Eg. referance 18); for a complete discussion of the concave grating see Namioka 1959[19].

In the plane of the Rowland circle a good focused image of the source slit is observed on the Rowland circle when both the grating centre and the source slit are on the Rowland circle, as in figure 2.61:1. In addition the grating normal must point along the radius of the Rowland circle to its centre, and to obtain the brightest image the plane of the source slit must be perpendicular to the line SG joining slit and grating centre. The only other requirement is that the slits be parallel with the grating 'rulings'.

These general principles were translated into the following specific criteria for assessing the alignment of the monochromator:

1) With the source slit in zeroth order position with respect to the grating, a bright image should be seen of the exit slit at the source slit position (it is easier to arrange a light source to illuminate the stationary exit slit than the moveable entrance slit).
2) A bright focussed image of the exit slit should be formed at the appropriate first order source position when the exit slit is illuminated with monocromatic light.
3) All focussed images must be vertical in the source flange plane.

A means of testing for alignment was devised in which a He-Ne laser (wavelength 632.8nm) illuminated the exit slit and the source slit was replaced by a ground glass screen. For a source position corresponding to 632.8 nm (ie b=53.17 deg. in fig.2.61:1) the bellows and slit flange had to be removed as the source table would not traverse that far. Instead of the source flange the glass screen was supported by a right-angled block which could be moved between two marked positions: zeroth order, and first order corresponding to 632.17nm. Using this simple apparatus it was found that focused images could be obtained on the Rowland circle to within the estimated measuring accuracy of ±0.5mm in 0.5m.

The alignment procedure was an iteration of setting up in zeroth order position and adjusting the grating position or orientation until a bright focused image was observed, and then switching to first order position (b=53.17deg.) and similarly readjusting. Many iterations were required before a

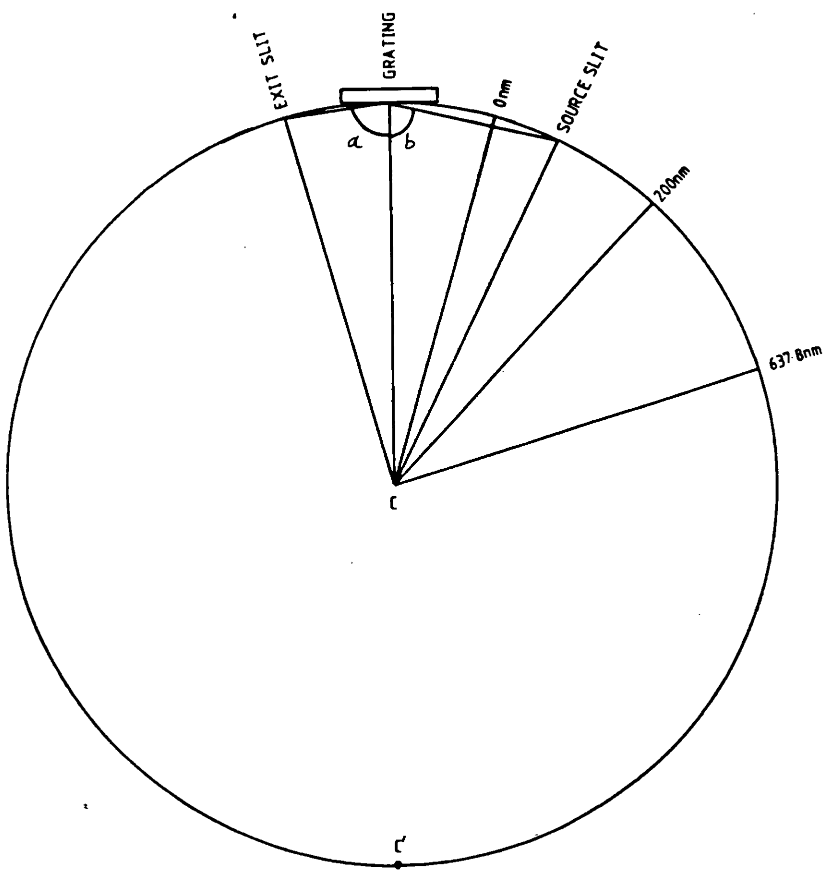

Figure 2.61:1 Schematic of the monochromator optical elements around the Rowland circle and indicating the position of the He-Ne spot during alignment.

satisfactory result was obtained and the whole procedure was very time consuming, largely because of the way in which grating adjustment was effected.

A diagram of the grating and exit slit assembly is shown in figure 2.61:2 illustrating the method of grating adjustment. The relative distance between exit slit and grating is fixed as is the orientation, but the whole assembly can be moved with respect to the entrance slit. The six screws and lock nuts equispaced around the two fixing rings allow adjustment in position in two axes and orientation in two axes. The third positional axis is catered for by moving the whole mount towards or away from the source slit and the third orientational axis is the longitudinal axis about which the assembly may be rotated.

When an acceptable alignment had been achieved all six lock nuts were tightened and the alignment rechecked. Finally the bellows and source flange were replaced and the monochromator vacuum system was connected.

The only sure indication of satisfactory alignment is the recording of spectra in the normal range of operation, ie 10–150nm. The relative positions of the known lines and their positions with respect to the zeroth order peak would betray any gross error in alignment. Therefore as a final check a series of measurements was planned using helium which is well known to exhibit two strong resonance series between 58.4nm and 24.3nm. Chapter 3 will concentrate on this work, on the additional equipment required before it could be undertaken, and on the assessment of the monochromator and source as a combination.

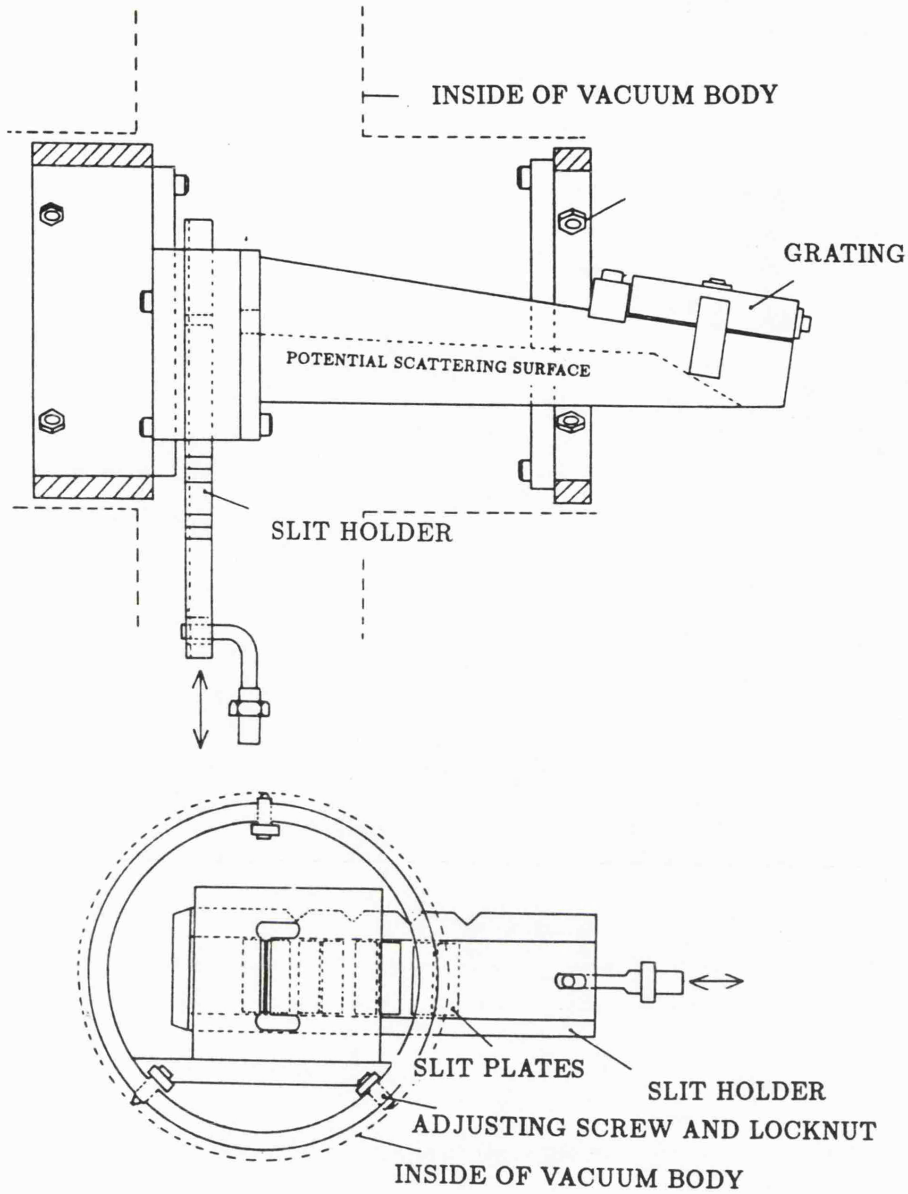

Figure 2.61:2 Diagram of the grating and exit slit assembly showing the six adjusment screws used during alignment.

CHAPTER 3

The Monochromator and Penning Source Combination.

3.10 Introduction.

Before the monochromator and PS could be used together as intended a series of experimental investigations was necessary. Firstly, a vacuum test of the PS was required to confirm that it was vacuum tight, that it would be possible to control gas flow easily, and that the high voltage supply worked. Secondly, it was important to verify the optical alignment of the monochromator using XUV light from the PS—which necessitated the construction of a dual vacuum system and the choice of an XUV detector.

3.11 Preliminary PS Tests.

Figure 3.11:1 shows the apparatus used for preliminary investigations of source performance, ie the assessment of electrical and vacuum behaviour. The diagram shows an 80ls^{-1} diffusion pump, a needle valve controlled gas feed line, and the source cage and insulation necessary because of the otherwise exposed HT cathodes. Also shown is the single wire proportional counter attached to the monochromator port of the PS which was used to confirm that the source did actually produce high energy photons. Since the window thickness (about 1 μm polypropylene) was such that the counter efficiency was very low at these wavelengths no quantitative measurements were attempted, but a definite correlation was observed between count rate and, for example, discharge current.

The PS was found to be adequately vacuum tight, pressures down to 5×10^{-6}mbar being recorded using the apparatus of figure 3.11:1 with the proportional counter window blanked off. With the needle valve on the gas feed line it was found to be a relatively simple matter to control source pressure over the range 10^{-5} to 10^{-2}mbar with a gas line pressure of a few pounds per square inch, as indicated on the gas bottle regulater. The electrical characteristics of course varied markedly with source pressure, but there was found to be a qualitative agreement between current–voltage characteristics recorded at different pressures so that shown in figure 3.11:2 may be taken as representative. The system pressure of 4×10^{-3}mbar is the pressure as indicated by the Penning gauge shown in figure 3.11:1 and is not strictly speaking the pressure in the source as this has a somewhat restricted pumping aperture and itself acts as a vacuum pump[1].

The rapid growth of discharge current with applied voltage, in figure 3.11:2, is a consequence of

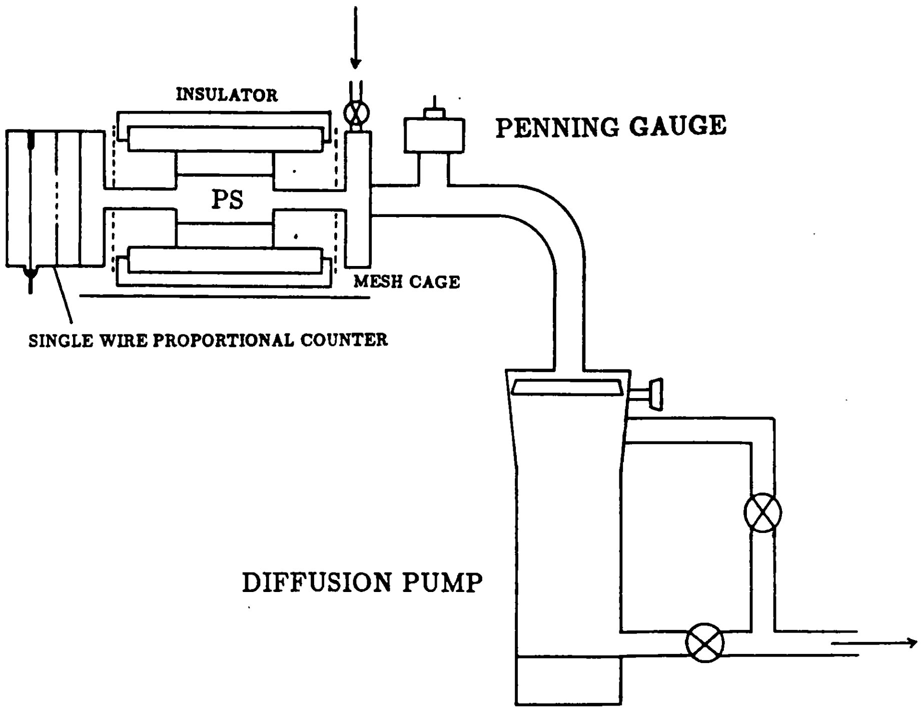

Figure 3.11:1 Diagram of the source cage and vacuum system used for initial tests.

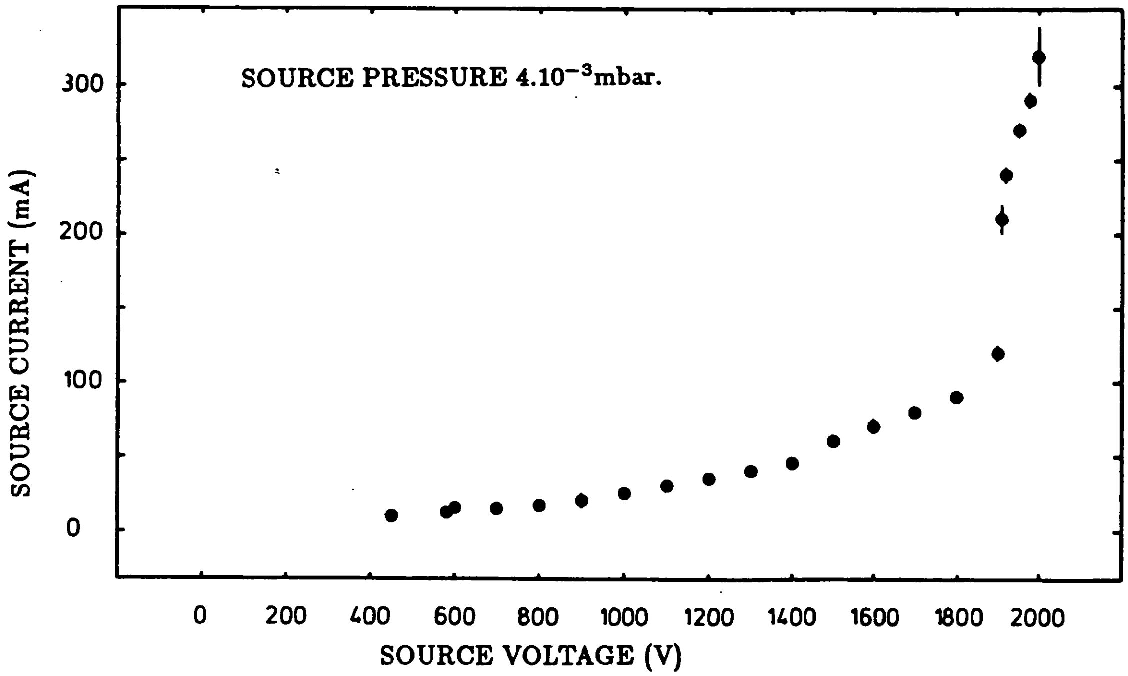

Figure 3.11:2 Typical electrical characteristic of the Penning source operated with argon.

the increasing numbers of charge carriers (electrons and positive ions) present due to ionisation of the residual gas by electron collision and the influence of excited states in gas atoms, and by the liberation of electrons from the cathode by photoelectric emission (chapter 2).

3.12 The Choice of an XUV Detector.

XUV detectors rely on the conversion of XUV photons into something more easily detectable, for example visible light or electrons. The secondary detector may be something like an electron multiplier to detect electrons, or a human eye or photographic emulsion to detect light, or a photomultiplier tube (which is a union of photocathode and electron multiplier).

To detect XUV photons emanating from the monochromator, the detector must be compatible with the vacuum environment between 10^{-4} and 10^{-6}mbar and must in no way contribute contaminants to the grating which is highly sensitive to monolayers, particularly of hydrocarbons[2]. Vacuum compatibilty is dictated by the lack of a window material which transmits shortwards of 104nm.

To fulfil these requirements the simplest solution was to install a Channel Electron Multiplier (CEM). The CEM has the virtues of being compact and robust and posessed of a large dynamic range; in addition it can be operated in photon counting mode using standard single wire proportional counter electronics. This latter point is an advantage because such electronics is plentiful in a group with a background in X-ray instrumentation. CEM quantum efficiencies have been measured[3] and a typical plot of Q.E. vs. wavelength is reproduced in figure 3.12:1 showing that useful sensitivity can be expected well into the soft X-ray region.

The type of CEM chosen was the Mullard B318 which has an input cone diameter of about 5mm, the choice was made for reasons of cost as much as anything as it was not intended to serve as a more than a simple monitor counter. A circular input aperture of some 5mm in extent was however an attractive feature as it relaxed the tolerance with which the CEM needed to be aligned with the monochromator beam. Figure 3.12:2 shows a photograph of the CEM in its PTFE mount suported by the three conductors of a high vacuum/high voltage feedthrough. This detector assembly was fitted to the monochromator by means of a 200mm to 70 mm OD (Outside Diameter) vacuum flange adapter.

The CEM electronics, as has already been mentioned, was single wire proportional counter electronics modified only in that the HT decoupling capacitors were uprated to 3kV. Figure 3.12:3 shows schematically the electronic configuration, which was realised using Harwell HT supply, pre-amplifier, and shaping amplifier. Pulse counting was by a Multichannel Analyser (MCA) which operated in either Pulse Height Distribution (PHD) mode or Multichannel Scaler (MCS) mode; the former displaying information about the state of operation of the CEM while the latter a record of count rate against time.

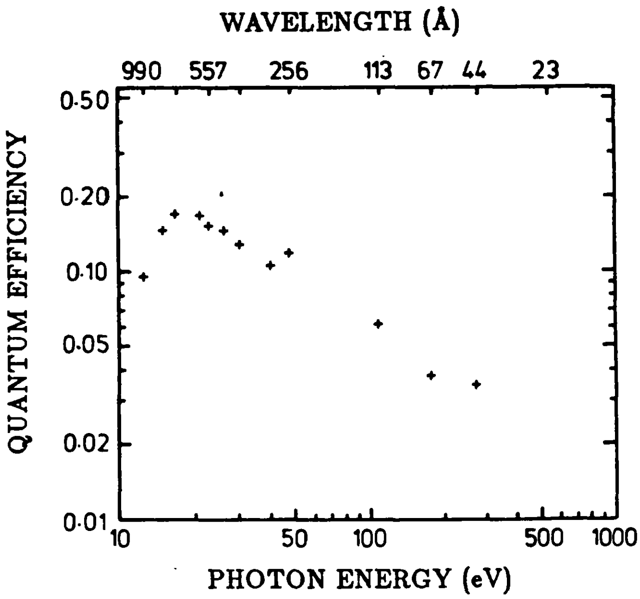

Figure 3.12:1 Graph showing the quantum efficiencies typical of CEMs. From reference 15.

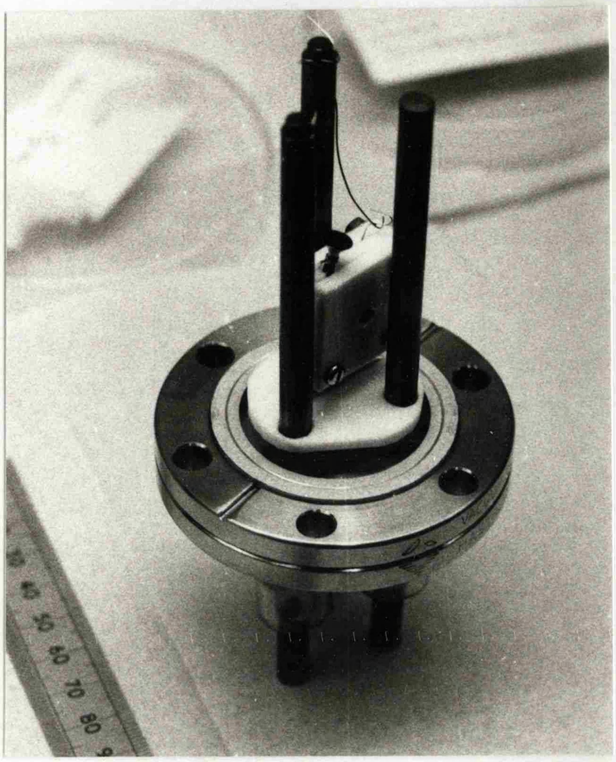

Figure 3.12:2 A photograph of the Mullard CEM in its PTFE mount.

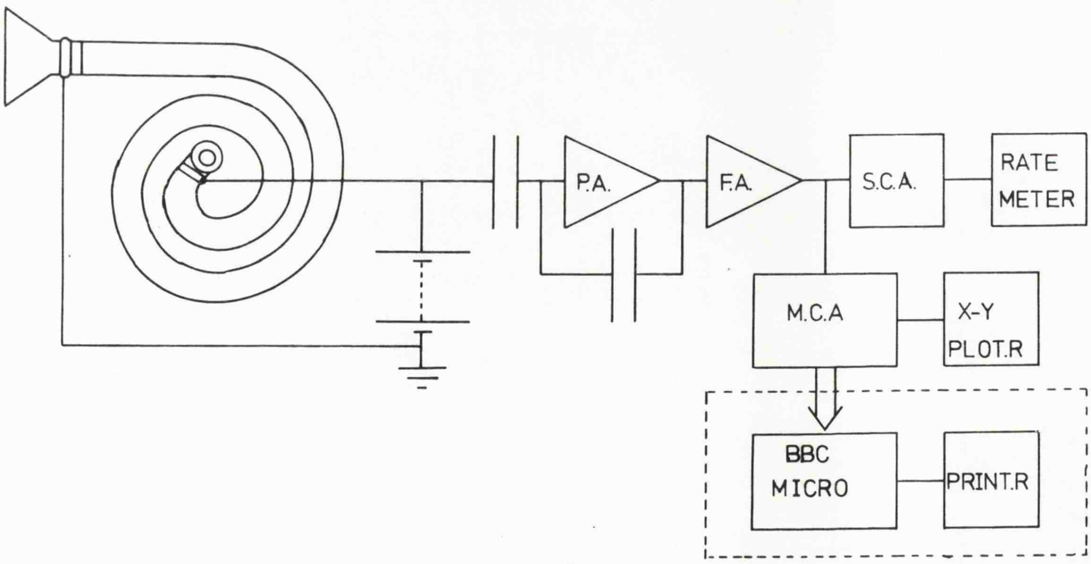

Figure 3.12:3 Schematic of the CEM pulse counting electronics.

A plot of count rate vs. time is useful as it can be interpreted directly as a spectrum.

3.13 Vacuum and Cooling Equipment for the Monochromator and PS.

The monochromator and PS were intended from their inception to be used together as one instrument producing XUV. This section will concentrate on the few modifications required before they could combined as such.

After the monochromator had been optically aligned as far as could be judged, the only remaining assembly job was the reinstatement of the vacuum bellows and the flange holding the source slit. Figure 3.13:1 shows the arrangement of pivots associated with the lead screw mechanism for moving the source table. It is these pivots which define the scanning behaviour of the instrument, for example, if the grating centre is precisely over pivot A and the source slit is precisely above pivot B, then because the lead screw runs between A and B both grating and slit are on the Rowland circle. The procedure for optically aligning the monochromater outlined in section 2.61 used a screen at pivot B, instead of the slit, at two points around the Rowland circle thus ensuring that the grating was on the circle. The only requirement for continued alignment was then that the source slit be positioned accurately at pivot B. This was done by eye when bellows and source flange were replaced, and it was left until XUV tests were complete before deciding whether its position was satisfactory.

The PS together with its insulated base and earthed cage fitted onto the source table with only minor remodelling. It was held in place by the eight bolts securing the PS 'monochromator port' to the monochromators source flange.

During the tests of the PS above, cooling had been effected by blowing compressed air through the water channels provided in the PS body. In most of the laboratories in which the source was likely to be used subsequently, however, no air lines existed so the source had to be water cooled.

Water cooling the PS presented a problem in that the regions most in need of cooling, the cathodes containing the sintered magnets, were at a high negative potential (up to 3kV). This meant that if mains water was to be used a long column of it would be needed between any high voltage and ground. The system adopted is illustrated in figure 3.13:2 and it consists of a long PVC tube, inside an earthed aluminium case, running between two metal pipes one of which was the PS cathode inlet pipe and the other of which was grounded.

While the monochromator was being aligned its vacuum system was being assembled in the Physics Departments' workshops. The completed assembly is shown schematically in figure 3.13:3. It is divided into two similar halves: the monochromator pumping system, and the PS pumping system. Both were diffusion pump based with the monochromator pump having a capacity of $280 ls^{-1}$ compared with $80 ls^{-1}$

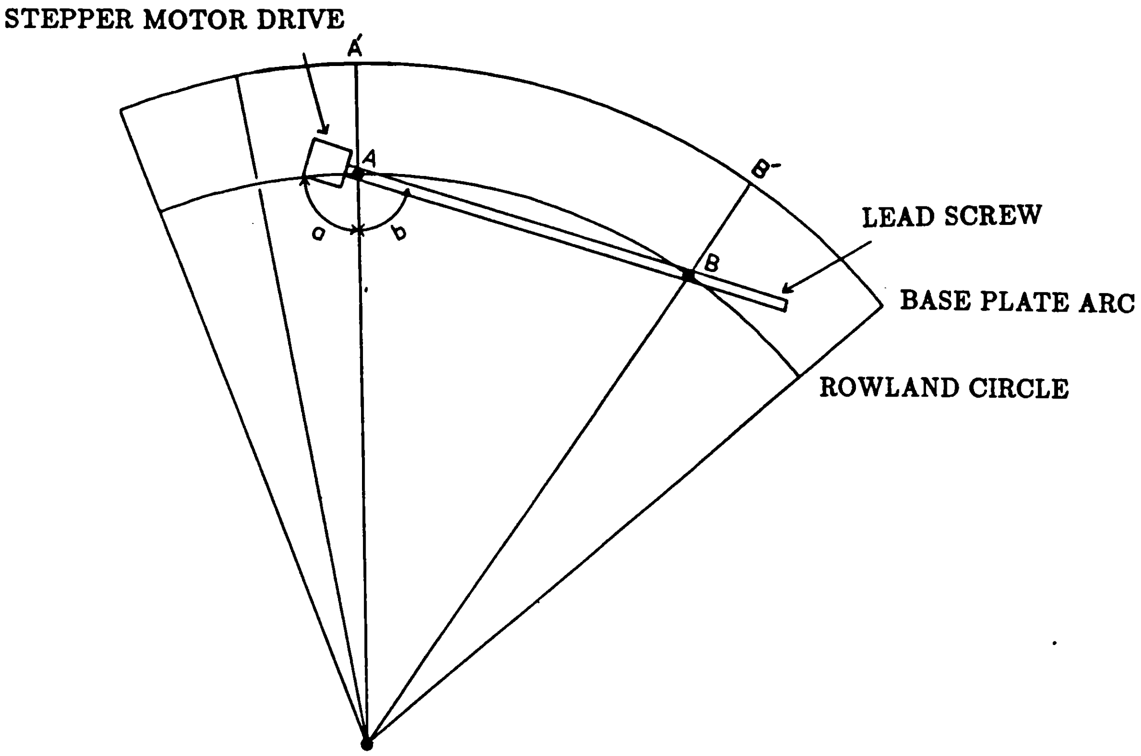

Figure 3.13:1 Schematic of the monochromator lead screw pivots which define the scanning motion of the source table.

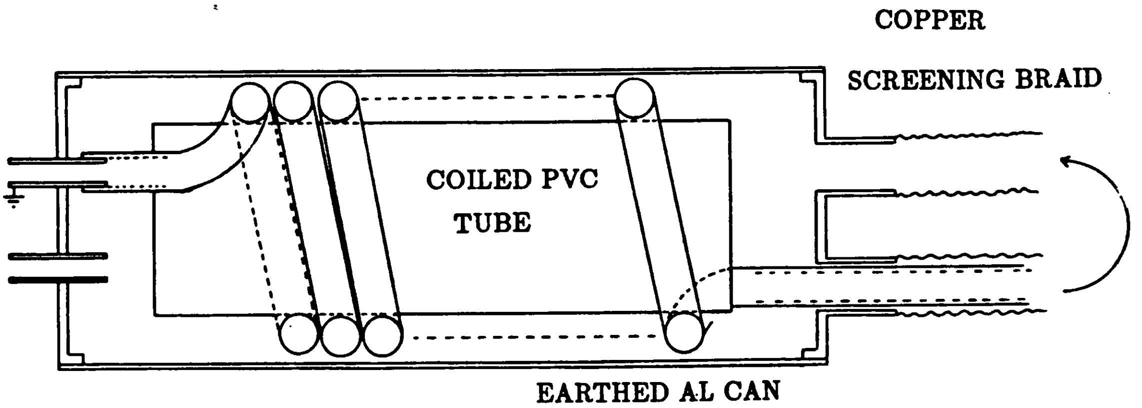

Figure 3.13:2 The PS water cooling system. The coiled pipe ensures a long path to ground through the water, limiting the leakage current.

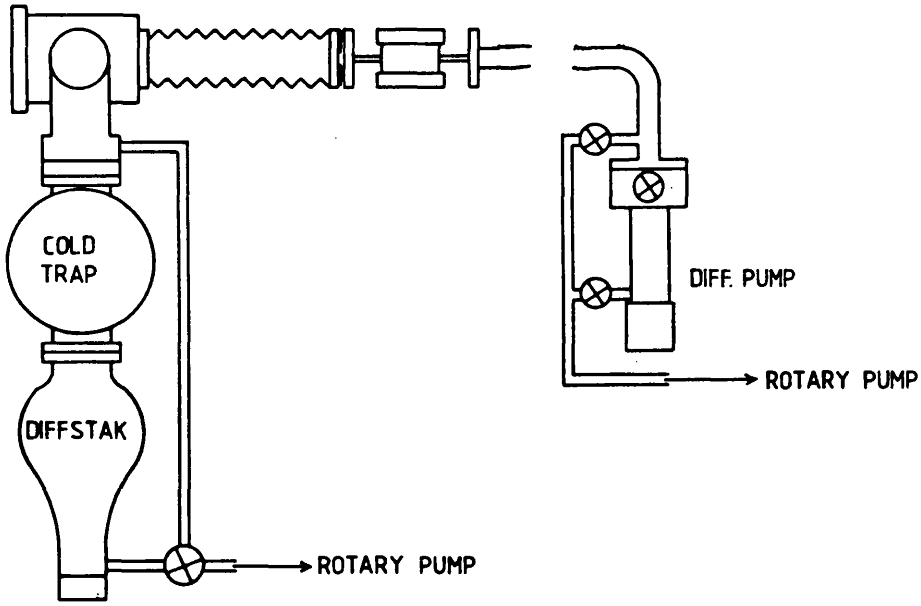

Figure 3.13:3 Schematic of the monochromator and PS pumping systems.

for the PS. The monochromator diffusion pump was topped by a liquid nitrogen cold trap which served to prevent diffusion pump oil products migrating onto the grating as well as to increase the pumping speed for water vapour. No such trap was fitted to the PS pump as it was expected that the high volume of gas pumped would prevent backstreaming, and in any case the conductance between the two systems was expected to be small as their only communication was via the monochromator source slit plate.

Initially both vacuum systems were backed using the same rotary pump, but it was later found that when operating the source with helium the large throughput of this gas made controlling the pressure difficult. The problem was that helium, being a small molecule, was not pumped as effectively as other gases resulting in a higher than acceptable foreline pressure. High foreline pressure was not a problem in the PS diffusion pump as a constant watch was being kept on its performance, but in the monochromator where the pressure might be required to remain below a certain maximum (for example because of detector operation) a more constant pressure was desirable. A separate rotary pump was therefore installed for the PS foreline.

This pumping configuration was satisfactory for initial tests and for detector calibrations described in chapters 4 and 5, but it was subsequently modified for the mirror tests which will be described in chapter 6. These modifications were mainly the adoption of a turbomolecular pump in place of the diffusion pump on the monochromator, so as to eliminate the threat to the mirrors posed by oil contamination, and the abandonment of a separate pumping system for the PS. A more detailed description of the later modifications will be presented in section 3.60.

3.20 Monochromator Wavelength Scale and Calibration.

It has been observed already that the ultimate test of monochromator alignment is its XUV performance, and with the commissioning of the vacuum system these tests could proceed. The purpose of the exercise was to establish the degree to which the monochromators parameters, the angles a and b, followed the ideal of the grating equation (2.61:1):

$$m\lambda = d(\sin(a) - \sin(b)).$$

Where m is the spectral order, d is the grating constant, a is the angle subtended between the grating normal and the exit slit, and b is the angle similarly subtended by the source slit. As far as m is concerned orders 0 and 1 are of primary interest, d is fixed by the grating manufacturer to 3.33×10^{-6}m, and a is fixed at about 82 degrees because the exit slit is located rigidly with respect to the grating. The wavelength calibration must therefore precisely determine a value for a which satisfies the above equation, if no such value can be found which is consistent then the monochromator is misaligned.

Given a value for the angle a wavelengths are determined by the angle b, but this is not a parameter which is readily discernible from the source table postion on the monochromator—much of which is enclosed by the vacuum body. Instead it was decided to use the distance measured around the arc of the monochromator base plate from some fixed marker to the line joining the radius arm pivot with the source table pivot (ie, pivots B and C of figure 3.13:1), and from this infer the value of b. Refering to figure 3.13:1 again, the length of the arc $A'B'$ is $R'(\pi - b)$ with b expressed in radians. Using this and the grating equation we get an expression for the wavelength in terms of the length $A'B'$:

$$m\lambda = d(\sin(a) - \sin 1/2(\pi/2 - A'B'/R')).$$

R', the radius of the base plate arc (which is approximately concentric with the Rowland circle) was measured to be 0.595m.

When the opportunity arose to do an XUV calibration of the monochromator the cooling system for the PS had still to be completed. This presented problems as the compressed air cooling previously employed was no longer available, so in effect the source could not be used. In the absence of any other source it was decided to attach a Penning gauge to the pumping port of the PS so that its axis pointed through the source towards the monochromator entrance slit. By bleeding in helium through the needle valve it was hoped that a detectable flux would be produced by the Penning gauge, which might at least enable an assessment of detector performance.

In fact the Penning gauge proved to be a most impressive XUV source as the first spectrum recorded (figure 3.20:1) shows. This is a raw spectum ie, it displays count rate vertically against MCA channel number, no attempt having been made to produce a linear wavelength scale. Several strong emission lines are recognizable and the strongest of these occurs in approximately the position expected of the 30.4nm line of ionised helium. Helium has another intense line at 58.4nm characteristic of atomic helium and any spectrum containing the 30.4nm line was expected to exhibit this line also, and indeed it was identified with that on the extreme right of the figure.

It was not obvious that the right hand line of those observed was the 58.4nm line, this fact emerged from the following analysis. To the left of the line easily identified as 30.4nm there was a weaker line occupying the position in which the second line of the HeII series at 25.6nm would be expected. Using these positions and the position of zeroth order, easily measured by scanning the source table through to its short wavelength limit and noting the position of the zero order peak, two values of the angle a were calculated. Using these the expected position of the 58.4nm line was determined from equation

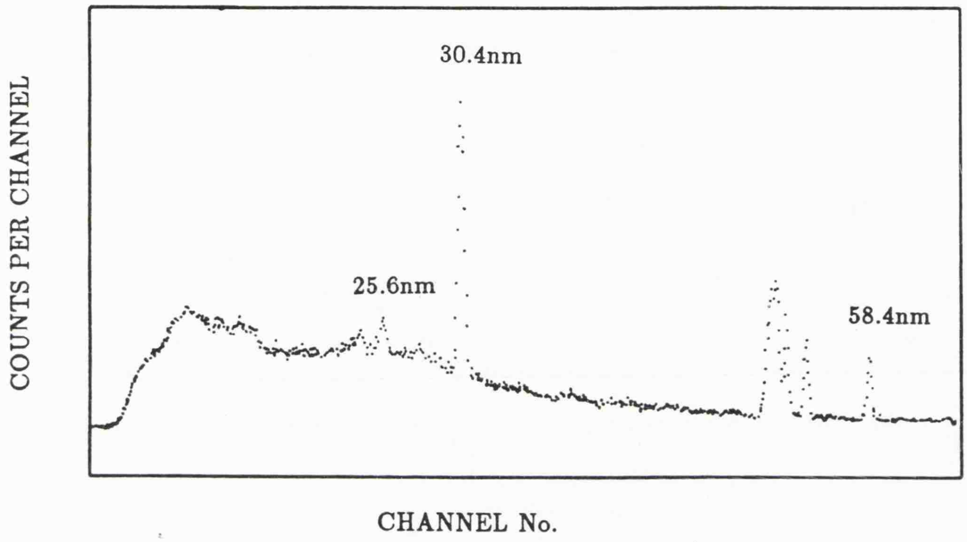

Figure 3.20:1 Spectrum of helium generated by a Penning gauge.

2.61:1. This having been done, a third value of a was calculated and found to be consistant with those previously obtained. An average was taken of the three numbers and this value was subsequently used with some success in determining the wavelengths of other lines from the positions at which they occured around the base plate. a was found to be 81.77 degrees.

It came as no particular surprise that a Penning gauge should be a source of XUV, after all the PS is based on the same design and is in truth a large, high current vacuum gauge. What was unexpected was the high flux observed, the gauge being constructed with what appears to be an optical baffle at its open end. Furthermore, the gauge was viewed by the monochromator through the axis of the PS, a tube with a diameter of approximately 5mm and length about 150mm. This also lead to the expectation of a low count rate.

3.30 Low Current Discharges.

When at last the PS water cooling was in operation the Penning gauge was removed to its rightful place on the PS vacuum system. It became immediately apparent when the source was first used that it was not going to be quite as easy to establish high current discharges as it had been when the source was operating on its own. The source pressure was found to be easily controllable when the source pressure was below about 10^{-2}mbar (using helium) but as soon as it was tried to increase the pressure further it became unstable. In its new environment connected to the monochromator, the source was evidently under lower pressure than had been the case before for a given Penning gauge reading. This was in spite of the fact that the gauge was in a similar position to that which it had previously occupied, and was probably due to the proximity of the monochromator source slit which had a significant pumping aperture. Also, the source had previously been used with argon and not with helium.

Not being able to elevate the source pressure was a serious drawback with the equipment as it was initially configured, and it was not immediately apparent whether an effective solution would be forthcoming. In the meantime, while this problem was being investigated off-line, it was decided to continue with the apparatus as it stood and investigate some low current discharges. Even when high pressures where obtained (with some difficulty) it was found that no stable discharges could be maintained probably as a consequence of the current limiting circuit of the PS power supply.

The high voltage power supply purchased for the PS used a current limiting circuit which it was originally hoped would enable stable discharges to be attained easily. It was thought that by setting the current limit control to a certain current, the power supply would maintain the current at that value if the voltage control was set high enough, by adjusting the voltage accordingly. What in fact occured was that the supply did indeed try to maintain its current by reducing or increasing the voltage, but it was unable to do so quickly enough. Consequently if the current in the discharge began to rise the supply would cut the voltage—but by too much so that the discharge would decay, this would then force the voltage up until the source again struck.

The striking voltage of a discharge is always larger than that required simply to maintain the discharge[1], as a result, the supply would cause very large oscillations in current and voltage. The only way out of this cycle was to introduce some stabilising influence into the circuit in the form of a large series resistor.

A series resistance is a commonly used form of discharge stabilizer[4], it works by limiting the current which may be drawn by the discharge when it strikes and its resistance drops suddenly. Constructing such a resistor became a high priority.

Initial PS discharges were establised in argon but at low current (of the order of 5mA). Attempts were made to record spectra of these discharges but it was found that although there was a significant count rate, there were no detectable lines present. This at first led to speculation that the grating may have been contaminated as all that could be seen was a gradually increasing continuum towards shorter wavelengths. Switching to helium dispelled this fear when a discharge at 1kV and 10^{-3}mbar revealed a spectrum similar to that observed with the Penning gauge, except that it exhibited a rather stronger continuum towards short wavelenghths much as the argon discharge had.

In addition to the continuum towards shorter wavelengths the overall level of continuum was found to be somewhat greater for the PS than had been observed with the Penning gauge.

In an attempt to establish whether or not this high background was due to unfavourable source conditions, a series of discharges was initiated at several voltages with a constant pressure of 4×10^{-3}mbar. The monochromator was then traversed through the 30.4nm line while the detector count rate was monitored on the MCS. The resulting series of line profiles is show in figure 3.30:1 and it can be seen that the line goes from being a strong emission feature at 450V to an absorption feature at 2.5kV. A data set recorded at 10^{-3}mbar (figure 3.30:2) exhibits similar behaviour but the level of background is much greater and the lines are only poorly excited at low voltages. This indicates that the ideal conditions for observing the HeI series are of relatively high pressure but low voltage, although the physical explanation for this is not clear. It could perhaps be that the high voltage and low pressures lead to the existence in the discharge of energetic electrons which do indeed produce a XUV continuum stronger than the line emission of the HeII ion. This would be seen in absorption if there were sufficient helium ions in the line of sight to the monochromator.

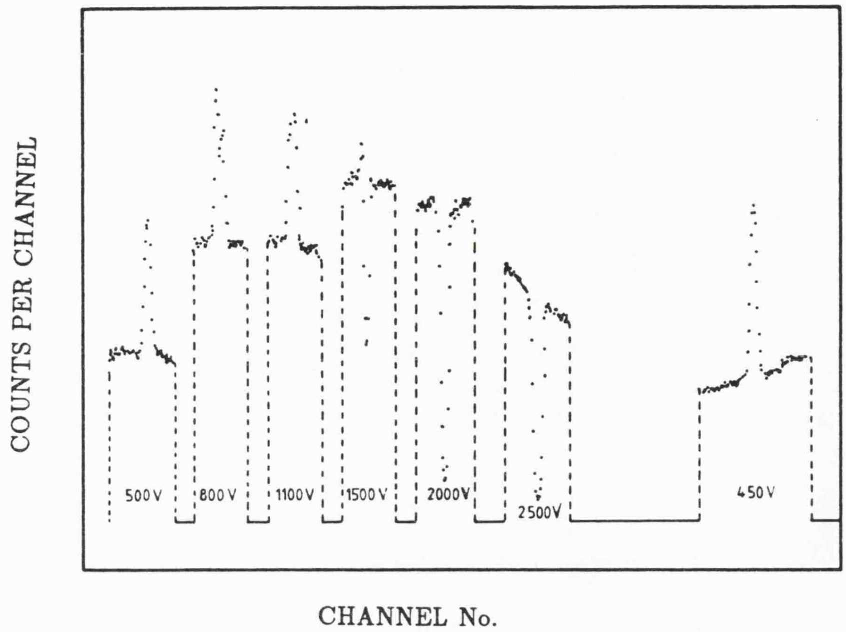

Figure 3.30:1 Change in the 30.4nm line profile with source voltage at a pressure of 4×10^{-3}mbar.

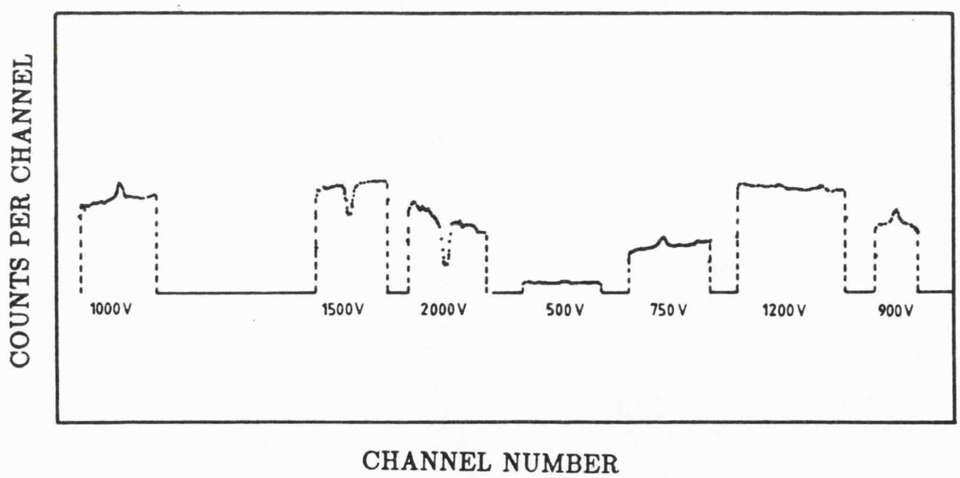

Figure 3.30:2 Change in 30.4nm line profile at a pressure of 10^{-3} mbar. Note: the vertical scaling is a factor of ten greater than in figure 3.31:1.

The grating having been vindicated by the observation of helium lines, some effort was put into producing lines in an argon discharge chiefly by trying to increase the discharge current. This was successful to a degree, but the line to background ratio was not very high as can be seen from figure 3.30:3. The lines observed were too close together to be easily identified, the emission lines of argon are not as distinctive as those of helium and the technique of measuring wavelength used so far was not accurate enough to differentiate between closely spaced lines. The clarity of argon lines was found to increase with time, presumably because of the source warming up.

As argon was found to emit its brightest line at long wavelengths (of the order of 90–100nm) it was decided to look for UV lines from other gases, notably helium, nitrogen and air. These features were not only potentially useful for detector calibration they may also have been the cause of the continuum at short wavelengths, by scattering through the monochromator grating and exit slit assembly.

It had been observed during optical alignment that there were numerous paths by which stray light managed to find its way around the exit slit and grating onto the source slit screen, and it was thought probable that there were equivalent leakage paths for light travelling in the opposite direction. Visible light would be unlikely to affect the detector as CEM efficiencies are low at optical wavelengths[3], so the offending background was thought to be of higher energy. XUV light shorter than a few tens of nanometres in wavelength would not scatter efficiently from the machined stainless steel surfaces that predominate inside the monochromator so this left UV light in the wavelength range 30–200nm. In fact CEM quantum efficiencies are also very small for wavelengths longwards of 120nm[3].

The argon spectrum in figure 3.30:4 shows about twelve lines in the range 50–100nm, the two bright lines at the righthand end of the plot are probably a pair of ArII lines at 91.98nm and 93.2nm respectively. Those at around 67nm and 72nm were also tentatively identified as ArII lines. All other lines are too easily confused to identify without more accurate wavelength measurement.

Long wavelength lines were also observed in helium and air discharges. Those in helium were around 121.5nm and it was concluded that these were most likely to be the Lyman series of hydrogen because although neutral helium does have a pair of lines around 121.5nm they are known to be weak[6] and also those observed always appeared in association with another line at about 102.5nm consistent with the second hydrogen Lyman line. Hydrogen would be expected to be present in the vacuum system because unless baked, water has a tendency to remain adsorbed onto the walls of the vacuum vessels[5]. The lines observed in air also included the hydrogen series with a few unidentified additions one of which was possibly the 130.2nm OI line.

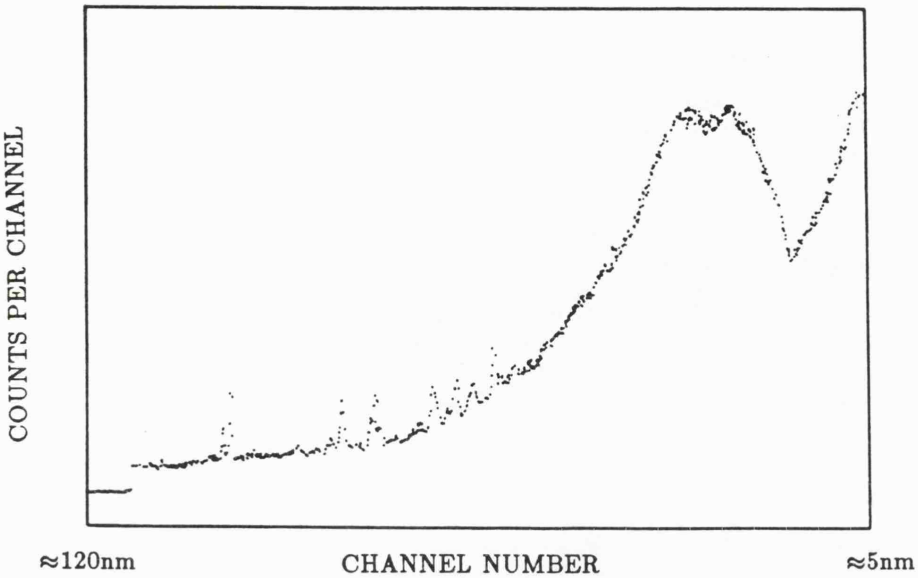

Figure 3.30:3 Argon spectrum between 5 and 120nm showing poor line to background ratio.

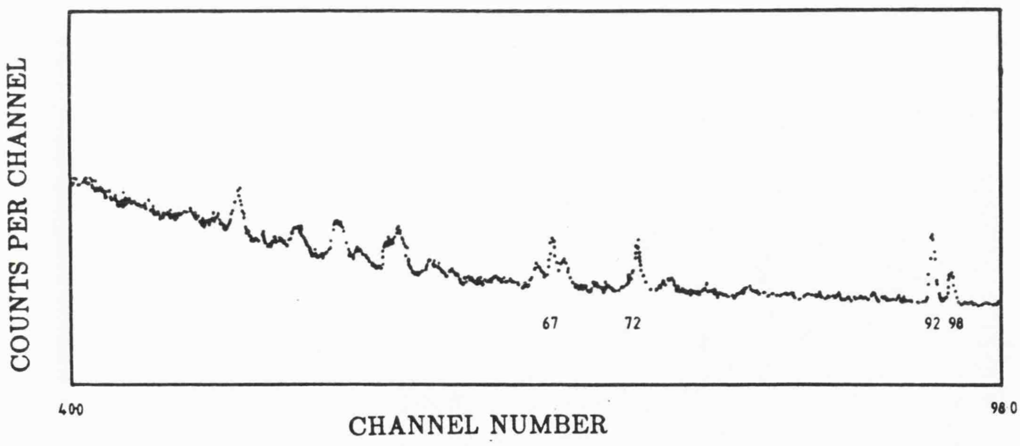

Figure 3.30:4 Argon spectrum between 45 and 98nm showing identified ArII emission lines.

3.31 Reduction of the Continuum Background.

No mention had been found in the literature of continuum emission by a Penning discharge and so the presence of such a background in all dicharges so far recorded was disturbing. It was thought possible that this might be due to the types of discharge thus far observed being not of the Penning type, a conclusion supported by the marked difference in currents produced in our source compared with those reported elsewhere[1].

A major source of background in any spectroscopic instrument is scattering, either of the spectral line being observed or of stray light from the source. It has already been noted that the CEM is vulnerable to light in the waveband 30–120nm since this is the most likely to be scattered through large angles from the monochromator surfaces. To exclude such light is usually a matter of effectively baffling the instrument so as to block its path. This approach was considered for the monochromator but it was found that due to its contruction there were few places within its vacuum vessel where such baffles could be accommodated, at least not without removing the grating mount which would have necessitated realignment. Repeating the optical alignment was not an attractive prospect for the reasons that it was both arduous and time consuming, the latter being the most damning reason because the ROSAT schedule would not allow it.

Another objection to the introduction of baffles was that it was unlikely to be effective unless an angled surface on the grating mount was somehow rendered nonreflecting, as this was thought to be a prime scattering surface. To clarify this point consider figure 2.61:2, it shows the offending surface and its position with respect to the grating. It can be seen that if an emission line is being observed through the exit slit then any line closer to the grating normal is likely to hit this surface and be scattered, maybe through the exit slit. Such a line is the zeroth order spectrum, extremely bright compared with the first order spectrum and of course not dispersed so it contains all the wavelengths that will scatter best. In addition to the removal of the grating assembly a solution to the problem would entail substantial remodelling of the support structure. This is perhaps something to consider for the future.

Another possible cause of scattering is the grating itself, this is possible even for a 'perfect' grating because the grating supplied with the instrument is blazed at 30nm. A blazed grating has the form shown in figure 3.31:1 with the elements making up the surface angled with respect to the macroscopic surface of the grating. The wavelength corresponding to specular reflection from each microscopic element is then the blaze wavelength of the grating.

If a blazed grating is illuminated so that the light strikes it along the long edge of the 'saw-tooth' then the diffraction will be clean. However, if the light strikes from the opposite direction then at shallow

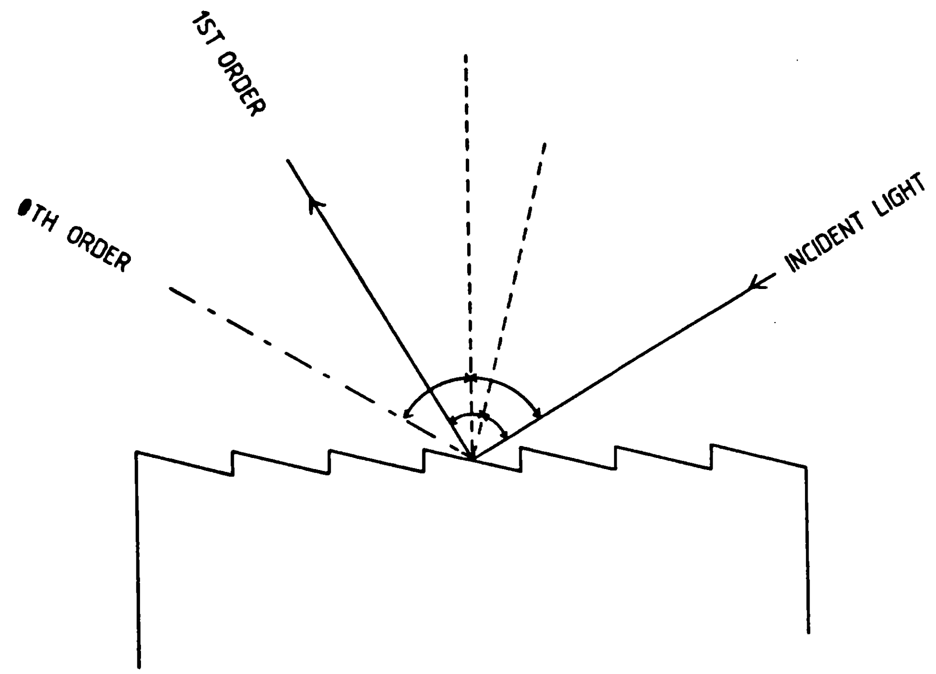

Figure 3.31:1 The microscopic form of a blazed grating.

angles particularly (ie. approaching zeroth order) there will be scattering from the short edge of the saw-tooth. Of course for a real grating the saw-tooth deviates from the ideal case illustrated resulting in scattering from angles further from zeroth order.

The correct orientation of the grating is marked on the end of the glass block on which it was fabricated but since the manner of use is not that normally experienced by the manufacturer, it was possible that they had installed it incorrectly. On examination however, the markings on the grating corresponded with the correct orientation and indeed when its orientation was reversed, no appreciable change in background was observed.

The inclusion of a simple baffle between the source slit and grating, however, restricted light to the grating surface only, and this confined the background to the region shortwards of 25nm in wavelength. This seemed to suggest that stray light was indeed the problem and that further improvements would be forthcoming if the detector were positioned further from the exit slit and some form of collimation adopted. Unfortunately, it was not possible to do this immediately but a marked improvement in short wavelength background was observed when the monochromator was attached to the mirror and detector test facilities (see, for example, the specta of sections 3.72 to 3.74).

3.32 Modifications to Increase Discharge Current and to Improve Reliability.

Continuing source instability at higher pressures when trying to increase the discharge current had indicated that a resistance stabilizer was necessary. The principle upon which such a device relies, ie. limiting the current drawn by the source, inevitably means that the resistor must dissipate a substantial proportion of the power drawn from the supply. This power, perhaps 2kW, must be got rid of somehow and the conventional approach is to include a fan to blow air over the resistor elements cooling them.

The solution adopted consisted of thirty six 50Ω 50W wirewound resistors mounted on heatsinks which formed a rectangular section tube through which a fan blew air. The resistance of the unit was 1800Ω which made a total of 2100Ω when the series resistor inside the power supply was included. Because the resistors used have a maximum rating of 2kV, the supply voltage was limited to around this figure.

The lull in activity brought about by the building of the ballast resistor enabled an investigation of the shortcomings of the monochromator stepper motor leadscrew mechanism. It was found that the torque required to turn the lead screw so as to extend the source slit bellows was almost the design torque of the stepper motor, and that the motor was not actually achieving this value. Stepper motors work by the application of current pulses to one or more of several windings, with a set phase relationship between the signals applied to the various coils. As it happened the circuit originally used to drive the motor did not comply with this sequence and so a new circuit was constructed. This circuit used simple TTL devices to provide control to the original current driver circuit and the old logic board was discarded.

Several useful features were built into the new driver: for instance, microswitch endstop controls, and variable sweep rates. A circuit diagram is reproduced in figure 3.33:1.

Another problem with the stepper motor was that whenever the power to it was switched off the motor would lose all holding torque, with the result that the tension in the evacuated bellows would send the source table crashing back to its stop. This could also occur because the torque of the motor was only just sufficient when running slowly to turn the leadscrew and when running quickly was much less. The answer was the inclusion between motor and leadscrew of a worm-reduction gearbox; this prevented running back even when the motor windings were not energised.

Inserting a series resistor in the PS circuit had an immediate effect, the spectrum shown in figure 3.33:2 is of a helium discharge operating at 180mA and 700V the source pressure was 5×10^{-3}mbar. This discharge was not sustainable for very long because it was found to be very difficult to maintain a constant source pressure but at least the discharge current had been pushed above 100mA.

In order to establish higher currents at low voltages it was found to be necessary to increase the pressure to beyond the point at which the PS backing pump failed to cope. Restricting the PS pumping aperture by means of a disk of aluminium sheet with a 6mm hole drilled through it helped a little, but not to the extent of drastically reducing the backing pressure problem.

A restricted PS pumping port also improved the argon pressure, and together with the ballast resistor this enabled discharge currents in the range 100–200mA to be attained. The resulting high detector count rates resulted in a severe loss of CEM gain and rather high MCS dead times. Gain loss in channeltrons is a well documented feature of their operation [7] which results from field distortion in the multiplier channel due to the charging up of the channel wall. Placing a piece of low transparency nickel mesh in front of the CEM input cone solved the problem by reducing the beam strength by approximately 99%.

Spectra recorded of 200mA argon dicharges still failed to exhibit any lines shortwards of 45nm. This was a cause of great concern as the reported strength of the PS was its ability to produce lines below 20nm in wavelength, particularly from aluminium ions created from material sputtered from the cathodes. The two principal series of helium containing the shortest lines yet observed could be more conveniently produced using a hollow cathode source[8].

Possible reasons for the lack of high energy lines were the background shortwards of 20nm which

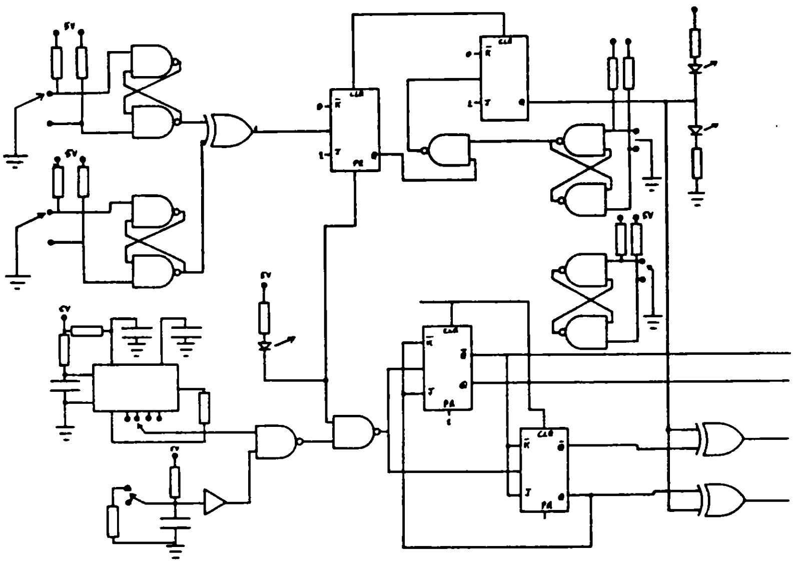

Figure 3.33:1 Circuit diagram of a stepper motor controller constructed using TTL components.

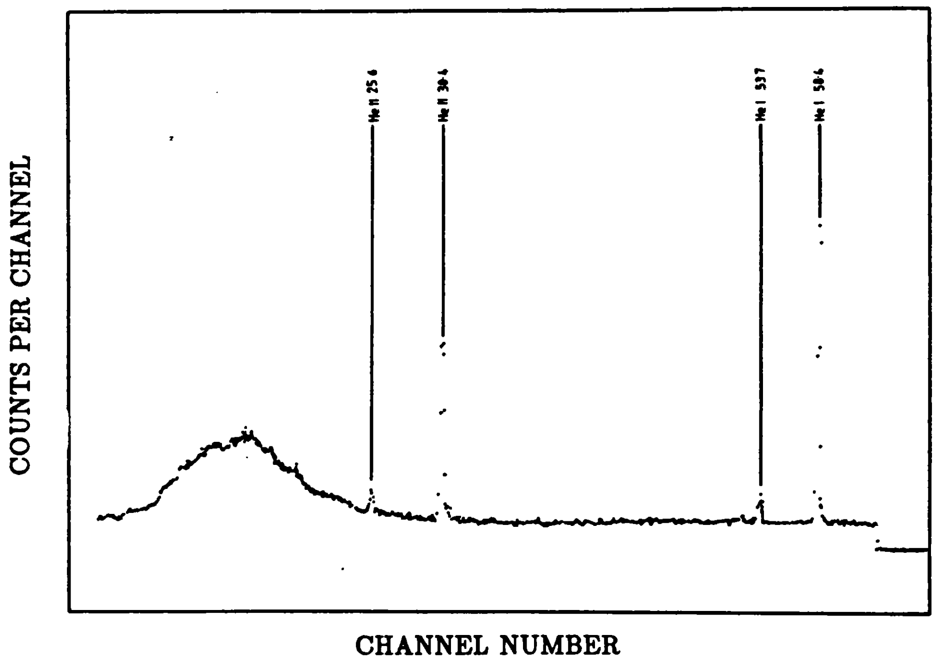

Figure 3.33:2 Helium spectrum between 10 and 60nm generated by the PS operated at 180mA.

has already been discussed, and the fact that the discharge current still fell short of expectations. The spectrum in figure 3.33.3 is of an argon discharge at 140mA and 800V with a source pressure greater than 10^{-4}mbar. The broad background peak is clearly shown and it is evident from the figure that there is some structure present. Indeed the structure was more apparent when spectra recorded under differing conditions were compared, for example there is a differance between figure 3.33:3 and figure 3.33:4 which was recorded at the same pressure but at 700V and just 80mA.

Stable discharges in argon were established for long periods usually in the range 200–250mA. After an accumulated run of several hours the source had attained a maximum current of 300mA when the current suddenly dropped to about 100mA and the discharge became erratic. The signifcance of this was unfortunately not immediately realised and lengthy attempts were made to relight the source but with no success. On opening and examining the source the reason for the abrupt change became obvious, the aluminium cathodes had been eroded completely through and with the effort to re-start the discharge some damage had been caused to the underlying brass cathode body. Fortunately the damage was not so severe that a hole had been burned through to the water jacket, but the remaining metal was only about 0.5mm thick.

Had the water cooling jacket been ruptured the result would have been catastrophic. The admission of liquid water into a diffusion pumped grating monochromator can be a very expensive mistake!

3.40 High Current Discharges in Neon.

Having failed to find the short wavelength lines in an argon discharge which were so essential to the WFC detector and mirror calibrations, it was suggested by Dr. B. Kent of RAL that a neon discharge might be more successful. He operated a more or less identical source to the Leicester device at RAL and had found that neon was an easier gas in which to initiate a high current discharge. Following Dr. Kents advice a cylinder of neon was procured and the resulting high current discharge lead to the spectrum reproduced in figure 3.40:1.

The spectrum was recorded using a discharge current of 350mA at 1.3kV with a source pressure of just 1.5×10^{-3}mbar. Although many lines are present there are none above the background below about 20nm, this was somewhat disappointing but the low pressure at which the discharge was established and its stability indicated that the current might be pushed up easily. This hope proved well founded as the spectrum of figure 3.40:2 demonstrates. In this spectrum there are numerous long wavelength lines as before but this time there are clearly two distinct raised features coincident with the top of the background peak.

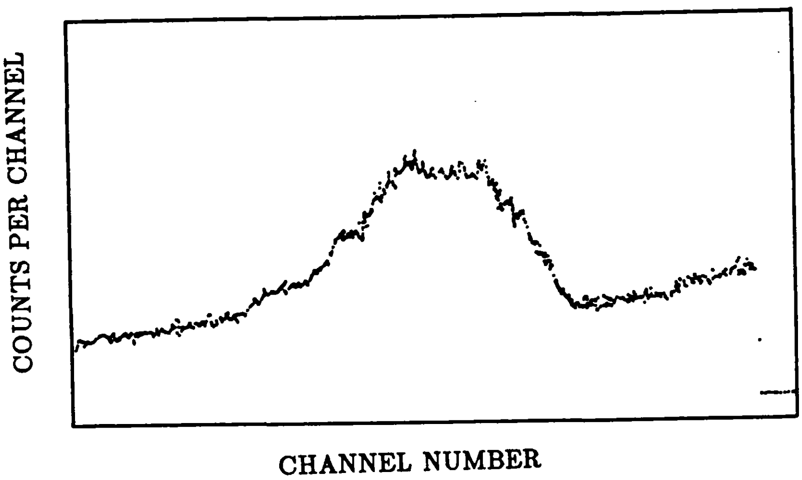

Figure 3.33:3 Spectrum of an argon discharge at 140mA, recorded between 5 and 30nm, showing the broad background peak.

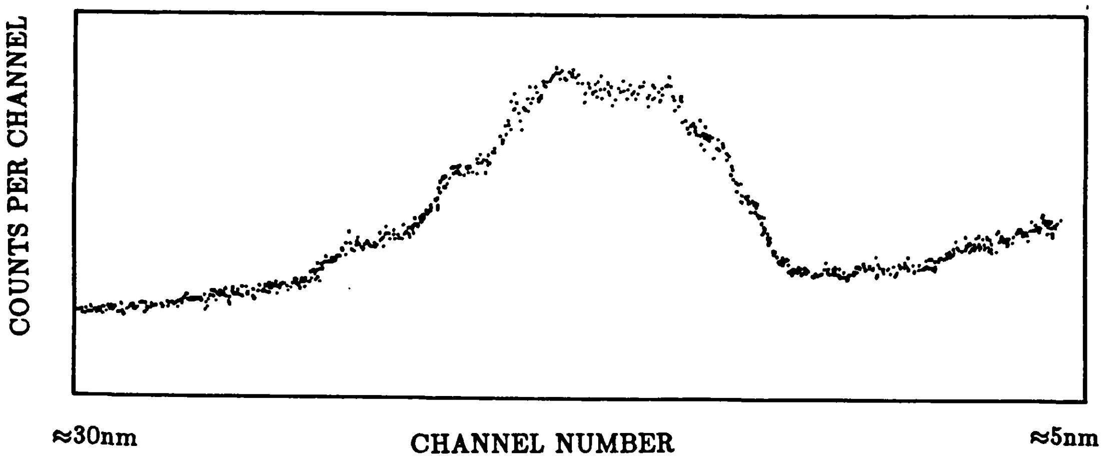

Figure 3.33:4 Argon spectrum between 5 and 30nm from an 80mA discharge.

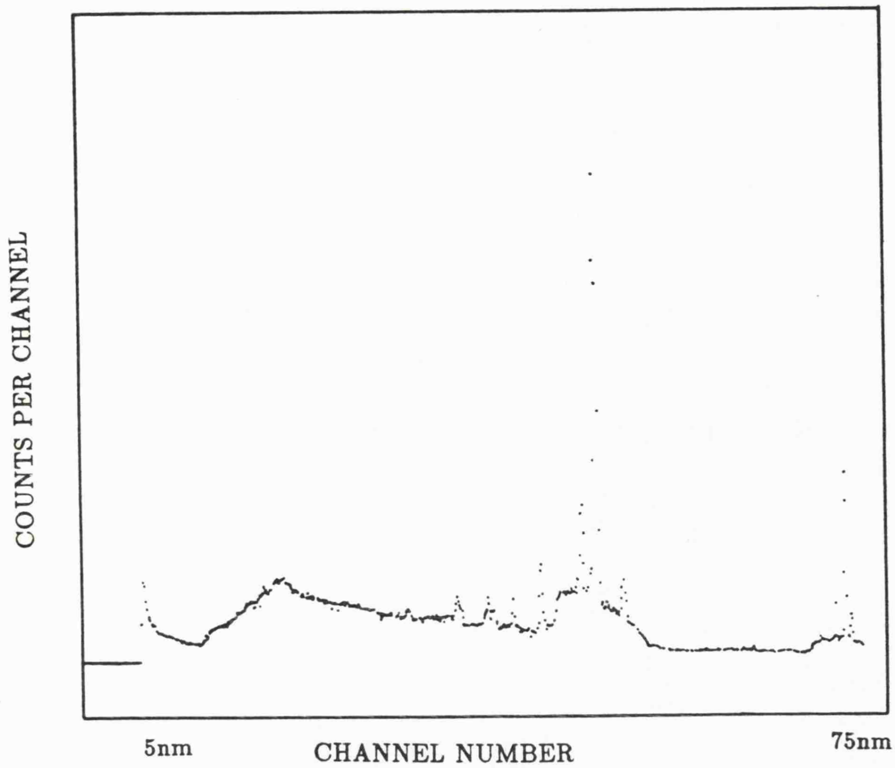

Figure 3.40:1 Neon spectrum from a 350mA discharge between 5 and 75nm.

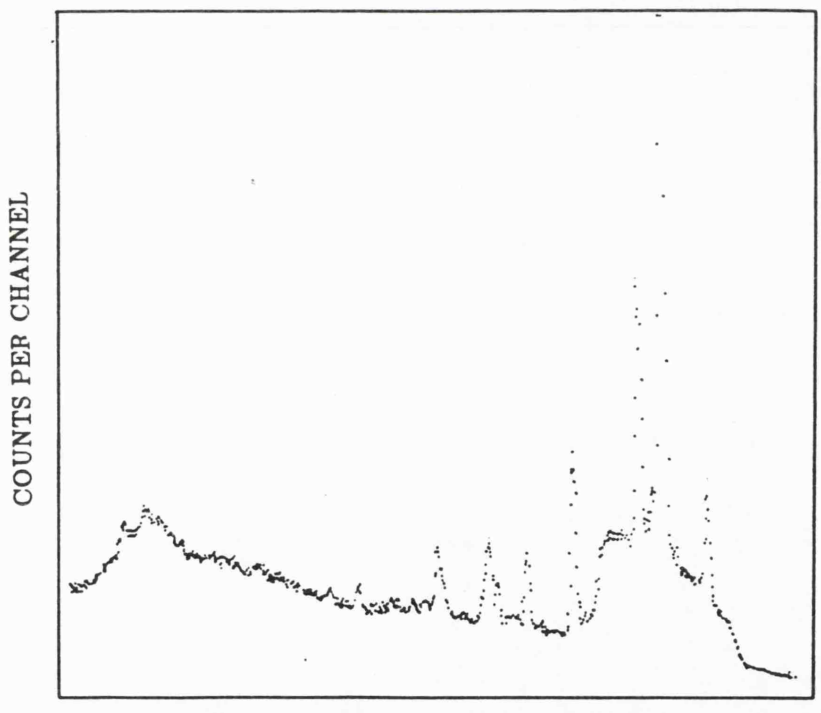

Figure 3.40:2 Spectrum of neon discharge showing lines at approximately 16nm

Observing two short wavelength lines as well as many longer wavelength lines highlighted the problem first encountered when looking at the lines in the argon discharge, ie. the problem of identifying the features. The next section outlines the technique used to accurately measure the wavelengths of lines and so lead to unambiguous identification.

3.41 Precise Wavelength Measurement.

Measuring the wavelengths of lines by finding the approximate point at which they occur as indicated by the position of the source table with respect to some marker on the base plate arc was clearly only of limited accuracy. It was only satisfactory as long as there were few enough lines for their identification to be straightforward. When it was possible for ions of several charge states to be present, as in the case of argon and neon discharges, the resulting crowd of lines became impossible to sort out. What were needed were a number of features of known wavelength which could be superimposed on any spectrum so that the MCS output could be directly calibrated in wavelength. The obvious choices were the 30.4nm and the 58.4nm lines from helium.

To include helium features in a neon spectrum a discharge was first established with neon alone, and then helium was bled into the neon supply to the PS. After some experimenting with the relative pressures of neon and helium in the PS gas feed line it was found that the normal long wavelength spectrum of neon could be preserved while the two major helium lines were visible. In figure 3.41:1 the 30.4nm and 58.4nm lines are picked out and by comparing the graph with that of figure 3.40:1 it is clear that they are additional features brought in by the inclusion of helium.

Marker lines having been inserted into the MCS trace it was then a simple matter to calibrate the spectrum in terms of wavelength instead of channel number. Each MCS channel represents a constant time increment so the trace represents count rate vs. time. The stepper motor operating the source table also runs at a constant rate so there is a fixed relationship between channel number and the change in length of the chord joining the source slit pivot with the grating pivot (figure 3.13:1). Referring back to figure 3.13:1, the length of the chord AB determines the angle the source slit subtends at the grating and so the wavelength. Relating the length AB to the wavelength via the grating equation:

$$d(sin(a) - sin(b)) = m\lambda$$

gives:

$$cos(b) = \frac{(AB/2)}{R}$$

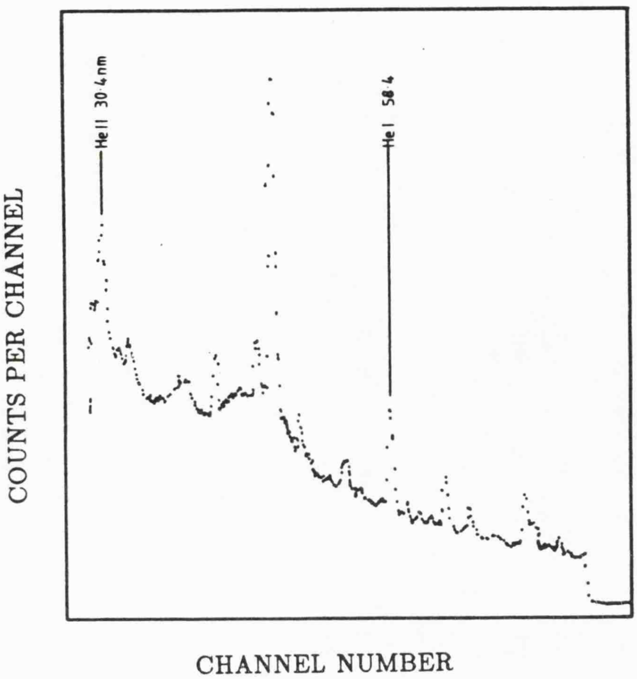

Figure 3.41:1 Spectrum of neon + helium with 30.4 and 58.4nm lines indicated.

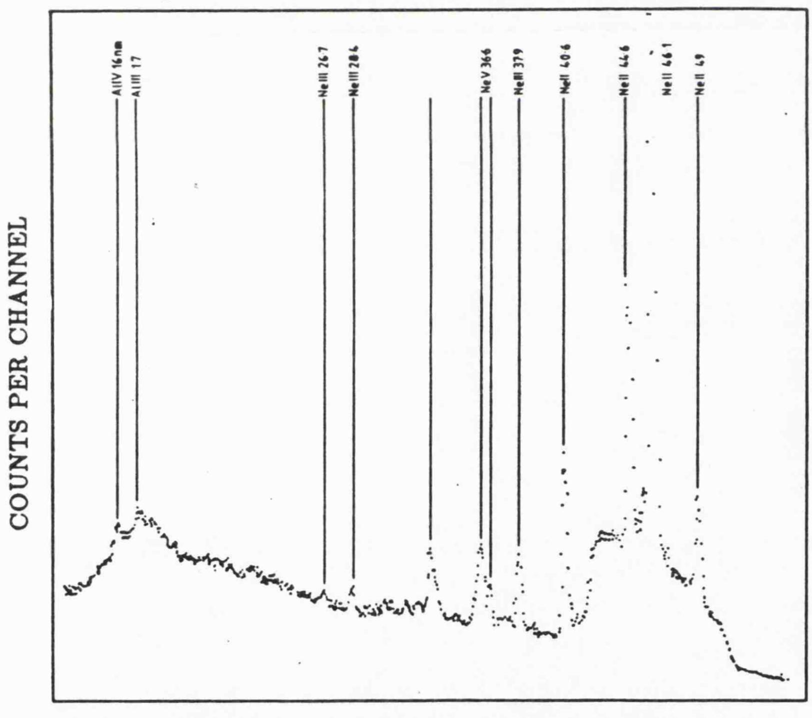

Figure 3.41:2 The spectrum of figure 3.40:2 with identified lines labelled.

therefore:

$$d\left(sin(a) - \sqrt{\left(1 - \frac{AB^2}{4R^2}\right)}\right) = m\lambda$$

since the stepper motor runs at a constant speed then:

$$AB = kt + c$$

where t may represent time, or equivalently, channel number. Substituting the expression for AB into equation 3.41:1 then gives an expression for wavelength in terms of t, plus of course the constants k and c:

$$m\lambda = d\left(sin(a) - \sqrt{\left(1 - \frac{(kt + c)^2}{4R^2}\right)}\right)$$

The values of k and c for a given MCS trace can be determined quite simply from the channel numbers and wavelengths of two known lines.

This technique was applied to the spectrum of figure 3.40:2 with the result that the two short wavelength lines were identified as the AlIV lines at 16.8nm and 16.01nm (unresolved) and with the group of AlIII lines between 17nm and 18nm. In fact all the lines in the figure were identified and figure 3.40:2 is reproduced as figure 3.41:2 with the lines labelled. By inserting helium lines into the spectrum in this way it was found to be possible to determine wavelengths to an accuracy of about 0.1nm. It is in fact only necessary to identify two well spaced lines in the discharge of any single gas before the whole spectrum can be classified, since the two identified lines then determine the wavelength scale for the rest of the spectrum.

3.42 Enhancement of Al Lines in the Neon Spectrum.

The observation, at last, of the aluminium lines in the neon spectrum prompted a search for the conditions which would produce the best line to background ratio. In the first few spectra to contain the aluminium lines the features were not strong enough above the background to be of any real value experimentally. To try to improve things, the discharge current was pushed higher and higher by elevating the source pressure. Ultimately currents of the order of 800mA were attained but at the cost of a higher source pressure which resulted in a decline in the observed line strength because of the inhibiting effect on aluminium sputtering[4].

Figure 3.42:1 shows the best results obtained at a source pressure of 1.1×10^{-3}mbar 2.2kV with a discharge current of 660mA. As can be seen both lines (or groups of lines) are well clear of the background but it was still not good enough to allow unambiguous quantum efficiency measurements to be made. The reason for the low line to background ratio was thought to lie in the low sputtering rate of aluminium by neon.

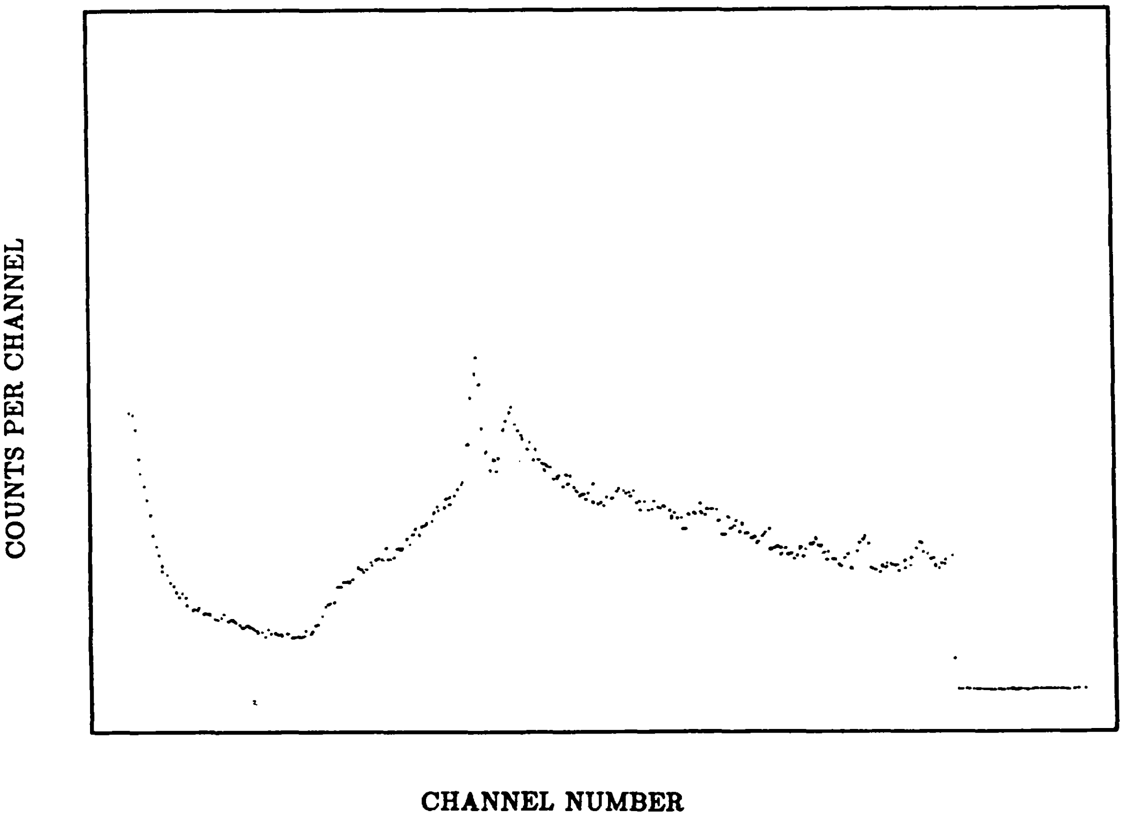

Figure 3.42:1 Neon/Aluminium spectrum showing the most prominant Al lines observed.

Although it is more effective in this respect than helium, argon was well known to be a better gas for the purpose of getting the cathode material into the plasma region.

3.50 High Current Argon Spectra.

Some difficulty was experienced at first in increasing the discharge current with argon, but this was eventually achieved by gradually increasing the source pressure and voltage so that when the current was about 450mA it became possible to see the aluminium lines. Straight away the improvement over neon at equivalent discharge currents was apparent, the lines being about a factor of two brighter. The process of increasing currents was continued with corresponding rewards in line emission, but it soon became apparent that this was to be at the cost of source operating time as it was discovered that cathodes could be eroded through in a matter of an hour or so.

Figure 3.50:1 shows the aluminium lines obtained from an argon discharge, the current is somewhat lower at 450mA for the pressure of 4×10^{-3}mbar than was typical because the source was 'well run in'. The lines are shown as they appeared through each of four exit slits, the widths of each are printed under each spectrum.

Initially the monochromator was equipped with only one exit slit set at 100μm, but it was thought that where a poor signal to noise ratio persisted this might be too narrow. Indeed a significant improvement can be seen in background for the 200μm slit over the 100μm case with just a slight loss of resolution. The loss of resolution with the 350μm case is more significant (about 1nm) but it was anticipated that this would be of little importance for some measurements. A 50μm slit was included to try to resolve the component lines in each major peak but this was not successful, and since there was an accompanying loss in line to background ratio this idea was not pursued further.

The design of the new slit plates was different to that originally installed because it was discovered that the shallow angled edges were contributing to scattering close to strong lines. This is illustrated in figure 3.50:2 where it is shown that it is possible for light passing through the slit to be reflected off a 5 degree slit face to increase the background whereas this is less likely with 45 degree plates. The existing 100μm slit was also modified.

Several other measures were tried in order to reduce background. One of these was the introduction of a filter between the exit slit and the detector. The filter was approximately 300nm thick, supported on a high transparency mesh and constructed from about 200nm of 'Lexan', a polycarbonate plastic, with a top coating of carbon. It was hoped that if the background was soft UV the it would be excluded by the filter, but this was not found to be the case. In fact the filter had very little effect at any wavelength,

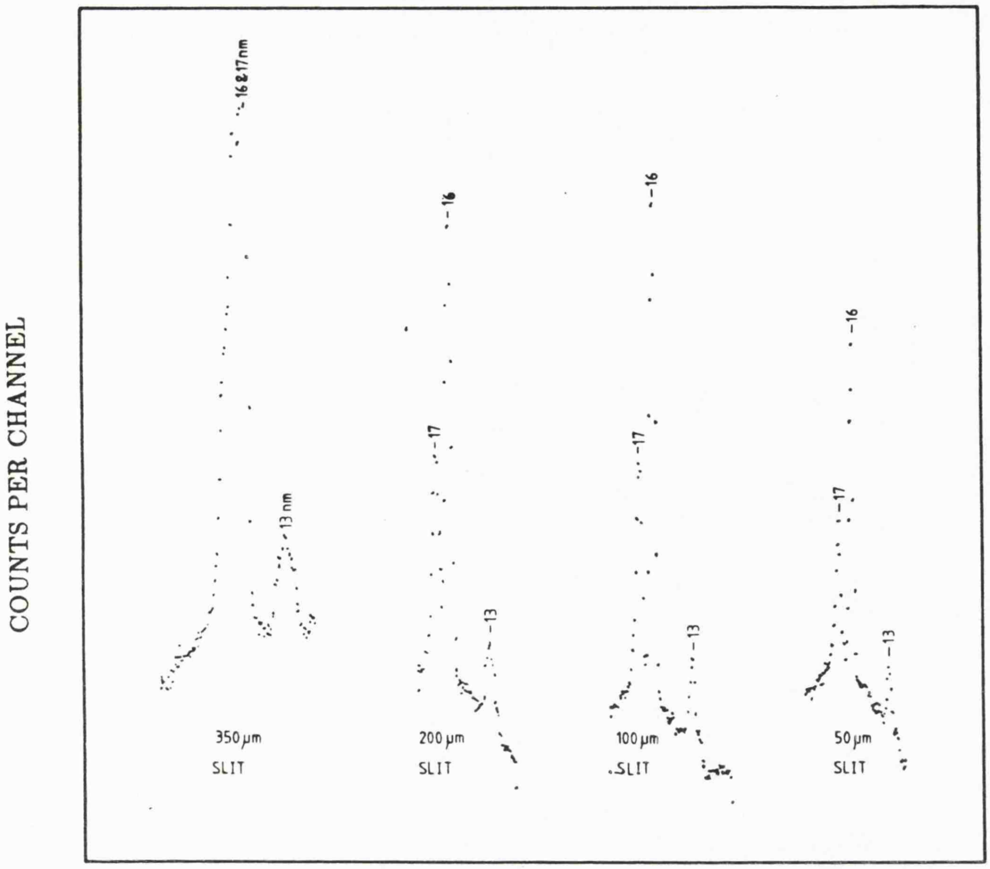

Figure 3.50:1 Aluminium lines observed in the spectrum of argon with different exit slit sizes.

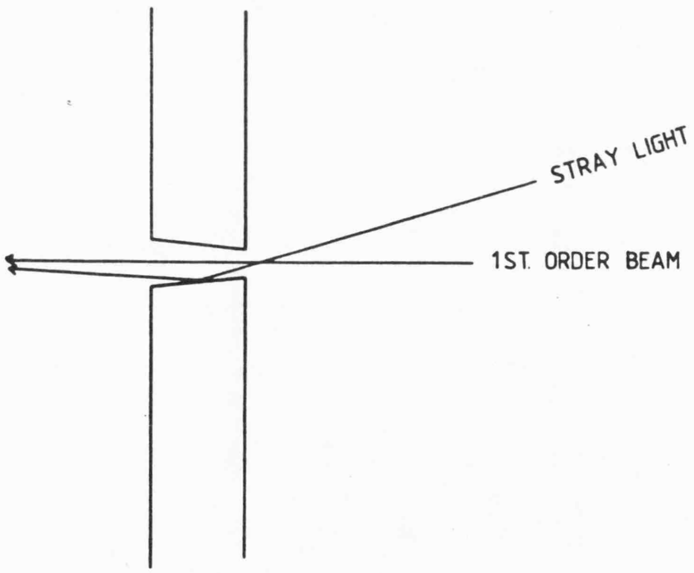

Figure 3.50:2 Scattering of line emission from 5 degree slit plate edges.

an observation which leads to the conclusion that the background is mainly XUV and/or that the filter is much thinner that was thought. This latter hypothesis is likely since the filter was cut from an early filter fabricated for the wide field rocket camera described by M. A. Barstow in his Ph.D thesis[9], and no record exists of its manufacture.

3.60 Further Vacuum Modifications.

With experience of PS running it became possible to reliably excite the aluminium lines between 12 and 20nm using the argon discharge. The apparatus described up to now was therefore used for the standard channeltron calibration and the microchannel plate detector calibrations that will be described in chapters 4 and 5. However, experience with windowless photodiodes (chapter 4) showed that with a diffusion pumped system, particularly with that on the PS untrapped, oil contamination of sensitive detectors and optics was inevitable. It was therefore decided to eliminate at least the PS pump from the system.

The flexible vacuum hose between the PS and its diffusion pump (figure 3.13:3) was removed and the source pumping port was sealed using a 'perspex' blanking piece. This viewport later proved useful in monitoring the state of the discharge.

The immediate effect of the removal of the PS pump was a decrease in the ultimate pressure attained in the monochromator. This was due to the elimination of the leaky flexible pipe.

Control of monochromator pressure when bleeding helium into the source was found not to be too difficult, indeed somewhat easier than it had been with the source pumped independently. Difficulty in controlling pressure in the pumped source was probably due to the stalling effect of the diffusion pump when overloaded. Often on being over pressurized the pump would stall and take just a second or so to start again, by this time the operator would have reduced the gas flow so that the pressure was too low. Setting a relatively high pressure could thus take some time. Without the PS pump the source pressure was easily controllable over the range 10^{-6} to 10^{-3}mbar as indicated on the monochromator penning gauge. The pressure in the source at these limits would be approximately 10^{-4} and 10^{-1} mbar. The ease of pressure control made it far easier to strike the discharge.

With argon, pressure regulation was almost as easy although it was observed that if the pressure was allowed to rise too much some delay would be experienced between shutting off the gas feed and the pressure recovering. Presumably this was a consequence of the lower conductance of the monochromator source slit for argon compared with helium. The conductance of an aperture varies as the mass of the gas molecule to the power $-1/2$[5].

For XUV tests on the WFC mirrors it was decided to convert the monochromater to turbomolecular pumping. As far as the vacuum performance of the system is concerned this had very little effect, but some possible effects on the spectra recorded are reported in the following sections.

3.70 A Summary of Penning Source Operation.

It is appropriate at this point to gather together the salient points about Penning source operation under the headings of the gases used and to make a few general points about PS operation. Hopefully this will clarify the techniques required for each gas in order to optimise line emission and ease of use. Firstly, however, it is instructive to compare notes with other authors who have described similar sources.

3.71 Other Cold Cathode PIG Sources.

J. R. J. Bennetts paper[10] has already been cited as an example of the use of PIGs as ion sources. This review also demonstrates the wide variety of designs that were used (PIGs have largely been superseded by other types of source for this application), particularly with regard to the cathode arrangement. For example, many sources were of the hot cathode type with the cathodes heated either electrically or directly by the discharge, and many were operated in a pulsed mode. The type of source used at Leicester was a continuously run cold cathode design so examples of this type from the literature will be compared here with the Leicester source.

Two experimental investigations of cold cathode sources illustrate some of the phenomena observed with the Leicester source. The first of these was conducted by J. Backus[11].

Backus observed two types of discharge; one at low pressures with currents of a few milliamperes and the other a high current discharge at higher pressures. The transition between modes was abrupt with changing pressure. This observation is in broad agreement with the behaviour of the Leicester source though the high current discharge could also demonstrate two modes which have been noted by other investigators[12]. The high current modes were characterised by high currents and low supply voltage ($>$ 600mA and 1.5kV) or high supply voltage and lower currents ($<$ 200mA and 2kV), two modes were generally observed when the source had been run in (section 3.74).

The current voltage curves of Backus are also in good agreement with that of chapter 2, as is his observation that these were not quantitatively repeatable. Backus was also able to investigate the effect of varying the magnetic field strength, which was not possible with tha Leicester source, and he found that as long as it exceeded a critical value this had very little effect. Typically his source was run using a field of 0.2 Tesla.

By measuring the power delivered to the discharge by the power supply and the power dissipated by the water cooling to the cathode, Backus was also able to conclude that the current at the cathode was about 75% ionic, a conclusion with which Bennett is in agreement with for cold cathode sources[10] but which is in constrast with Shulte's measurements on hot cathode sources which suggest that the electron current dominates[13]. Cooling water temperatures on the Leicester source are consistent with most of the power being dissipated at the cathode, or equivalently with the cathode current being predominantly ionic.

Mass spectrometer measurements on the ion current extracted from Backus's source showed argon ions up to charge state 4^+ (Cu cathodes). Difficulties in identifying XUV lines from the plasma in the Leicester source make it difficult to be certain of the charge states present, but those definately identified are tabulated in the following sections.

The second investigation from the literature was by B. H. Wolf[14], and this included a study of the effect of changing the cathode material, gas fill, and the effect on extracted ion currents of varying source parameters. Wolf found that for high arc powers the discharge voltage increased with the atomic weight of the cathode material and the fill gas. The running voltage was observed to increase with current until an approximately constant voltage was reached, and the voltage also increased with gas flow (pressure).

The implications of these observations for the Leicester source are a consequence of the power supply limitations. For example, should it no longer be desired to use aluminium cathodes, so as to avoid their rapid erosion, the alternative materials are limited. In fact Wolfś measurements suggest that titanium would allow the source to be operated under similar voltage conditions but at a lower sputtering rate. This possibility has yet to be investigated experimentally.

The 3kV supply limitation also means that when aluminium sputtering is desirable for generation of aluminium emission lines, the source has to be operated at a higher than ideal pressure resulting in reduced sputtering efficiency.

Mass spectroscopic analysis of the charge states generated by his source enabled Wolf to come to the following conclusions about the influence of discharge parameters on the charge state composition:

1) Lower source voltages for a given arc power resulted in higher proportions of high charges states produced.

This suggests that in order to generate the widest range of emission lines, the PS should be run at the lowest voltage consistent with a stable discharge. It has been observed that the intensity of the HeI 58.4nm line may decrease with respect to the HeII 30.4nm line at lower voltages.

2) The proportion of high charge states increases rapidly with discharge current.

The observed intensity of short wavelength lines in the PS spectrum increases with current, consistent both with Wolfs observation and with the expected increase in sputtering resulting in increased aluminium line emission—a major contributor to the short wavelength spectrum.

3) The extracted high charge state current decreases with increasing gas flow (pressure).

This is also consistent with the short wavelength spectrum of the PS, though aluminium sputtering rate also increases with decreasing pressure. The limit to reducing source pressure is imposed by the decreasing stability of the discharge.

Measurements at Leicester and by other investigators demonstrate that the following general rules should be observed when operating a Penning discharge source:

1) A ballast resister (or a more sophisticated stablising device) is essential for the easy striking and running of the source.
2) To get stable high flux operation a large discharge current must be available, and this may mean that the source pressure will need to be elivated or the applied voltage increased accordingly.
3) Water cooling, particularly of the cathodes, has been found to be essential in view of the large arc powers used (typically 100 to 800W).
4) If a period of stable light output is required, an initial setting up period may be necessary during which continuous pressure adjustment is needed to achieve a steady state. Additional instrumentation may aid this goal, for example, a gas flow monitor might help to expedite matters.
5) Radio frequency screening has been found to be essential if the source is to be used near to microprocessor based equipment such as microcomputers, turbomolecular pump controllers, and some gauge controllers.

3.72 HELIUM.

Stable helium discharges can be established in two modes; high pressure and high current, or low pressure and low current.

For low current operation, helium is supplied to the source using the needle valve until the pressure is seen to rise on the monochromator penning gauge. Typically the current limit control on the HT supply is set to 200mA and the voltage control to 1.5kV, before switching on the HT. The voltage is then adjusted until a stable discharge drawing about 5mA is established. With the monochromator tuned to 30.4nm, this discharge has been found to provide a modest count rate of about 10 per second close to the exit slit, which corresponds to a flux of around 100 photons per second.

With the viewport fitted as in section 3.60, the ultimate pressure in the monchromator will be of the order of 10^6mbar. For high current operation helium may be admitted until a pressure of about 5×10^{-5}mbar is recorded on the monochromator penning gauge, care must be taken that the pressure does not rise above 10^{-3}mbar and that the backing pressure NEVER rises above 10^{-1} mbar. The current limit should be set to about 400mA and the voltage to 1.0kV; the HT is then switched on and the pressure adjusted to produce a stable discharge. If the source fails to strike, it may be lit by further increasing the pressure.

It is generally the case that during the first few minutes of operation, the pressure in the source will drop as it pumps itself to some extent. Discharge instability may result from the loss of pressure unless it is corrected, and this has been known to result in electrical interference particularly in microprocessor systems such as some gauge controllers.

When a stable discharge is established it may be desirable to increase the light output. This may be done by increasing the discharge current, either by raising the voltage or by increasing the helium pressure. A period of pressure adjustment may then be necessary to counteract the increased source self-pumping speed.

Operating the source with helium has been found not to produce significant cathode erosion, even after running for extended periods at high currents. The reason for this is presumably the low sputtering efficiency of helium, plus the fact that relatively high source pressures have been employed. Some cathode erosion does occur, but it appears to progress slowly. Typically, after some hours running the cathode surfaces will have a shallow surface depression (assuming that they have not previouly been used with argon) which has a shiny molten appearence. In addition, a grey or black deposit will have formed around the damage site and on the anode and this may need to be removed periodically.

Table 3.72:1 lists the emission lines, together with their approximate relative strengths and figure 3.72:1 shows a typical spectrum recorded using a CEM detector in the detector test facility (chapter 5).

An estimate of the absolute flux from the monochromator when tuned to 30.4nm, with the PS running with helium, can be derived from a typical count rate of 100 per second in the straight through beam of the Mirror Test Facility (chapter 6). Using a 90% reflectance for the Kirkpatrick-Baez collimator, 20% quantum efficiency for the WFC style MCP detector (chapter 5), and a collimator aperture of 4×4mm 2.0m from the 350μm exit hole (in place of the monochromator exit slit— see chapter 6), the

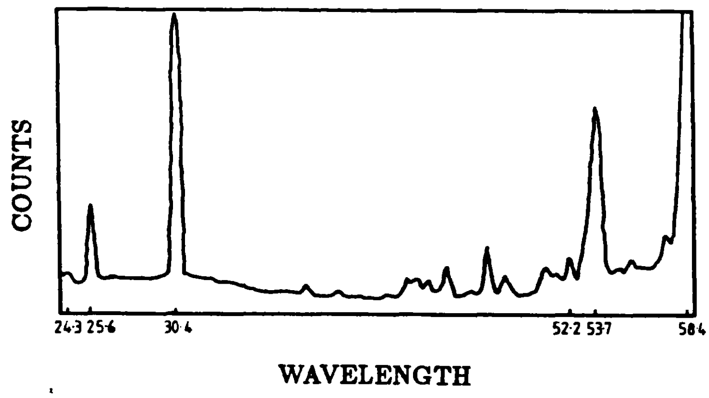

Figure 3.72:1 The spectrum of helium between 58.4 and 24nm showing the HeI and HeII resonant series.

TABLE 3.72:1

A list of lines obtainable from the PS/Monochromator with a helium discharge at high pressure.

Typical conditions are: Pressure 5×10^{-5}mbar, Voltage 1–1.5kV, Current 300–500 mA.

Wavelength/nm	Species	Relative strength*
30.378	HeII	100, V. strong
25.632	HeI	13
24.303	HeII	
58.43	HeI	100, V. strong
53.703	HeI	10
52.22	HeI	

* Relative strengths are quoted as a percentage of the most intense line in the observed spectrum of the ion species concerned.

An indication is given of the absolute intensity of bright lines in qualitative terms.

monochromator flux is of the order of 10^8 per second per steradian.

3.73 NEON.

Most discharges in neon so far investigated have been at low pressure (10^{-4}–10^{-5} mbar as measured in the monochromator) in an attempt to generate aluminium lines (section 3.42). It is certainly the case, however, that NeI and NeII lines can be generated at higher pressure.

To operate a neon discharge at low pressure, neon is generally admitted to a pressure of a few 10^{-5}mbar. The HT current limit typically used is about 500mA with the voltage set to 1.5kV. Should the discharge fail to strike when the high voltage is applied, the pressure can be increased until it does (keeping an eye on the foreline pressure). Once a discharge is established the pressure should be adjusted to achieve stability at the required current.

Cathode erosion does occur with neon, as evidenced by the presence of aluminium lines in the spectrum, but the timescale over which significant damage accrues is uncertain. Of course the rate of sputtering depends greatly on the discharge conditions, particularly on the pressure, as the erosion rate increases rapidly with decreasing pressure for a given current and voltage. Symptoms of severe cathode erosion are; difficulty in initially striking the discharge, and change to unstable conditions during running which cannot be rectified by adjusting the pressure or voltage. Should such a situation develope it has been found to be prudent to inspect the cathodes before proceeding.

The principal disadvantage in using neon is its high cost, It should therefore only be used to excite lines at wavelengths which are not available from other gases eg. 30–50nm. The emission lines available from a typical high current neon discharge at low pressure are listed in table 3.73:1.

Several lines in the neon spectrum are unidentified, and it has been found that in the MTF (chapter 6), where the signal to noise ratio is very high due to low scattering and careful image processing, useful lines have been observed in the vacinity of 20nm. Emission lines have not been observed in this wavelength range with other gases but those in the neon spectrum were too weak to be of use for the detector calibrations of chapters 4 and 5. However, for the mirror calibrations of chapter 6 the 20nm line proved useful in filling a gap between the 25.6nm HeII line and the 16nm AlIV lines.

Figure 3.73:1 shows a spectrum recorded in the mirror test facility, most lines are unidentified but their approximate wavelengths are indicated. Also with the MTF, spectra appear to differ from those previously recorded and it is possible that this is due to changed pressure gradients in the source as a result of pumping the monochromator with a turbomolecular pump rather than with a diffusion pump.

TABLE 3.73:1

A list of lines obtainable from the PS/Monochromator with a neon discharge at low pressure.

Typical operating conditions are: Pressure 3×10^{-5} mbar, Voltage 1.2–2kV, Current 350–800mA.

Wavelength/nm	Species	Relative Strength*
16.007	AlIV	Weak and unresolved
16.17	AlIV	Weak and unresolved
17.04	AlIII	Weak Multiplet
73.59	NeI	100 Strong
74.37	NeI	100
40.59	NeI	15
44.625	NeII	21
46.07	NeII	100 V. strong
37.93	NeIII	80
48.95	NeIII	100

* Relative strengths are quoted as a percentage of the most intense line in the observed spectrum of the ion species concerned.

An indication is given of the absolute intensity of bright lines in qualitative terms.

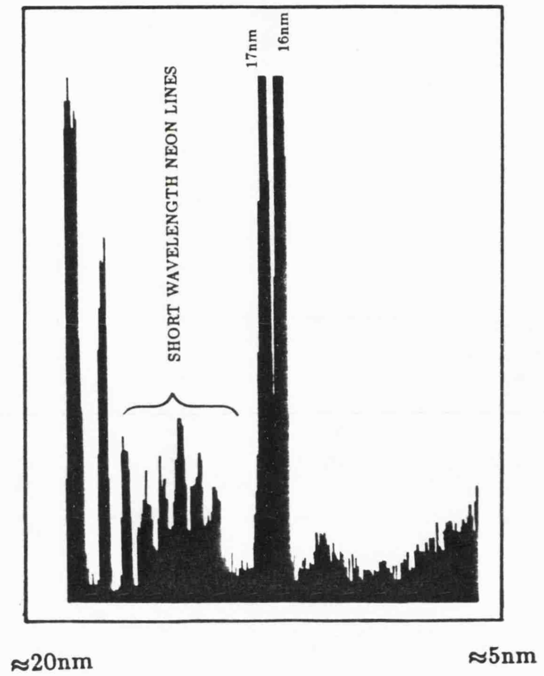

Figure 3.73:1 A neon spectrum recorded in the MTF between 14 and 45nm. Most lines have not been positively identified but approximate wavelengths are indicated.

This effect was first noticed in argon spectra and it is possible that the cause is contamination of the grating by aluminium. This is discussed further in the following section.

3.74 ARGON.

The argon discharge has been found to be a rich source of lines in the 50–70nm and 90–110nm ranges, but is principally used to obtain the 16nm and 13nm lines of aluminium. Aluminium ions build up in the argon discharge due to the high sputtering efficiency of argon.

The conditions necessary for generating the 16nm and 13nm lines are of high current at low pressure. Argon should be admitted to the source to a pressure of 10^{-4}mbar as indicated on the monochromator penning gauge and HT applied with a current limit of about 700mA and voltage of 1.5kV. If the source fails to strike, the source pressure can be further increased (in this case the monochromator foreline pressure should be monitored), and the voltage can be increased.

It has been observed that the initial current drawn can be quite high (as much as 700mA at a supply voltage of 1.5kV) but this decays over a period of a minute or so. After the current burst, due presumably to high initial gas pressure in the discharge region, it can be necessary to increase the pressure and voltage to maintain the discharge. During the course of half an hour or so it is found that the current increases and the voltage subsides, so that a satisfactory current can eventually be attained at low pressure. This 'warming up' period has been reported by Finlay[1] and others, and has been attributed to the existance of an oxide layer on new cathodes. During the warm-up the oxide layer is sputtered off, and if the source is not let up to atmosphere does not recur. The initial burn-in is thus only required when source is first used with fresh cathodes.

With the PS running with argon at high current it has been observed that two discharge modes are sometimes possible, and that the source may switch between them. These modes are characterised by high voltage and moderate current in one state, and by lower voltage and higher current in the other. By adjusting pressure and voltage, the source can be made to operate stably in one or other of these modes. The lower voltage state is preferable for exciting aluminium lines. To enhance aluminium sputtering always operate at as low a pressure as practicable.

Cathode erosion can be very rapid at pressures between 10^{-5} and 10^{-6}mbar and at currents of 600 to 900mA (V=1.5–2.5kV). Continuous running at this level will eat through the cathodes in 1–3 hours. Whenever the discharge becomes erratic, and cannot be stablised by a simple pressure adjustment, or if the source is unusually difficult to strike, it is essential to investigate the state of the cathodes.

Table 3.74:1 lists the emission lines obtainable from an argon discharge with aluminium cathodes. The 13nm aluminium line, although strong, was not intense enough to allow calibration of a CEM

TABLE 3.74:1

A list of lines obtainable from the PS/Monochromator

using an argon discharge operated at low pressure.

Typical operating conditions: Pressure 5×10^{-5}mbar, Voltage 1.5–2.5kV, Current 600–900mA.

Wavelength/nm	Species	Relative strength*
130	AlIII	Strong
160.07	AlIV	V. Strong unresolved
161.7	AlIV	V. Strong
170.4	AlIII	V. Strong, Multiplet
1048.2	ArI	100
1066.7	ArI	74
661.9	ArII	64
671	ArII	94
677	ArII	54
723.3	ArII	100 V.strong
730.9	ArII	37
740.3	ArII	54
745	ArII	44
919.8	ArII	63
932.0	ArII	40
637.3	ArIII	100 Moderate
696	ArIII	77
769.1	ArIII	85
878.7	ArIII	86

Wavelength/nm	Species	Relative strength*
Unidentified strong lines:		
467		
474		V. strong
487		"
501		
507		
519		"
543		"
557		"
574		"
579		"
597		
602		

* Relative strengths are quoted as a percentage of the most intense line in the observed spectrum of the ion species concerned.

An indication is given of the absolute intensity of bright lines in qualitative terms.

(chapter 4), and shorter wavelength lines in the aluminium spectrum were weaker still. The weak lines were in fact only observable in spectra recorded using the mirror test facility (chapter 6).

Figure 3.74:1 shows the long wavelength spectrum of the argon discharge and many of the lines are unidentified (Table 3.74:1). Figure 3.74:2 shows the short wavelength spectrum due to aluminium in the discharge.

It has been found, as with neon, that argon spectra in the MTF differ from those recorded in the DTF and with the CEM at the monochromator exit slit. The main difference is the absence of lines longwards of 60nm in wavelength, which is unfortunate as the ArII lines at 92 and 93nm were potentially very useful, as were lines around 73nm. A lack of long wavelength lines may be due to pressure changes in the source as a result of the different pumping environment (section 3.60), but a more worrying possibility exists.

It is well established that the reflectivity of aluminium declines towards longer wavelengths in the EUV region as a result of the build-up of a surface oxide layer. Aluminium is a prime candidate as grating contaminant because of PS cathode sputtering which has resulted in a deposite of aluminium forming on the monochromator entrance slit. This deposite can be scraped with a knife, indicating a considerable thickness-perhaps several μm. It is inevitable, therefore, that aluminium be deposited on the grating, though the amount is probably small given the size of the slit and the fact that no degradation has been observed in monochromator resolution. Further investigation of this problem is essential for future work.

As with the 30.4nm line of helium it is possible to estimate the flux to be expected from the 16nm Al doublet under typical source conditions. Using the figures quoted in section 3.72 and a MCP quantum efficiency at 16nm of 50%, the flux is of the order 5×10^7 per second per steradian.

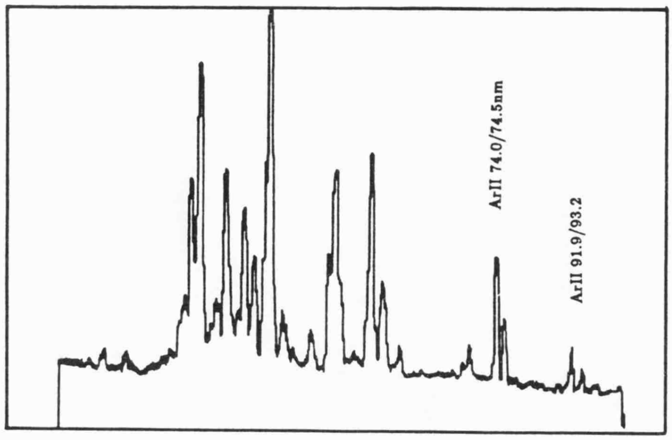

Figure 3.74:1 Long wavelength spectrum of argon between 5 and 100nm; several identified lines are labelled.

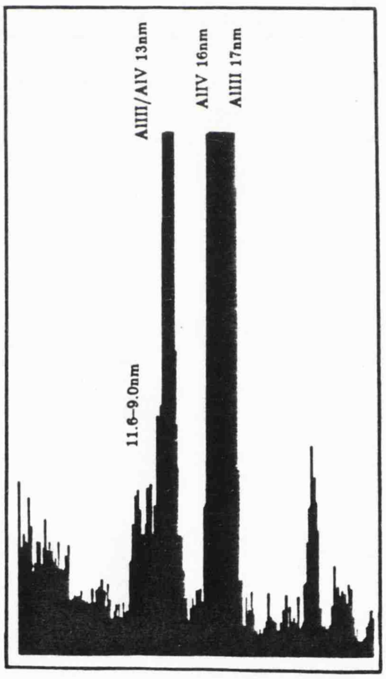

Figure 3.74:2 Short wavelength spectrum of argon discharge recorded in the MTF. The lines are due to the presence, in the discharge, of aluminium ions.

CHAPTER 4

The Production of a Laboratory Transfer Standard for the Measurement of WFC Detector Quantum Efficiencies.

4.10 Introduction.

The achievement of useful fluxes of XUV light from the Penning source as described in Chapter 3 meant that the ROSAT test program could be supported by the PS and the monochromator. In particular, as far as this thesis is concerned, it meant that a WFC MCP detector could, at least in principle, be calibrated and mirror reflectivities measured. All that was required in order to measure the quantum efficiency at various wavelengths was a knowledge of the beam strength in absolute terms so that the relevant detector count rate could be turned into an efficiency.

This seemingly simple requirement is the crux of any intensity calibration and the accuracy of the results depends on the precision with which the illuminating beam intensity is known. It is possible to measure source strength by comparing the unknown flux with that from a standard source, or by measuring it using a standard detector[1]. Standard sources in the XUV region are effectively limited to the synchrotron type and access to these is of course difficult to obtain. Standard detectors seemed then to offer most promise as far as the PS and monochromator were concerned.

Several reviews of XUV and EUV radiometry had been published (eg. references 1,2, and 3) and the detectors which appeared most reliable in terms of accuracy and stability in the wavelength range 5 to 100nm were the windowless photodiodes produced and calibrated by the National Bureau of Standards (NBS) in the USA. These detectors are calibrated using synchrotron radiation against a noble gas double ionization chamber[4,5], which itself could be used as a standard were the more convenient diode not available.

Simpler still than a photodiode would have been to use a photon counting detector such as a proportional counter or a CEM. Unfortunately a proportional counter is not as useful at long wavelengths as it is below about 10nm, because it is no longer an absolute detector since it is not possible to choose a window material which conbines low absorption with strength[3]. This means that a proportional counter like the CEM would require calibration before it could be used as a standard. This possiblity was investigated but it was found that there was no possibility of having this done by the NBS or by any facility in this country.

It was decided then to purchase a NBS diode as a standard, but its limitations dictated that a secondary standard would need to be produced from it. The reason for this was that a photodiode works by the emission of electrons from a photocathode by the photoelectric effect, these are then collected at the anode and flow as a current which can be measured. Typically, the quantum efficiency of this prosess is rather less than unity implying that fluxes of the order of 10^6–10^7 photons s^{-1} are necessary before the current can be measured with any accuracy.

In choosing the secondary standard several points were taken into account, these included the unreliability of thin windowed proportional counters, that no energy resolution was required, and that a great deal of confidence had been built up in the reliability and robustness of CEMs. Although having much to recommend them CEM's were also known to have drawbacks, for example, the loss of gain experienced at high count rates might affect the accuracy of results were the counting electronics not carefully set up, and the detection efficiency is known to be a strong function of conditions of illumination[6].

Variations in CEM efficiency occur with angle of incidence and position of illumination on the sensitive area, positional variability being most marked when the entrance to the multiplier channel is illuminated. This is because small changes in spot position produce large variations in angle of incidence effecting the production of photoelectrons and this influences the probability of a detectable avalanche occurring. In open cone devices, such as the Mullard B318 BL used as a monitor counter for recording PS spectra in chapter 3, varations in QE across the cone are less drastic away from the central channel but are nevertheless significant; these are the result of field distortion on the electron collection probability.

Mullards type B419 BL CEM was adopted as the secondary standard because it has been shown to have useful quantum effiency between 10nm and 100nm[7] and because CEM efficiency is stable at least over the time scales required of it for the WFC program[8]. Sensitivity to beam orientation was not considered to be too restricting as the calibration beam would have to be collimated to better that a degree anyway and a suitable CEM cone mask would ensure repeatable detector positioning. With this in mind, three Mullard detectors were acquired and on arrival were stored in a desiccated nitrogen atmosphere to insure against contamination.

Because of the difficulty anticipated in using the NBS detector it was planned to calibrate a B419 channeltron using the diode and the monochromator/PS, and then transfer this secondary standard to the Detector Test Facility (DTF) (see section 5.10) in which the detector calibration could be performed. The rest of this chapter will concentrate on the design, construction, and use, of apparatus to calibrate the secondary standard CEMs.

4.20 The Design and Construction of the CEM Chamber.

Calibrating one detector against another is simply a matter of measuring the strength of a beam of light with one detector, and then substituting the second detector and comparing the two measurments. If during the time taken to switch detectors the beam has remained constant, and if sufficient care has been taken that both detectors see the same part of the beam then a precise calibration will be achieved. This was the goal of designing a vacuum chamber in which to calibrate a CEM against the NBS photodiode.

Estimates of the monochromater count rate were made in order to decide where with respect to the exit slit the diode should be placed. It was known that typical CEM quantum efficiencies were of the order of 10%, so it was possible to establish that the monochromator and PS would produce a maximum count rate of about 10^6 photons per second over the B318 detector area of $25mm^2$ at a distance of 350mm, for some of the fainter lines. Such a small figure meant that for a complete calibration over the full wavelength range the diode would have to be placed as close as possible to the monochromator exit slit. Approach to the slit is limited by the vacuum hardware to only about 30mm, but it was not possible to come this close because a detector manipulation system had to be included to allow their exchange.

Moving things inside a vacuum chamber from outside it can be an expensive exercise, particularly where that movement needs to be accurately repeatable to within about 0.1mm as in this case. Linear motion feedthroughs can be purchased with the requisite precision but funds were not available for such costly items, and even if they were, linear motion drives tend to be rather slow. Rotary motion feedthroughs although quick acting do not as a rule have the positioning accuracy of linear ones but one happened to be available for temporary loan. The feedthrough in question was, however, only graduated in five degree steps and so on its own would not allow precise detector positioning. With the addition of some positively locating device it was hoped that the detector positions could be firmly established, so that the CEM and the diode could be swopped quickly and accurately.

Figure 4.20:1 shows the calibration chamber as it was originally designed. The main vacuum body is a 150mm internal diameter T-piece with a 70mm flange set into its longest side. The rotary feedthrough lead into the vessel through the top flange and from it hung a carriage holding the two detectors, each pointing at right angles to the other. On the shaft of the carriage a two position stop located with a pin set into the top flange cover to fix the two detector positions, the effectiveness of this will be discussed later.

Both detectors required electrical supplies and provision was made for these by including two sets of electrical feedthroughs in the bottom flange cover. For the diode a 60V supply lead was necessary,

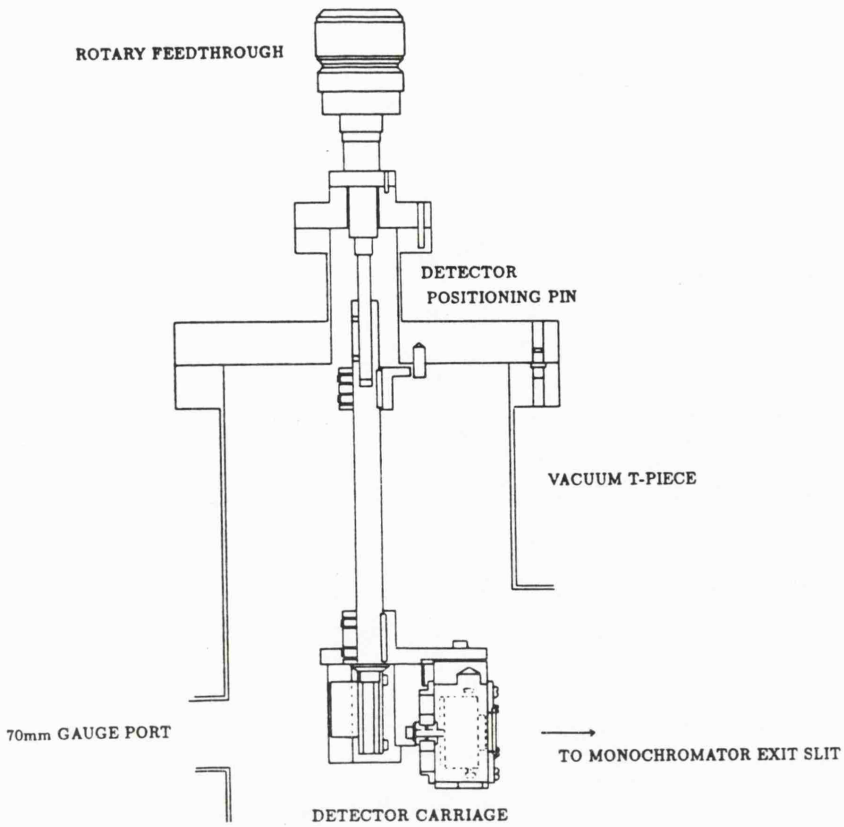

Figure 4.20:1 The CEM calibration chamber.

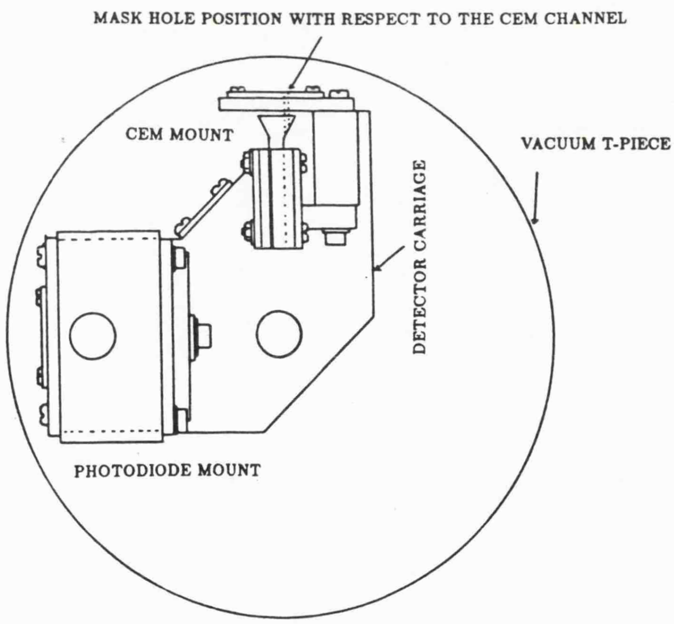

Figure 4.21:1 The calibration detector carriage.

plus a signal lead, and for the CEM a high voltage signal line and a signal earth were needed. Possible interference in the diode signal by the CEM pulses indicated that two well separated feedthroughs would be wise so that adequate screening could be installed if necessary.

Mullard B419 channeltrons are comparatively insensitive to operation in an indifferent vacuum environment, such as that exsisting in the monochromator when the PS was operating, however the spare 70mm flange on the T-piece allowed the addition of a Penning gauge head to monitior pressure. No separate pump was to be provided for the new chamber and so it was as well to know the pressure in the T-piece compared with that in the monochromator.

4.21 Detector Mounts for the Calibration Rig.

Figure 4.21:1 shows a more detailed diagram of the detector carriage with the two detector mounts. These were designed to accommodate the differing needs of the two detectors as regards support, and to allow aperture masks to be fixed in front of each.

Aperture masks were required to ensure that both detectors saw the same amount of the beam to avoid having to correct for the differing sensitive areas of the two devices. In addition, the variabilty of CEM efficiency with position has already been mentioned, but this was not a problem with the diode as its efficiency is insensitive to the position at which a given beam strikes it[4]. The CEM once calibrated could not be moved relative to its mask as this might change its apparent efficiency, the channeltron mount was therefore designed so that both detector and aperture could be removed from the calibration rig together and used elsewhere. This was not important for the diode as it was not intended that it be used again, except for recalibration.

Both detectors required a different mount, the CEM was sandwitched between layers of PTFE and clamped firmly while the diode was mounted in the manner recommended by the NBS.

High count rates required from the monochromator in order to stimulate a measurable current from the diode were expected to produce unacceptable gain loss in the CEM. To reduce the flux incident on the channeltron, a spring clip was fabricated to fix a piece of 1% transmission nickel mesh in front of the aperture mask. The aperture mask and its position with respect to the CEM channel is shown in figure 4.21:1.

4.22 Detector Electronics.

Electronics for the CEM followed very much that used for the B318 device (section 3.12), except that the B419 operates at higher voltage and so required a 3–4kV supply. All the electronics used for the channeltron was of the NIM variety, and in addition to the equipment used for the B318 a Single Channel

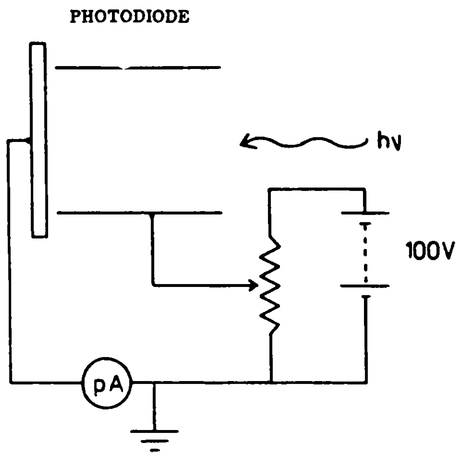

Figure 4.22:1 Schematic of the photodiode electronics.

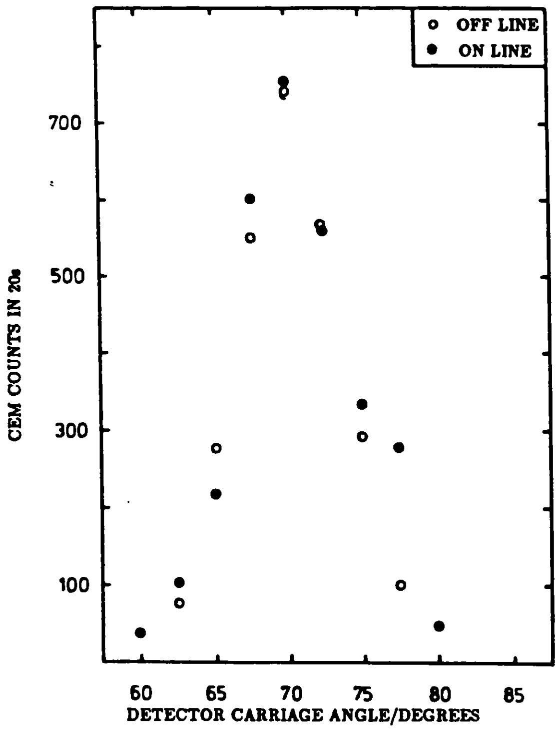

Figure 4.30:1 Calibration chamber 'beam' profiles on and off the 30.4nm helium line.

Analyser (SCA) and a counter were added to avoid the dead-time problems encountered when measuring high count rates with the MCA.

The NBS photodiode had very simple requirements as far as electronics is concerned: a low noise 60V power supply and an instrument capable of measuring down to 10^{-15} amperes. Sixty volts at very low noise were provided by connecting four 22.5V 'AVO' batteries in series and then adding an adjustable resistive divider to set the voltage. The circuit diagram is reproduced in figure 4.22:1. The femtoameter was also easily found since it was dicovered that there was a Keithley electrometer available in the group which would measure down to about 1×10^{-16}A on its most sensitive scale.

4.30 Evaluation of the CEM Rig.

Before any calibration work could be undertaken it was necessary to find out how well the calibration chamber would perform. First, a Penning gauge was connected to the vacant 70mm port on the T-piece to verify that the monochromator pressure was representative of the chamber pressure, it was found that this was indeed the case. The next objective was to establish that a good, clean spectrum could be recorded by a CEM mounted on the detector carriage.

When a channeltron was installed on the carriage and a helium discharge established in the PS it was found that no lines could be detected in the initial CEM position. This failure was at first put down to detector misalignment because an acceptable spectrum was recorded using the B318 CEM viewing the exit slit through the gauge port. Since it was difficult to improve on the alignment it was decide to dispense with the two position stop and try to locate the monochromator beam by scanning the detector through a range of angles close to the expected beam direction.

Scanning the detector produced the surprising result that there was an extremely broad range of angles over which there was a strong detected count rate, the strongest point in this signal did not however correspond with the monochromator beam because no line spectrum could be recorded. Two scans were then made, one with the monochromator on the 30.4nm helium line and one off line, these data are presented graphically in figure 4.30:1.

It is noticable that there is a slight excess in count rate at about 77.5 degrees when the monochromator is on line compared with off line. When the detector was positioned at 77.5 degrees a spectrum of helium could be recorded, albeit with rather poor signal to noise ratio.

It was realised that the significance of figure 4.30:1 and the poor spectrum was that there must be a great deal of scattered light from somewhere which was not visible to the B318 CEM. The origin of this light could be either through the exit slit, in which case there was little to be done, or from around

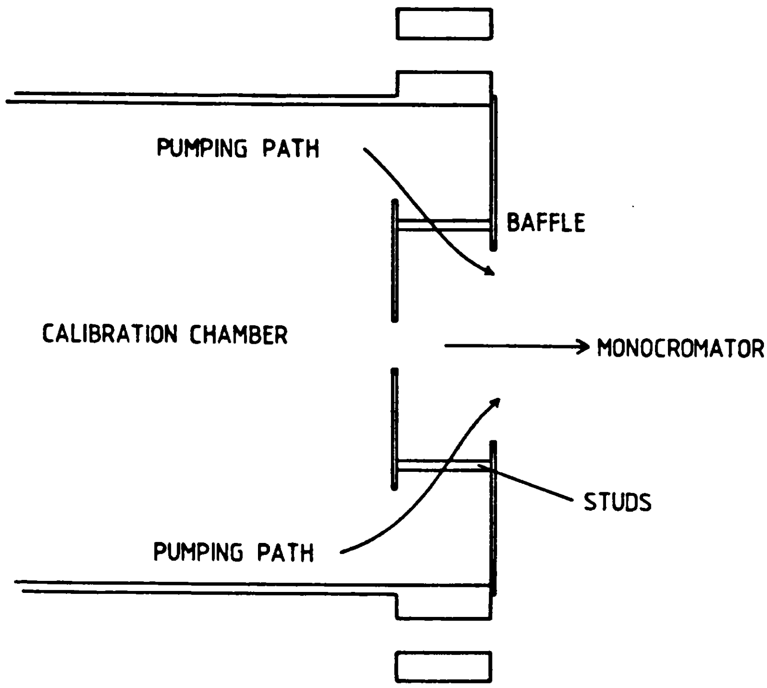

Figure 4.30:2 The baffle included between monochromator and test chamber to exclude stray light.

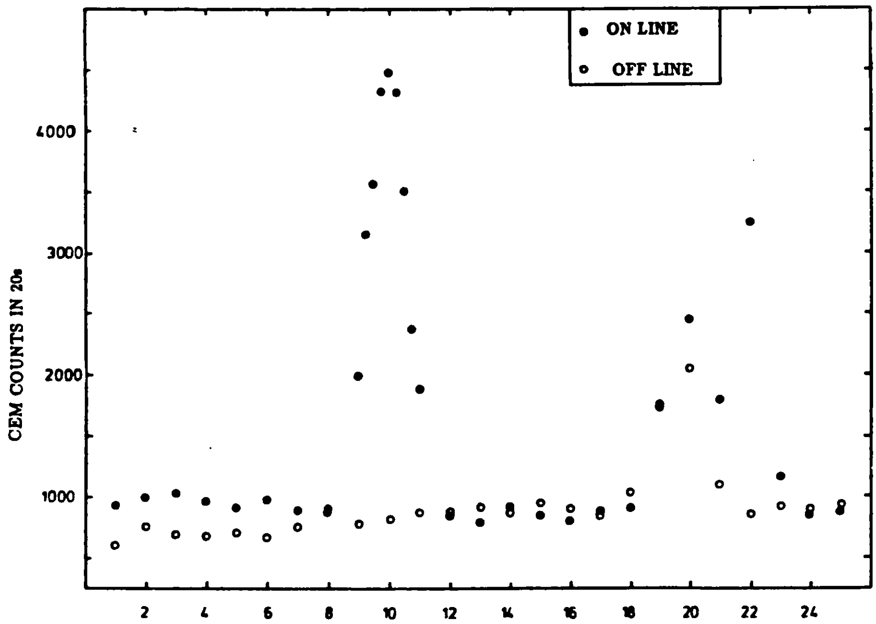

Figure 4.30:3 Calibration chamber beam profiles with baffle fitted; recorded on and off 30.4nm line.

the slit assembly. To exclude light from around the slits a baffle was made to the pattern of figure 4.30:2, and this was introduced at the flange between the monochromator and the CEM rig.

Scanning in angle with the baffle in place produced a much more sharply defined peak, so sharp in fact that it could only be found with difficulty using the coarse scale on the rotary feedthough. To improve the angular resolution the five degree scale was supplemented by a quadrant marked in degrees which was fixed to the feedthrough scale along with a suitable pointer. The new scale allowed the data presented in figure 4.30:3 to be recorded, and it can be seen that although there is still a background peak the monochromator beam is well separated from this.

It became apparent while the above tests were being performed that the two position stop intended to fix the positions of the detectors was not adequate. This was because the detectors couldn't be aligned with the monochromator beam with sufficient accuracy by removing the detector carriage from the vacuum vessel, it had to be done while the source was operating by locating the point of maximum count rate. If the detector positions had to be fixed in vacuo then the position stops had to be external to the vacuum system. Figure 4.30:4 is a photograph of the system adopted, it is based on the angle quadrant mentioned earlier and the stops are threaded so that they are adjustible. It was found to be possible to accurately locate the beam by holding the stop against its reference pillar and turning the stop until a maximum count rate was observed on the MCS.

Although it was easy enough to find the beam using the CEM, it was anticipated that the sensitivity of the electrometer might make things more difficult in trying to do the same with the photodiode.

4.31 Operating the NBS Photodiode.

Once it had been established that there was indeed a relatively background free monochromator beam in the mask position, it was time to install the diode and assess its ease of use. Since this meant unpacking the diode ordered from the NBS, which was kept in a desiccator, it was decided to use a diode which was on loan from the Laboratory for Space Research, Leiden. Because this diode was five years old it was the original intention to recalibrate it against the one ordered for this group and then return it to Leiden. No special precautions had been taken in storing the Leiden diode because it had been dispatched to Leicester in its original sealed holder but not otherwise protected, except for the addition of a small packet of silica gel. The storing of such diodes under ordinary laboratory conditions is known not to adversely effect their calibration for periods of a year or so[9], thus it was not expected that the calibration would have been greatly altered by the storage conditions.

When the diode had been installed on the detector carriage and the vessel evacuated, the PS was lit and the 30.4nm helium line again selected using the monochromator. By moving the source table

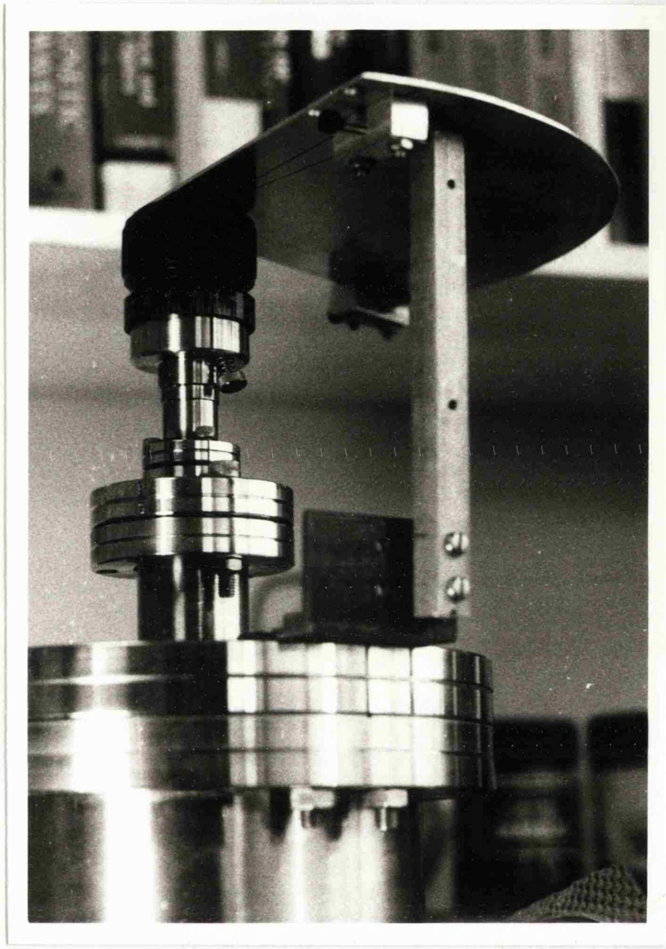

Figure 4.30:4 Photograph of the detector carriage stop mechanism.

so that the monochromator moved on and off the line, it was possible to see that there was a definite increase in current when on the line. Some experimenting with the electrometer scale and the detector position had, of course, been necessary before this was discovered.

It was not surprising to find that when the electrometer was on scales more sensitive than 10^{-12}A full scale, any movement of the detector carriage caused a large fluctuation in the registered current. This current was thought to result from changes in the capacitance of the connecting leads causing an induced current. Less easy to understand was the fact that when the electrometer was zeroed as recommended by the manufacturer, the instrument always registered a current of the order of 10^{-13}A when switched from the zeroing mode. This offset was ascribed to pick-up in the external leads, and it was found that it could be eliminated by adjusting the zero control while the electrometer was reading.

It was not possible to move the diode without causing a disturbance to the current reading but it was essential to plot a graph of current verses carriage angle in order to be sure that the diode was in the right place for calibration work. This was done by moving the rotary feedthrough by a small amount and measuring the distance between the threaded stop and the reference pillar, and then noting the current reading after it had stabilized. Figure 4.31:1 shows the curve of current vs. distance and from this the beam position is clearly established at 36 ± 1mm. Measurements indicated that the beam peak was reasonably flat topped, so small deviations from the ideal position would be insignificant.

4.40 Quantum Efficiency Calibration of a CEM against the Leiden Photodiode.

As the Leiden diode had been established in the vacuum chamber, it was decided to go ahead and calibrate a CEM with it. Using the Leiden detector first offered the advantage of minimising the amount of changing of detectors that had to be done, limited the exposure of the second diode to the vacuum system while development work was underway, and meant that when the true calibration was performed with the newer diode a QE curve could be derived from the second set of CEM QE's for the Leiden diode. As it happened, however, shortage of time meant that the only calibration results taken were with the Leiden diode.

Calibration measurements were performed by adopting the following sequence:

1) Using the CEM, the maximum count rate on the line concerned was found by tracking the monochromator whilst watching the MCS trace.
2) The CEM gain was reset to a predetermined value by adjusting the shaping amplifier gain.
3) The count rate over 20s was measured
4) The CEM was switched off and the turntable moved to the diode position; the current was allowed

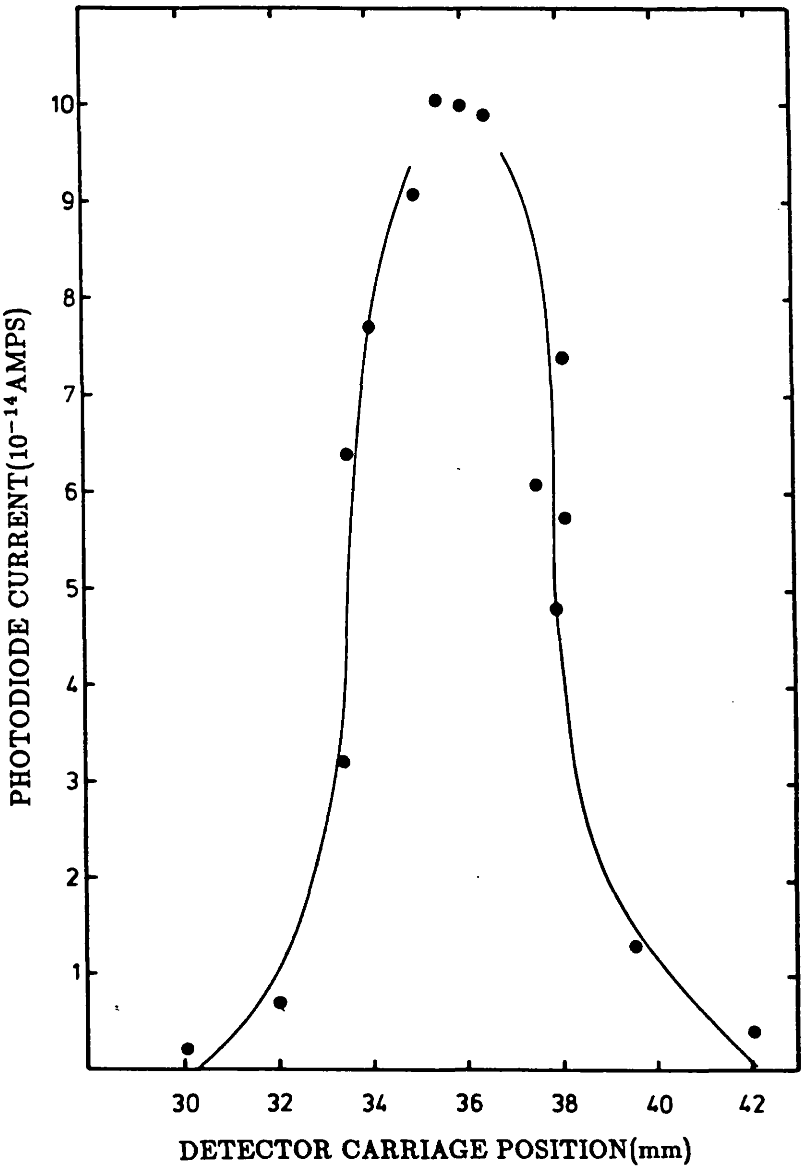

Figure 4.31:1 Current vs. distance beam profile recorded using the NBS photodiode.

to stablize and diode current noted.

5) The monochromator was scanned off line to a point well off the shoulder of the line.

6) The diode current was measured.

7) The electrometer was switched off and the diode swopped for the CEM.

8) The CEM gain was reset and the count rate over 20s recorded.

9) Repeat as often as possible.

This prescription was followed as far as time allowed for the following emission lines: HeI 58.4nm, HeII 30.4nm, HeII 25.6nm, and AlIV 16/16.2nm.

The first quantum efficiency measurements were at 30.4nm, two values of 21% and 24% were recorded which are somewhat higher than was expected as the results of Lapson and Timothy[7] indicated a value closer to 10%. These first measurements were conducted with a diode voltage of 55V rather than the recommended figure of 60V. Diode voltage has been reported as having little effect on cathode current[5] over the range 20–70V, but when the voltage was increased to 60.3V five subsequent values of 10.1%, 13.8%, 11.7%, 15.3%, and 12.3%, were measured. These results, and those for the other wavelengths are summarised in table 4.40:1, the recorded QE values are listed in the order in which they were taken.

Figure 4.40:1 shows the quantum efficiency of the Leiden diode as measured by the NBS and figure 4.40:2 shows graphically the quantum efficieny of the Mullard B419 CEM as measured at Leicester. The figures due to Lapson and Timothy are included for comparison.

4.50 Discussion of Results.

The striking feature of the data presented is the scatter in the measured quantum efficiencies, this is easily explained when it is considered that the PS would often show a drift in line emission of 10% or so over a period of a few minutes. This drift was particularly noticable when running the source with argon to obtain the 16nm aluminium doublet, especially when the source was still being run in. It was also found to be very difficult to stablize the source, even when running with helium, for the times required to make one QE measurement. Measurement time was largely the result of the wait necessary before the electrometer would become stable enough to record a diode current.

Another random contribution to the spread in results was undoubtably the drift in the zero of the electometer. It could often be half an hour or so before a reliable zero could be acheived, but after this time it was not unknown for the source to have drifted so far as to necessitate re-zeroing.

Compared with this error, other effects were probably rather less important. Several sources of

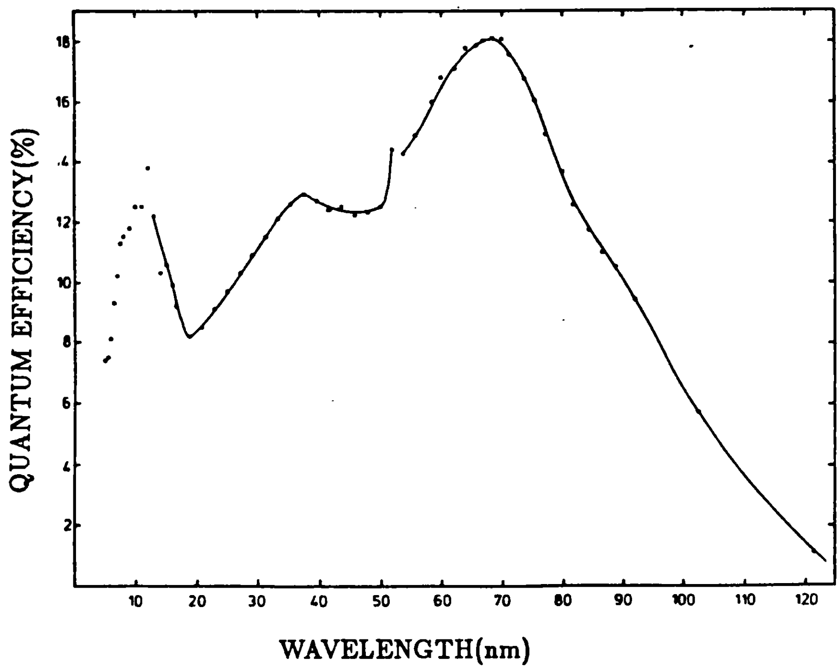

Figure 4.40:1 Quantum efficiency of the Leiden photodiode as measured by the NBS.

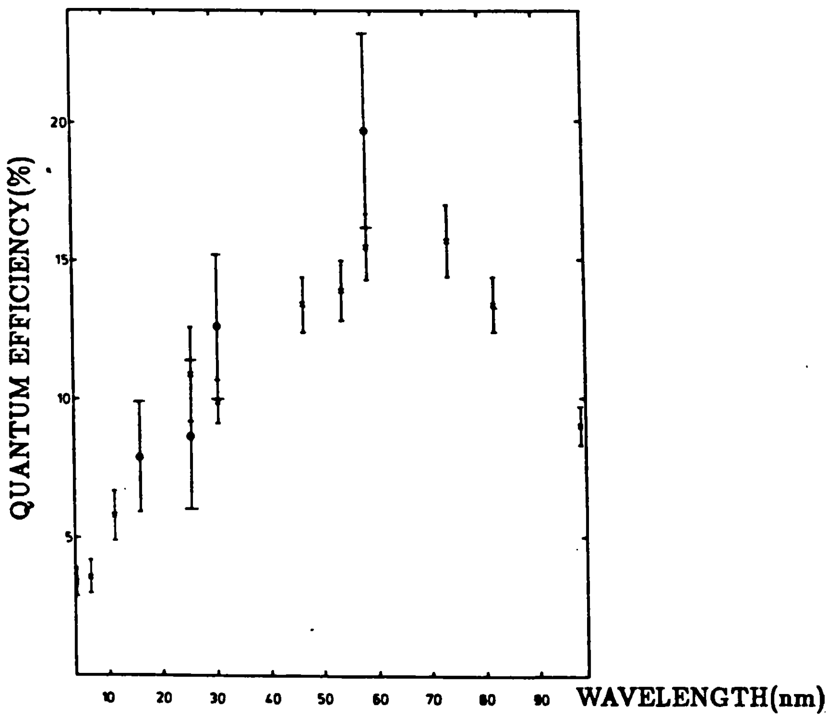

Figure 4.40:2 Measured Mullard B419 CEM quantum efficiencies (full circles) compared with measurements by Laspson and Timothy for a similar device.

error can be identified, firstly of course there is the initial calibration error for the diode with values ranging from 15% at short wavelengths to 8% above 50nm (see figure 4.40:1). Added to the uncertainty in the initial calibration there is the unknown drift in efficiency since, but it is unlikely from the published stabilities of these devices that this would have amounted to more than about 10%.

The transmission of the attenuation mesh is another possible error, though probably small. No actual measurement of mesh transmissions were performed at the time of the CEM calibration but the quoted value is based on the percentage open area of the holes. Open area may not be directly interpretable as an XUV transmission if a significant amount of scattering of light into, or out of, the beam occurs. Had scattering been a problem it would have manifested itself as a degradation in the line to background ratio in specta, and this certainly wasn't the case at least for the brighter (30.4 and 58.4nm) lines. It is believed in addition to the latter that mesh transmissions were measured at Leiden[10], from where the mesh used originated, and that no great deviation from the quoted value was observed (see section 5.51).

It was mentioned earlier that the measured values of the CEM quantum efficiency at 30.4nm was consistent with that measured by others under similar conditions. This agreement was also apparent at 58.4nm and at 25.6nm (although at 25.6nm too few results were taken to be over confident about the QE here), but at 16nm there seems to be an over estimate by a factor of about two.

Although the mean value at 16nm was found to be rather high, the spread in the data is also large because the line to background ratio at this wavelength was poor, typically about 50%. A consequence of this poor signal to noise ratio was that photocurrents were extremely difficult to measure.

The reason for the poor signal to noise ratio at 16nm seems to be the scattered light problem partially solved by the introduction of a baffle. It had been noticed before that cleaner spectra were recorded if the detector could be moved as far as possible from the exit slit, and it was not surprising that with the distance dictated by the need for a high flux a large background was observed. With the inclusion of further baffling, perhaps including a collimator it should be possible to improve the situation greatly. Spectra subsequently recorded in the mirror and detector test facilities (chapters 6 and 5 respectively) show markedly better signal to noise ratios as a result of superior stray light elimination.

Looking at table 4.40:1 it appears that there is a general upwards trend in the measurements. These data were recorded over a period of three days, the first four values were taken on the first, the next seven on the second, and the last two on the third. It could be that on each day the source was misbehaving more, but it is also possible that the increase is due to a drop with time in the diode efficiency. E. B. Salomans measurements[9] demonstrated the poisoning effect of oil contamination on

TABLE 4.40:1

Measured CEM Quantum Efficiencies

Wavelength	AlIV 16nm	HeII 25.6nm	HeII 30.4nm	HeI 58.4nm
	7.4%	9.2%	10.1%	19.5%
	8.5%	8.1%	13.8%	21.7%
	9.0%		11.7%	16.4%
	18.0%		15.3%	21.9%
	20.0%		12.3%	19.2%
	12.7%			
	16.0%			
	16.4%			
	22.0%			
	19.5%			
	17.5%			
	23.9%			
	24.4%			
mean±error	(8.3±2.0%)*	8.7±2.7%	12.6±2.6%	19.7±3.5%

*See section 4.50

photodiode photocathodes, and it may be significant that before the 16nm measurements were made the diode had only been exposed to the cold trapped monochromator vacuum. When it came to trying to excite the AlIV lines, however, it became necessary to use the un-trapped Penning source diffusion pump (which is rather old) in order to reduce the pressure sufficiently. The conductance between the source and the monochromator was small, but it is possible that backstreaming occured to damage the photocathode.

Attempts to assess possible hydrocarbon contamination using a mass spectrometer head were frustrated by the presence in the monochromator vacuum system of a leak. The leak made the dominant mass peaks detected correspond with oxygen and nitrogen and it was found to be impossible to increase the sensitivity sufficiently to trace any possible oil cracking products. It was not possible to rectify the leak within the time scale of the experiment, and so the extent of any contamination remains an open question.

It should also be noted that in the only reported measurements under comparable conditions[7], the data only cover 25.6nm and 11.3nm with no value between. It is probable that the true number is of the order of 10% so the bracketed value in table 4.40:1 has been adopted, it is the mean of the first three results recorded. This extends to 16nm the generally good agreement between the Leicester results, at other wavelengths, and the figures provided by Lapson and Timothy[7]. Without this apparently arbitrary adjustment it was found to be impossible to measure realistic MCP quantum efficiencies as is reported in chapter 5.

The choice of the first three measurements of CEM QE can be justified, as has been mentioned, by the suspicion of hydrocarbon contamination inside the monochromator and the reported sensitivity of windowless photodiodes to this effect, especially at wavelengths below 20nm[9].

CHAPTER 5

Calibration of a WFC Detector.

5.10 Equipment.

The ultimate objective of the experimental work described in previous chapters was the measurement of the quantum efficiency of WFC style detectors and the reflectivity of WFC mirrors as a function of wavelength. With the completion of the monochromator development, and the production of a transfer standard detector, it became possible to shine a known flux of XUV light onto a detector and determine its efficiency. The commissioning of the Detector Test Facility (DTF) made this a relatively simple exercise.

The DTF beam line is shown schematically in figure 5.10:1, the monochromator is included but a conventional X-ray source could be substituted for the production of shorter wavelength light. Between the monochromator and the DTF proper, there is an interface tube which mates with the source gate valve on the DTF; this gate valve can isolate the facility from its source. After the valve there comes the main vacuum tank designed to house items such as filters, collimators, and monitor counters, the latter being movable by means of a motion feedthrough mounted in the tanks' lid. Another gate valve separates the tank from the MCP detector mount and motion system.

Movement of the detector was accomplished by two bellows; one to allow vertical and horizontal motion, and the other to allow variation of the angle of incidence. All movements were by gear mechanisms which will eventually be automated, replacing the handwheels currently employed. The detector is mounted from the second bellows; a 'Viton' O-ring sealing straight onto the vacuum body of the detector.

For the purpose of measuring the MCP quantum efficiency, the calibrated CEM was placed in the beam suspended from the motion feedthrough. The CEM and its calibration mount are illustrated in figure 5.10:2 showing the 'wobble stick' nature of the feedthrough which allowed quick, but precise, movement into and out of the beam.

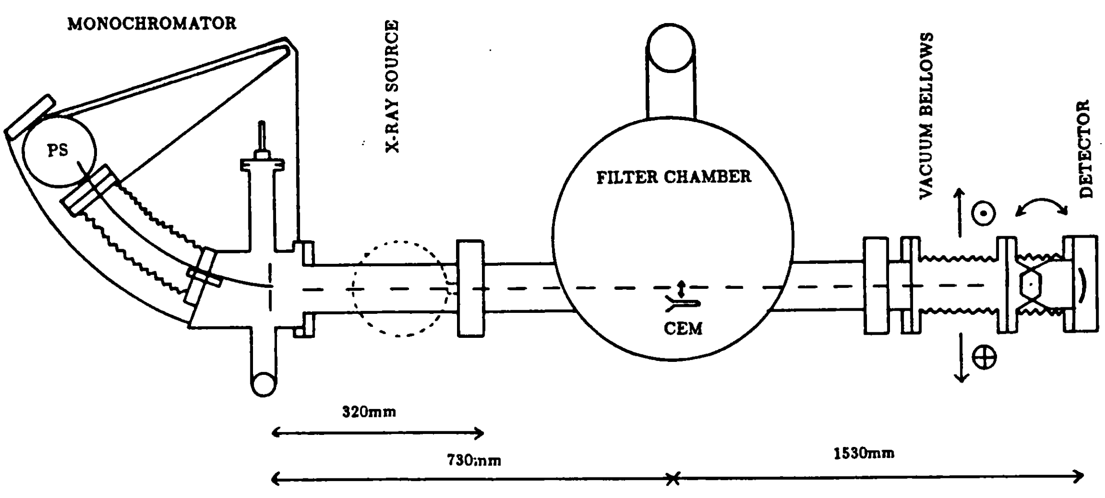

Figure 5.10:1 Schematic diagram of the DTF beam line.

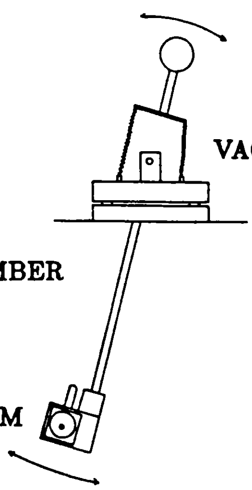

Figure 5.10:2 The calibrated CEM mounted on the DTF 'wobble stick' feedthough to allow rapid movement into and out of the beam.

5.20 The MCP Detector.

The detector to be calibrated was a development model of the type of detector to be flown on the WFC experiment. This type is novel in that it incorporates a CsI photocathode and is curved to match the optimum focal surface of the WFC mirrors[1]. Some important features are illustrated in figure 5.20:1, which was reproduced from reference 5, they are:

1) The repeller grid. This is a high transparency mesh held at a negative potential with respect to the photocathode to deflect photoelectrons into the microchannel electron multipliers.
2) A CsI coated microchannel plate with spherical surfaces ground to a radius of curvature of 167mm, and with its channel axes parallel with the detector axis.
3) A second channel plate, this time with its channels at 13 degrees to the detector axis, but also curved to match the front plate.
4) The readout device, a curved resistive anode with four corner contacts for charge sensing.

Of the above, the CsI coated front plate comprises the XUV sensitive element in the detector, both photocathode and MCP glass contributing photoelectrons depending on photon energy[2]. Figure 5.20:2 shows the form of the photocathode as deposited on the front surface of the first channel plate of the pair. Without a repeller grid, electrons released from the CsI on the interchannel area of the front surface, stand little chance of entering a channel and initiating an avalanche. For this reason the CsI that lines the top portion of each channel is most effective in sensitising the detector to XUV light.

The extent of penetration of the photocathode into the channels is determined by the coating geometry. Figure 5.20:3 shows how depth of penetration is greater where the coating source is close to the channel axes.

The physics of MCP photocathodes has been extensively discussed by Fraser[2,9] who has pointed out the principle interactions involved within a photocathode and MCP for a photon to be detected.

The first interaction in the detection process is between the photon and the sensitive surface, here there is an angle of incidence dependent probability of the photon being reflected rather than passing into the material. Given optical constants of sufficient precision, it is a simple matter to calculate this probability using the Fresnel equations[11]. Figure 5.20:4 shows an XUV photon incident on a surface at angle of incidence A, and the reflected and refracted paths. The refracted beam propogates at a grazing angle A' which is less than A since the refractive index is less than unity for XUV wavelengths.

Inside the absorbing medium, the refracted beam declines in intensity exponentially according to the relation:

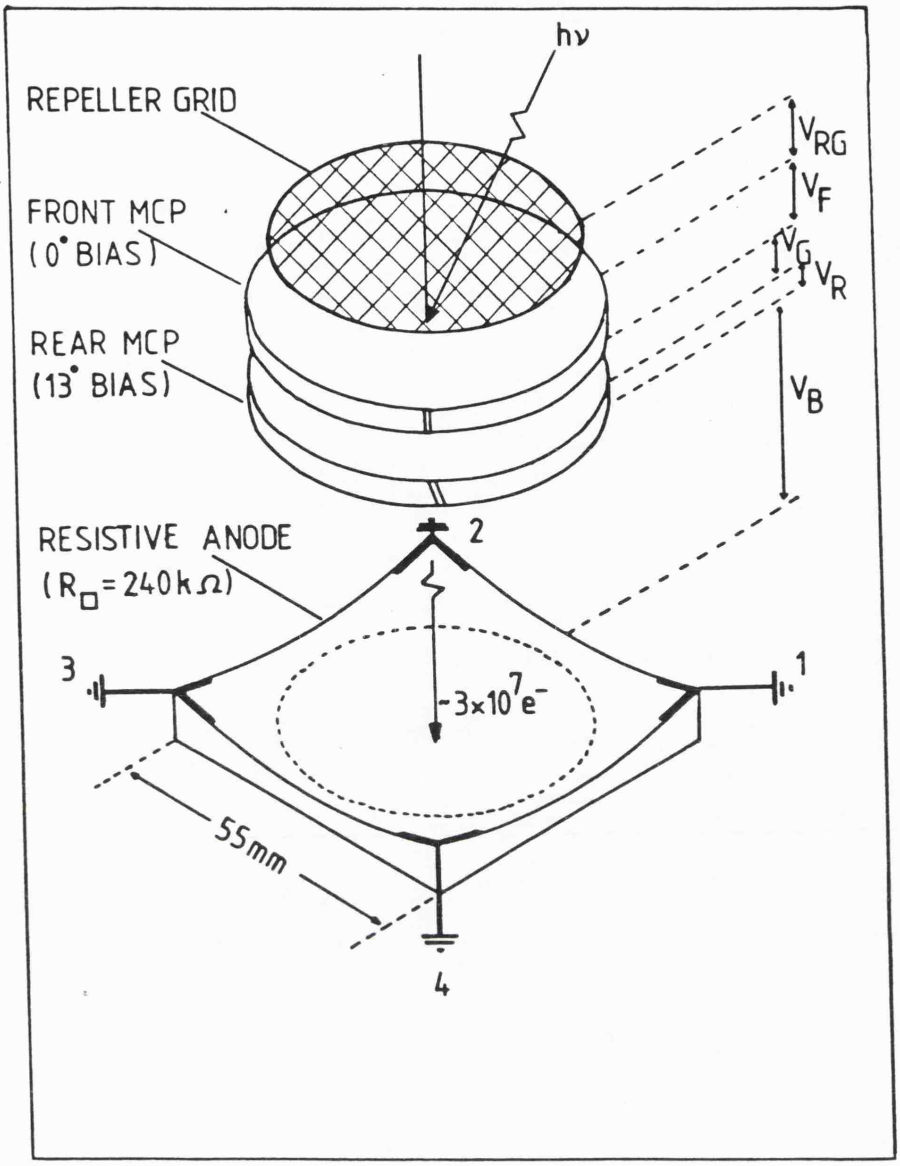

Figure 5.20:1 The WFC MCP detector. From reference 5.

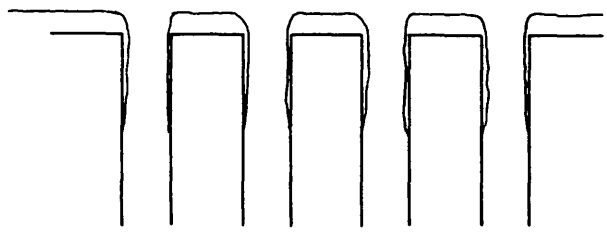

Figure 5.20:2 CsI deposited onto the front surface of a MCP; the CsI penetrates into the channels.

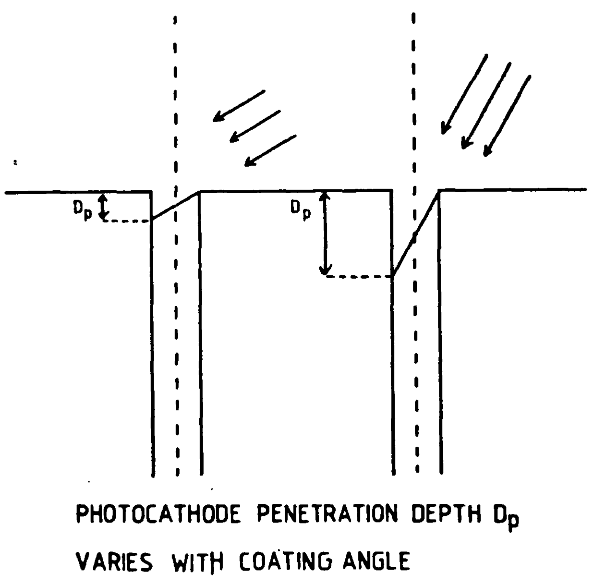

Figure 5.20:3 The extent of the penetration of CsI into the MCP channels depends on the coating angle with respect to the channel axis.

$$I = I_0 e^{-\mu d} \qquad 5.20:1$$

where μ is the linear absorption coefficient and d is the distance travelled in the medium. The probability that absorption results in the emission of a photoelectron from an atom then depends on the cross section for the interaction of the photon with any particular orbital. Clearly if the energy of the photon is less than the binding energy of the electron in a particular orbital that electron will not be ejected.

Atomic relaxation following the emission of photoelectrons may result in the production of Auger or Coster-Kronig electrons, and these may contribute to the stimulation of electron avalanches in the MCP if they have sufficient range in the MCP or photocathode material to reach a channel.

In his model Dr. Fraser assumes that all electrons which enter MCP channels initiate avalanches and are thus detected. He has been able to predict with some success[2] the behaviour of a given photocathode material deposited with a given geometry onto a MCP. The various interaction probabilities, for example reflection probability and photoelectron yield, are calculated by using published cross-section or photocathode quantum yield data.

Sensitisation of the front MCP in a detector thus increases the chance of an electron pulse of high gain being produced. A second MCP in series with the first increases gain with reduced risk of ion feedback associated with operating single MCPs at high gain[4].

Feedback protection by a second MCP, with channels biased with respect to the first, works by limiting the drift range of ions from the output end of the channel so limiting the possibility of them gaining enough energy to initiate an avalanche at the input end of the front plate. An alternative approach has been to curve CEM and MCP channels[3].

Figure 5.20:1 shows the voltages across the channel plates, across the gaps, and between the front plate and the repeller grid. These voltages were provided by high voltage power supplies and were therefore adjustable, the values chosen having considerable influence on the detector performance. In addition to power supplies, electronics was necessary for the signal read-out from the device and figure 5.20:5 shows a schematic diagram of that used for pulse counting and imaging.

The read-out electronics was broadly divided between the analogue amplification and pulse counting system and the digital imaging electronics. The former consisted firstly of four pre-amplifiers sensing the charge reaching the four corner conductors on the resistive anode, the output from these was passed to the pulse counting electronics and via four filter amplifiers to the imaging electronics. Image analysis was performed by a BBC microcomputer; it determined the position of charge pulses on the resistive

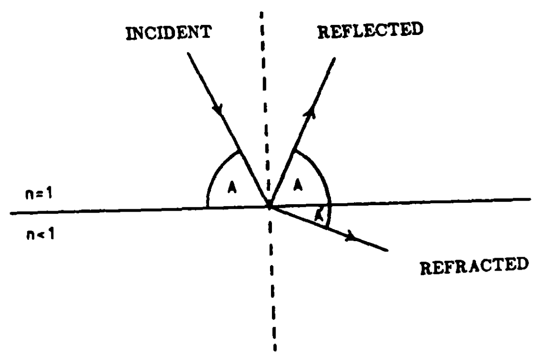

Figure 5.20:4 Reflection and refraction of XUV light at the photocathode surface.

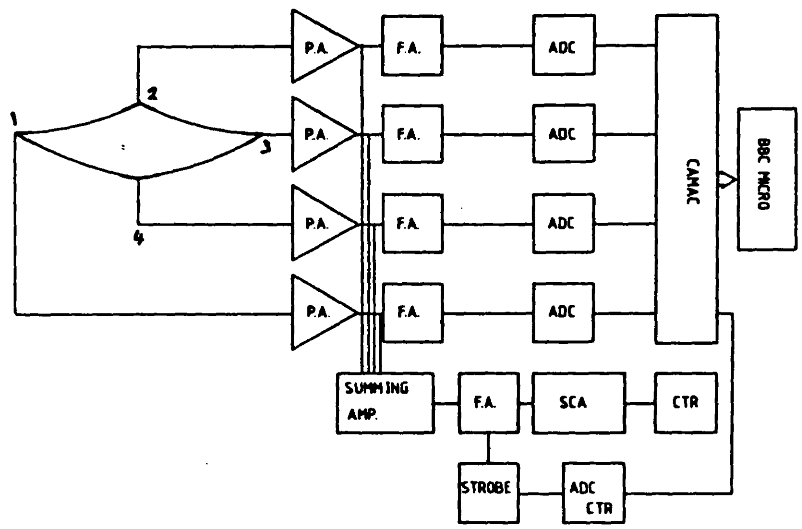

Figure 5.20:5 Schematic of the MCP pulse counting and imaging electronics.

anode by comparing the voltage at each corner contact as sensed by Analogue to Digital Converters (ADCs). The centroid of a charge cloud incident on the anode is given by[5]:

$$X = V1/(V1 + V3), \text{and} Y = V2/(V2 + V4)$$

where Vn is the voltage induced at each anode contact. The microcomputer then produced a pictorial representation of the accumulated counts as they were registered by the electronics.

5.21 Detector Operation.

It has already been stated that detector variables like the plate voltages can profoundly effect performance. Development work on the WFC detectors at Leicester has lead to the establishment of optimum operating parameters for this detector, these ensure that the device operates in a saturated mode. Saturation simply means that the detector produces a peaked pulse height distribution (PHD) which ensures that the counting electronics is able to count all the events detected. It is also important that the dynamic range of the electronics be high enough that the PHD of the detector be accommodated under all operating conditions.

The values used for calibration work were: Vrg=100V or 0V, Vf=1550V, Vg=100V, Vr=1450V, Vb=300V. The symbols used refer to figure 5.20:1.

5.30 XUV Alignment of the DTF.

Detector quantum efficiency measurements were the first work to be undertaken in the newly commissioned DTF, and as such some alignment was necessary before they could proceed. The facility was complete except for the absence of any collimators or beam stops, and so it was necessary to introduce a restricted aperture between the monochromator and the source gate valve. Initially a 5mm diameter aperture was installed but it was planned to restrict this further if required, to reduce the beam flux.

All initial tests were performed with a low current, low pressure discharge in helium with the monochromator set to 30.4nm. Even with a current of the order of 10mA in the PS it was found that the detector count rate was $5000s^{-1}$ over an area about 19mm in diameter. This spot size was somewhat smaller than the 24mm indicated by a projection of the 5mm aperture onto the detector surface, and showed that the monochromator divergence was 0.25 degrees. The observed MCP count rate was rather higher than was acceptable, and a reduction in source current to reduce the count rate only lead to unstable source operation. A mechanical restriction on flux was thus called for.

Instead of further restricting the aperture, it was decided to reduce the beam strength by introducing a mesh with approximately 1% transmission across the existing hole. This not only reduced the count rate as expected, allowing increased source currents to be used, but it also caused a vertical stripe pattern on the detector image. Figure 5.30:1 shows this effect which will be discused further in a later section.

Figure 5.30:2 shows the profile of the monochromator beam in two detector axes. This was produced using the microcomputer by displaying the total accumulated count against X, and Y co-ordinate. The form of the profile is of a relatively flat-topped distribution in both directions with the broad top making up perhaps half of the full width of the peak. Translating this measurement to the CEM position in the main vacuum tank meant that in order to attain a good correlation between CEM count rate and the peak count rate in the detector image, the CEM would need to be positioned to within ±2mm in each direction perpendicular to the beam.

This requirement was most easily satisfied in the X-axis (the X-axis of the detector lay in the horizontal plane), because in this direction the beam position is movable by scanning the monochromator in wavelength. A movement in the beam position, as measured on the MCP, of about 8.5mm occured as the monochromator was traversed from one side of the 30.4nm line to the other. This motion enabled the CEM to be centred precisely in the X-direction simply by tuning the monochromator carefully to maximum count rate as registered by the CEM.

In the Y-direction there was no such movement, or at least not enough to significantly alter the beam position with respect to the CEM, so the alignment in the Y-direction had to rely on the initial CEM positioning on its mount. It was found that the CEM position could be easily established to within a millimeter of the centre of the expected beam position, and this expected beam path was verified by the position of the beam spot on the MCP detector.

With the CEM sampling the peak of the beam profile, it was hoped that calibration between the two detectors could be performed by comparing the CEM count rate with that from an area on the MCP image corresponding with that part of the beam viewed by the CEM. Unfortunately it was found that when the computer was asked for the count rate within a box marked on the screen, inconsistent values were returned when the total detector count rate was high. This was attributed to time delays caused by the centroiding required to produce an image and the additional processing involved in sampling the image, the result was an inability on the part of the imaging system to cope with high count rates.

When the beam flux was changed by altering the PS conditions and moving to the fainter 25.6nm line, it was observed that as the count rate was reduced the proportion of events placed inside the box approached a limit of 0.064. To explain this a model of the beam profile was adopted (figure 5.30:3) and the proportion of events observable by the CEM was estimated as 0.069. Subsequently the measured value of 0.064 was used to determine the MCP count rate in the CEM area directly from the total

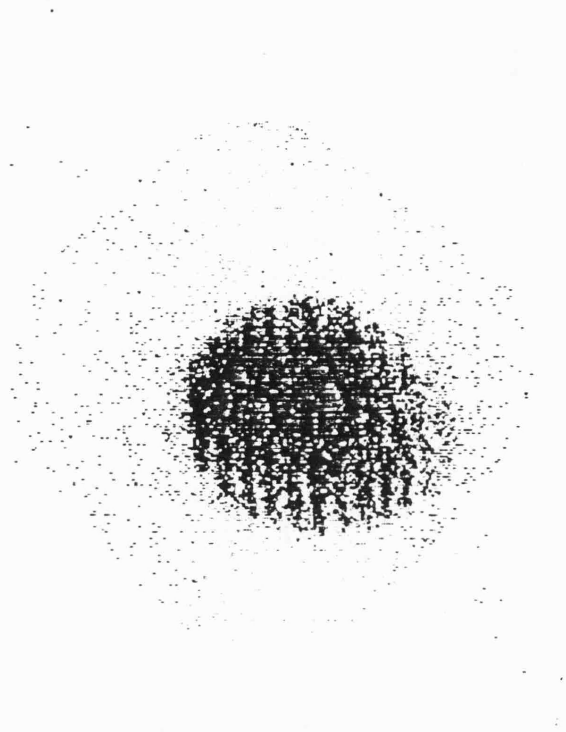

Figure 5.30:1 MCP image of the DTF beam showing banding introduced by attenuation mesh.

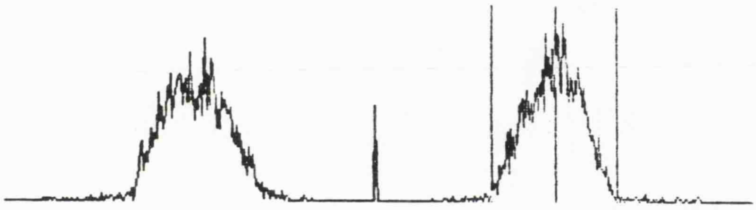

Figure 5.30:2 The profile of the monochromator beam in two axes.

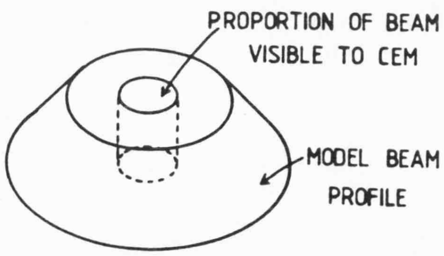

Figure 5.30:3 Beam profile used in the calculation of the proportion of the beam observable by the CEM.

(background subtracted) MCP count.

5.40 XUV Calibration of the MCP Detector.

Having established the position of the CEM in the beam, and the technique for reducing the imaging detector count rate to that seen by the CEM mask, the calibration was a simple matter of comparing count rates. Measurements were made at an angle of incidence of 30 degrees with respect to the detector axis at the wavelengths: 16nm, 25.6nm, 30.4nm, 46nm, and 58.4nm. Thirty degrees is approximately the WFC illumination angle and as MCP quantum efficiency varies markedly with angle[2], this was the obvious angle to make the first measurements. The wavelengths listed above are those for which the CEM quantum efficiency has been measured (see chapter 4), with the exception of 46nm.

This latter wavelength nicely fills a gap between 30.4nm and 58.4nm so it was decided to derive an estimated CEM QE at this wavelength using the other values and the data of Lapson and Timothy[6]. The resulting figure for Qc(46nm) was (14.5+3)% arrived at by scaling an estimated value from reference 6 by a factor reflecting the systematic difference between the measurements of chapter 4 and those of Lapson and Timothy. The quoted error takes account of the errors typical of the measured values and of the difficulty of extracting accurate figures from published graphs.

During these measurements it was found that although sensible QEs were measured at 25.6nm, 30.4nm, and 58.4nm, at 16nm the values based on Qc(16nm) from chapter 4 were greater than 100%. It was observed in chapter 4 that the 16nm data were the most difficult to obtain and that later values were not consistent with the earlier ones. In the light of this it was decided to take (8.3+2)%,this being the mean of the three lowest values (table 4.40:1), as the true Qc(160).

The justification for picking three values from the 16nm calibration results is twofold: Firstly, the three numbers chosen are based on the most reliable diode photocurrent measurements, and secondly they are consistent with the values at 25.6nm and 11.4nm published by Lapson and Timothy, and others[7].

Quantum efficiencies were measured at 30 degrees at the wavelengths above, and at 30.4nm over a range of angles of incidence from -1.5 to 47 degrees. All measurements were for repeller grid voltages (Vrg) of 100V and 0V.

During the measurement work it had been observed that at long wavelengths, ie. 58.4nm and 30.4nm, the detector image included verticle stripes (figure 5.30:1). It was noticable, however, that this effect had disappeard altogether at 16nm and was hardly visible at 25.6nm. This wavelengh dependence suggests the effect is a result of diffraction, possibly at the reducing mesh although the symmetry of this item would indicate banding in both detector axes and this was not seen.

The image structure had little effect on the quantum efficiency measurements, as the pitch of the pattern (2.5mm) was small enough that at least one complete peak and valley were in the CEM field at all times. Using the the grating equation for normal incidence and first order:

$$L = d \sin(B)$$

a pattern pitch of 2.5mm at 2m implies B is approximately 0.036 degrees hence;

$d = L/sin(0.036) = 50\mu m$ at 30nm. This means that features with widths of the order of 50μm are required to explain the image banding.

Nickel meshes used as attenuators were composed of small holes arranged in a hexagonal pattern and measurements indicated a pattern pitch of approximately 350μm with a pore size around 50μm. The origin of the image banding may thus be explained by diffraction through the mesh with the band period determined by the mesh pore size. The absence of this effect for shorter wavelength lines may be a consequence of poorer line to background ratio for these lines.

5.41 Quantum Efficiency Results.

Quantum efficiencies measured by the above technique are plotted in figure 5.41:1. These are the five points to the right, those on the left were measured using a soft X-ray source producing lines at 4.4nm (C_k), 6.7nm (B_k),and 11.4nm (Be_k). The soft X-ray results were produced by Dr. M. Barstow and are included here for completness. Two sets of points are plotted; the full circles are QEs measured with a repeller field applied by means of the repeller grid, and the open circles show QEs with no field applied. Both sets of points are corrected for the transmission of the repeller grid mesh which was 92%.

Figure 5.41:2 shows the result of measuring the quantum efficiency of the detector at 30.4nm over a variety of angles of incidence. The angles considered range from -1.5 to 47 degrees, the significance of the negative angle being only a zero offset in the angle scale on the detector motion system. Again the two sets of points are for 100V and 0V on the repeller grid.

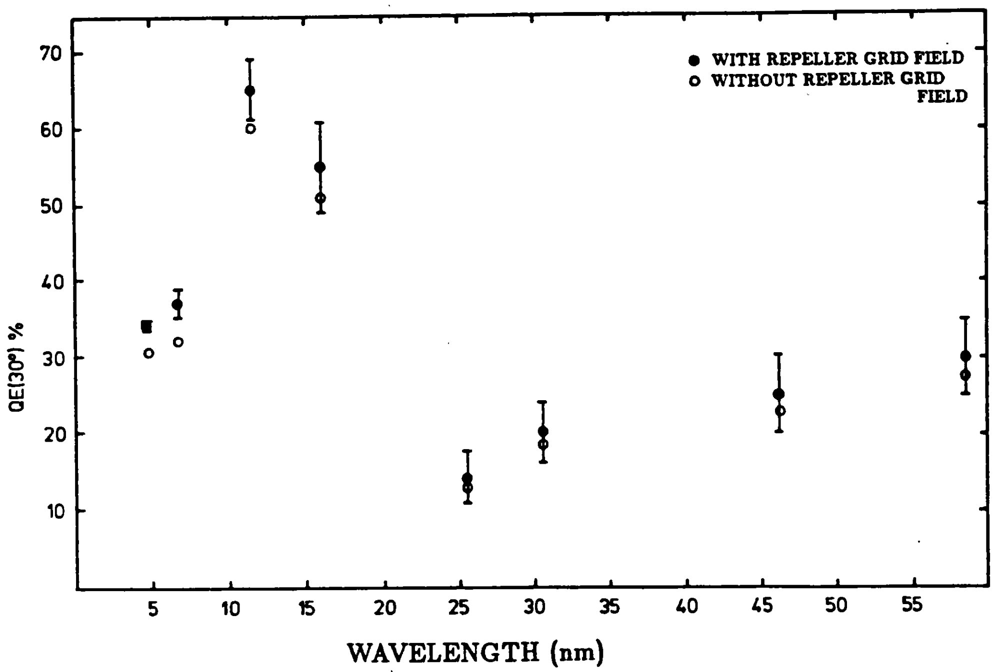

Figure 5.41:1 Measured MCP quantum efficiencies. The three soft X-ray points on the left were measured by M. A. Barstow.

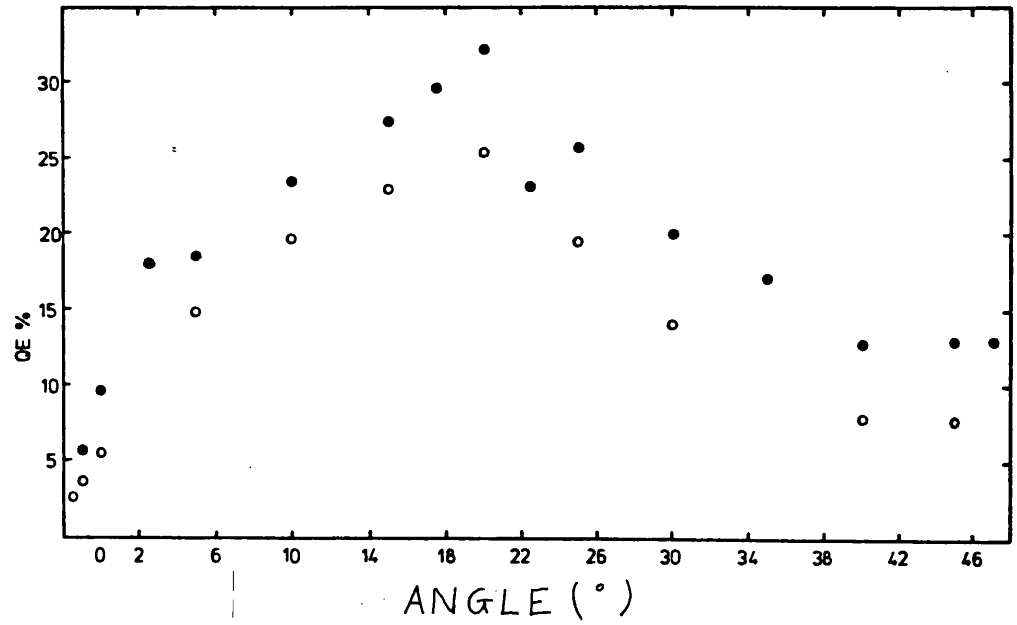

Figure 5.41:2 The variation of measured 30.4nm quantum efficiency with angle of illumination.

5.50 Discussion of QE Results.

The errors indicated in figures 5.41:1 and 5.41:2 stem in part from the spread in the measurements, but are dominated by the uncertainties in the CEM calibration. This is particularly true at 16nm, where CEM calibration was especially difficult. Other systematic effects, like the error involved in estimating the proportion of events recorded by the MCP detector which were visible to the CEM are small by comparison. Similary insignificant are random effects like the repositioning accuracy of the monitor counter.

Large errors apart, the quality of the measurements can only be assessed against comparable data from other sources or by looking at the physics of MCP photocathodes. Alas, quantum efficiency measurements in this waveband are scarce for CsI coated MCP detectors, indeed the work presented in this chapter represents the first such measurements on this novel detector configuration, and the first to bridge what was hitherto a gap in the data between 11.4nm and 25.6nm.

Some encouragement may be drawn from measurements made at Leiden, as yet unpublished, which show a similar increase in efficiency from 25.6nm to 58.4nm although the absolute level of efficiency differs because of dissimilar photocathode deposition geometry. This detector, intended as the readout element for a Gas Scintillation Proportional Counter (GSPC), was coated with 1400nm of CsI, at Leicester, with a coating source angle of 6 degrees with respect to the channel axes. A WFC detector similarly has 1400nm on its front surface but is coated at 11 degrees implying a thicker coating inside the MCP channels, but one which doesn't penetrate as far down the channels. Data from Berkley in California[8] shows an almost identical efficiency at 30.4nm, though at different photocathode thickness and angle of illumination (8 degrees).

According to Fraser (section 5.20), the overall shape of figure 5.41:1 can be explained by the photoabsorption cross section of CsI. The observed peak around 12nm in figure 5.41:1 corresponds well with the peak in published absorption spectra for CsI [10]. Figure 5.50:1, taken from reference 2, shows the predicted form of the QE variation with wavelength for a CsI coated MCP. Parameters indicated in the figure are: The length to diameter ratio of the MCP channels, the MCP bias potential, the channel diameter, and the photocathode thickness on the channel walls. Figure 5.50:1 gives the expected QE from a photocathode configuration representative of the WFC situation but not identical to it. The theoretical curve should be compared with the open circles of figure 5.41:1 as figure 5.50:1 shows the QE contribution from the channel photocathode only and does not include the contribution that may be expected from the front surface of the MCP when a repeller grid potential is applied.

The two angles of incidence depicted in figure 5.50:1 show that only small variations in the form

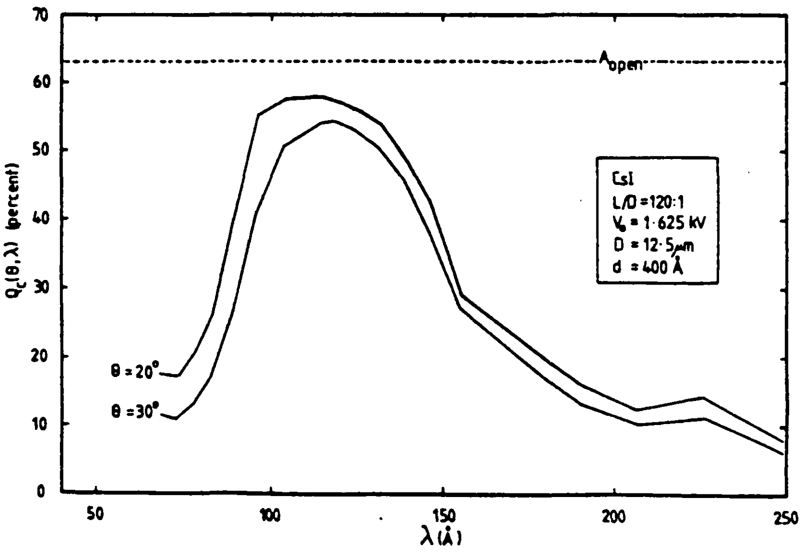

Figure 5.50:1 The quantum efficiency of a CsI coated MCP detector predicted by Fraser (reference 2).

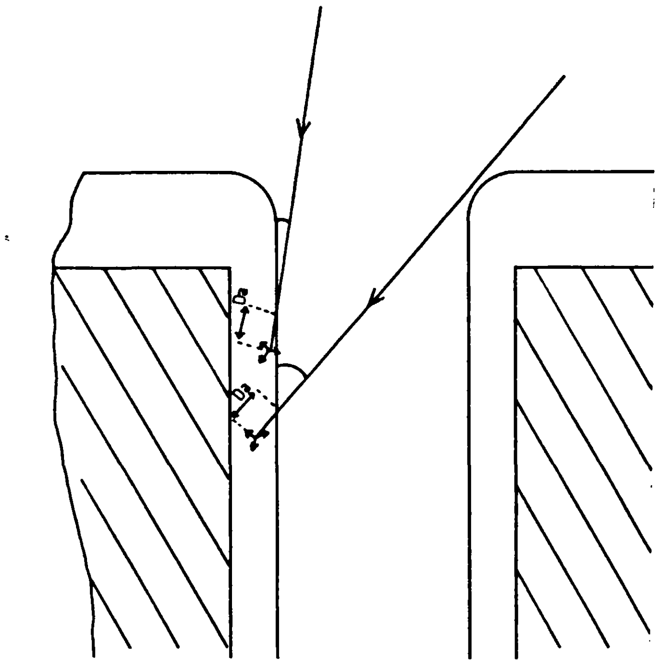

Figure 5.50:2 The absorption of photons at differing depths in the channel entrance photocathode with changing angle of illumination; Da is the absorption depth for photons in the photocathode.

of the curve are expected, though a significant change in absolute QE may be observed. The change of QE with angle of incidence is apparent from figure 5.41:2 (open circles).

Variations of QE with angle of incidence occur as a consequence of the photocathode geometry. Figure 5.50:2 shows the absorption of photons with differing angles of incidence by the photocathode at the top of a MCP channel. With photons incident at large angles with respect to the channel axis, the probability of reflection is low but the depth of absorption is large. Electrons liberated deep within the photocathode are less likely to escape to stimulate a channel avalanche than those created near the surface.

As the angle of incidence decreases with respect to the channel axis, the probability that the photon will be reflected increases but photons absorbed by the medium will be absorbed close to the photocathode surface so that electrons liberated have a high probability of reaching the surface and being detected. Thus as the direction of incident light approaches the MCP normal, an increase in quantum efficiency resulting from shallow electron creation should be observed. If the direction of incidence is allowed to approach the channel axes further, however, the quantum efficiency may be expected to decline as the reflection probability increases.

Figure 5.41:2 bears out this qualitative view of photocathode behaviour. Quantitative predictions of the absolute quantum efficiency are very much dependent on the thickness of the photocathode where it penetrates into the channel, the extent to which it does so, and the details of electron transport within the material.

Fraser has addressed these points and figure 5.50:1 represents a quantitative prediction of the QE of a CsI coated MCP. The differences in the observed QEs from those of figure 5.50:1 are thought to be largely a result of the differences between the situation modelled and the real photocathode configuration. The model photocathode assumed a front surface thickness of 600nm with a deposition angle of 15 degrees, this compares with actual figures of 1400nm and 11 degrees. The WFC photocathode would thus have a thicker coating inside the channels pentrating further down its length. Higher measured QEs than those predicted by figure 5.50:1 would on this basis be understandable though the extent of the disagreement is somewhat large.

5.51 CEM Mesh Transmission.

In chapter 4 it was mentioned that a low transmission mesh was used during CEM calibration to act as a beam attenuator. At the time of the CEM measurements it was assumed that this mesh had a transmission of 1% based on the geometric open area, but it was also noted that this figure might be inaccurate.

After the MCP had been calibrated against the CEM an oportunity arose for the mesh transmission to be measured in the DTF. This was done at 30.4nm and a figure of 1.4% resulted. The measurement was not a precise one as time did not allow it to be refined, so an error of perhaps 25% is realistic.

The implications for the measurements reported in this and the previous chapter are of CEM QE reduced by a factor of 0.7 ± 0.18 and MCP QE similarly reduced. This of course still assumes that the mesh transmission is independent of wavelength. A reduction in MCP efficiency of 70% brings the measurements of figure 5.41:1 almost into agreement which the predicted figures of reference 2.

5.60 Conclusions.

XUV quantum efficiencies of a CsI coated imaging MCP detector have been successfully measured to within 25% over the wavelength range 16 to 60nm, extending the total range of calibration to 4.4 to 60nm. The measurements demonstrate that efficiencies up to 60% can be expected of flight instruments in the principal filter wavebands[5]. WFC detector QEs and their variation with wavelength and angle of illumination have been shown to be in general agreement with the predictions of Fraser[2,9], based on a theoretical model of MCP photocathodes.

CHAPTER 6

The Measurement of Mirror Reflectivities.

6.10 Introduction.

The completion of the detector quantum efficiency measurements coincided with the arrival at Leicester of the first of the three WFC mirrors. This mirror was the middle mirror of the nest of three and was designated M2, the inner mirror being M1 and the outer M3. Design and manufacture of the mirrors has been briefly described in chapter 1.

Fabrication of M2 had not been without problems and the finish to the eye was not as free of blemishes as had been hoped, for example there were numerous 'comet tail' lapping marks in the polished surface which were a legacey of indifferent nickel plating. Also as a result of the nickel plating, metrological data revealed significant departure of the measured profile from that specified.

As M2 was in effect a development model, initial optical, soft X-ray, and XUV measurements on that mirror were conducted in order to decide whether or not it should be returned to the manufacturer. Largely as a result of optical measurements, M2 was indeed sent for refurbishment. This chapter describes the optical and XUV tests performed on M1 and M3.

6.20 Optical Testing.

The optical testing of the mirrors was performed by R. Willingale, J. Spragg, and the author. The aim was to quantify the focusing performance of each mirror in turn by illumination with a parallel beam on axis across the full aperture. Producing a light source with a parallel beam some 500mm across presents some difficulty, so an autocollimation technique was adopted as illustrated in figure 6.20:1.

In this scheme a laser beam is focused onto a ground glass screen and the spot thus produced acts as the source spot for the mirror. If the spot is located accurately at its focus, the mirror produces a parallel beam which is reflected from a plane mirror to re-enter the mirror and converge to a focus on the screen. This 'return' spot contains information about the size of the source spot and the focusing ability of the mirror, and in the situation where the source spot is sufficiently small the size of the return spot is a measure of the quality of the mirror.

Two main parameters influence the focus of the mirrors, apart from the abberations which are inherent in the mirror design[1], and these are the reflecting surface finish and the mechanical tolerance

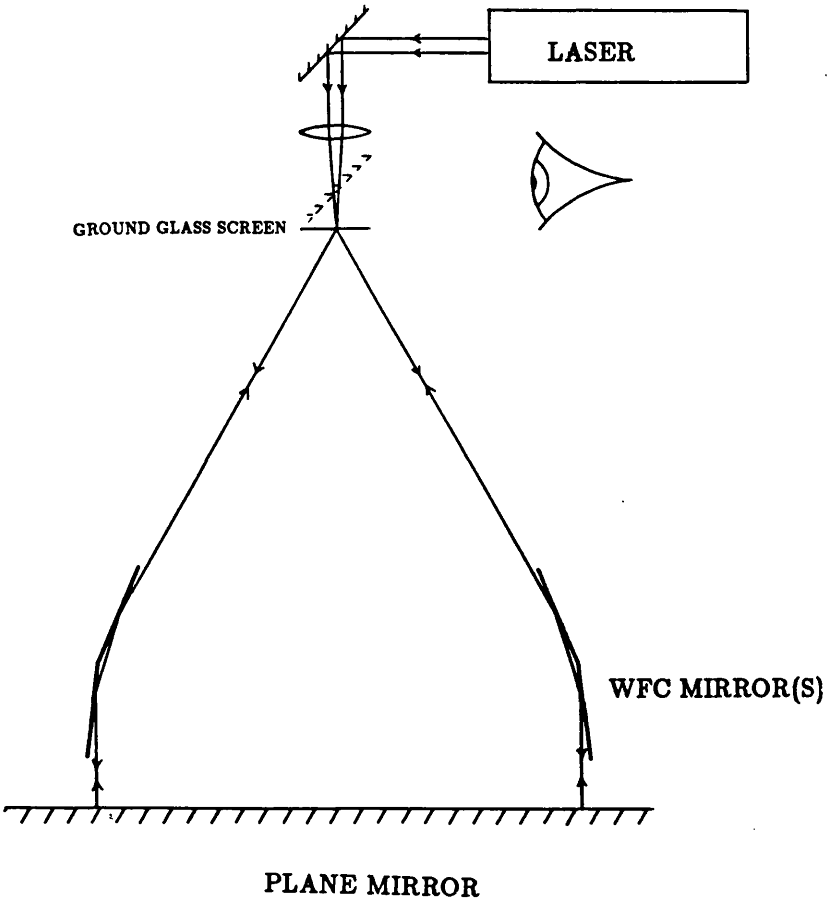

Figure 6.20:1 **Apparatus for the full aperture optical tests on the WFC mirrors.**

achieved during manufacture. At optical wavelengths the surface finish of an XUV mirror is of such quality that it does not influence its performance[2], optical tests therefore are only sensitive to the departure of the surface figure from the specification, and to deformations of the mirror shell.

The size of the return spot, and hence the mirror performance, was measured by photographing the ground glass screen using the inclined half-silvered mirror illustrated in figure 6.20:1 together with a camera equipped with a suitable magnifying lens. Microdensitometer traces of the negatives like that in figure 6.20:2 were calibrated by measuring the distance between source and return spot on the glass screen using a travelling microscope. With the mirror focusing under optimum conditions, ie. with a small source spot at the mirror focus and with the return spot close to it, it was found that the measured Full Width at Half Maximum (FWHM) of the return spot was within specification. Indeed it is very likely that a substantial part of the measured widths were due to the finite size of the source spot, the sharpeness of the camera focus, and the response of the film. As far as this latter point is concerned, some effort was put into ensuring that the exposure was not at the limit of the film response. Figure 6.20:3 shows a graph of exposure (lens stop) vs. film density on which the nominal exposure used is indicated.

6.30 Experimental Details for Reflectivity Measurements.

6.31 The Mirror Test Facility (MTF).

All soft X-ray and XUV tests on the WFC mirrors were performed in the MTF of which a photograph and schematic diagram are included in figure 6.31:1.

The source end of the facility can be occupied either by a conventional Coolidge type soft X-ray source[3] or else by the Penning source and Monochromator (chapter 3). Vacuum modifications to the monochromator made to reduce the likelyhood of an oil contamination accident have been described in section 3.60 and the changes in PS behaviour introduced have been discussed. One further modification to the monochromator, the inclusion of a 0.35mm diameter hole in place of the exit slit, was dictated by its location at the focus of the MTF collimator.

The collimator is of the Kirkpatrick-Beaz design[4] consisting of two glass plates, bent to parabolae using a bending jig, each focusing in one axis. The vacuum tank containing the collimator comprises the centre section of the test facility (figure 6.31:1). From this tank, the parallel beam passes to the slit chamber where two sets of four slits may be used to define the beam passing into the mirror tank.

For the reflectivity measurements described here, both M1 and M3 were mounted on their three-pronged support, the mirror 'spider', and together placed inside the MTF mirror tank. This large vacuum tank

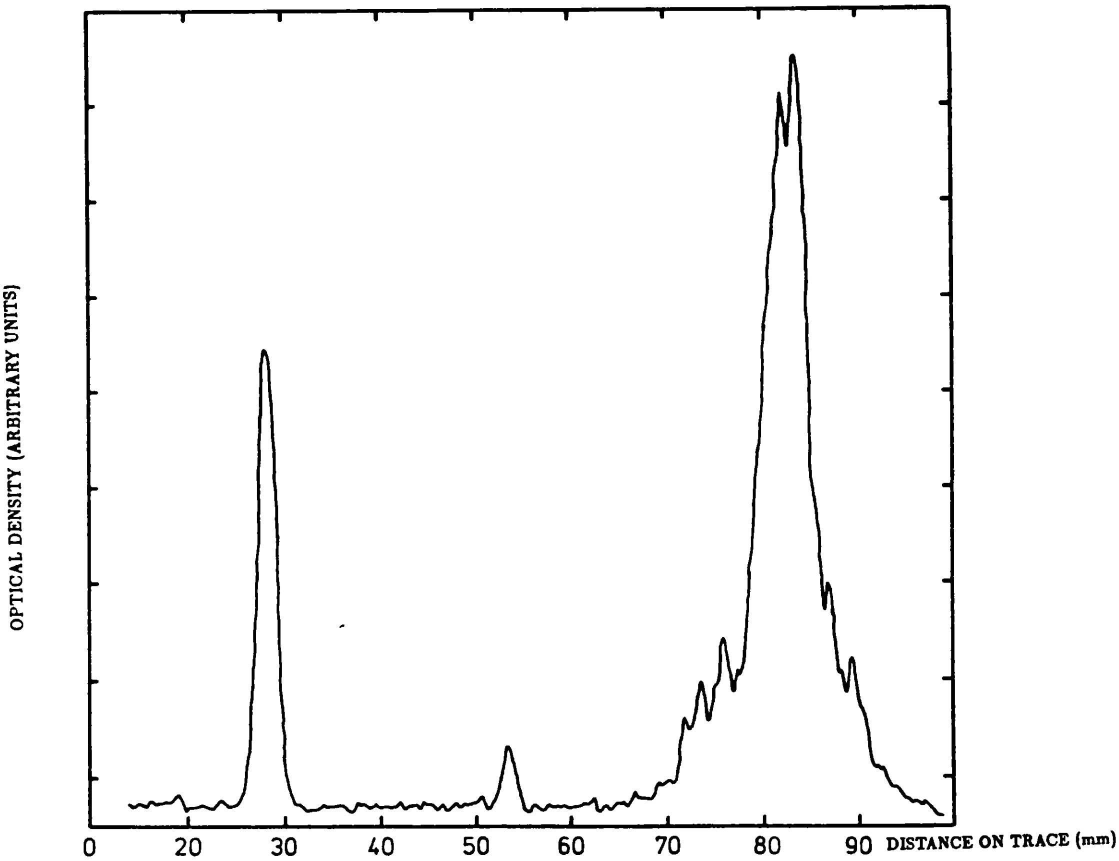

Figure 6.20:2 Microdensitometer trace of the source and return spots on a optical test negative.

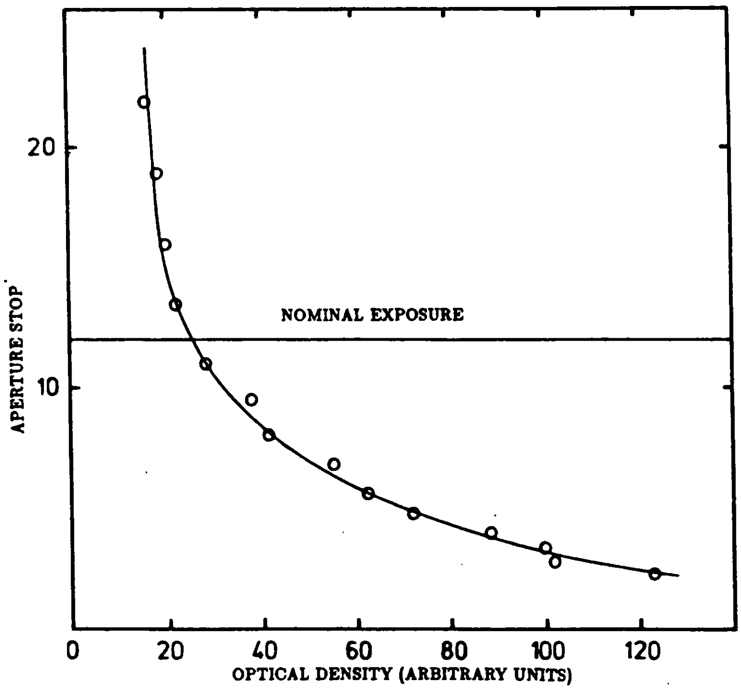

Figure 6.20:3 Plot of camera stop vs. measured optical density to determine nominal exposure.

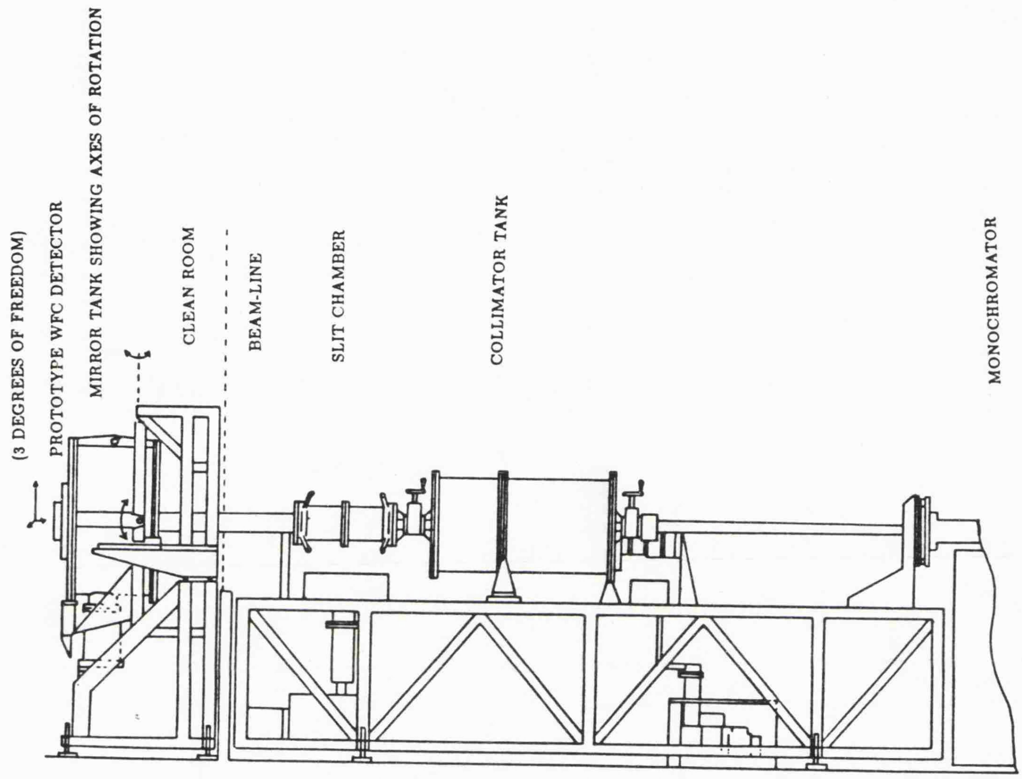

Figure 6.31:1 The Mirror Test Facility.

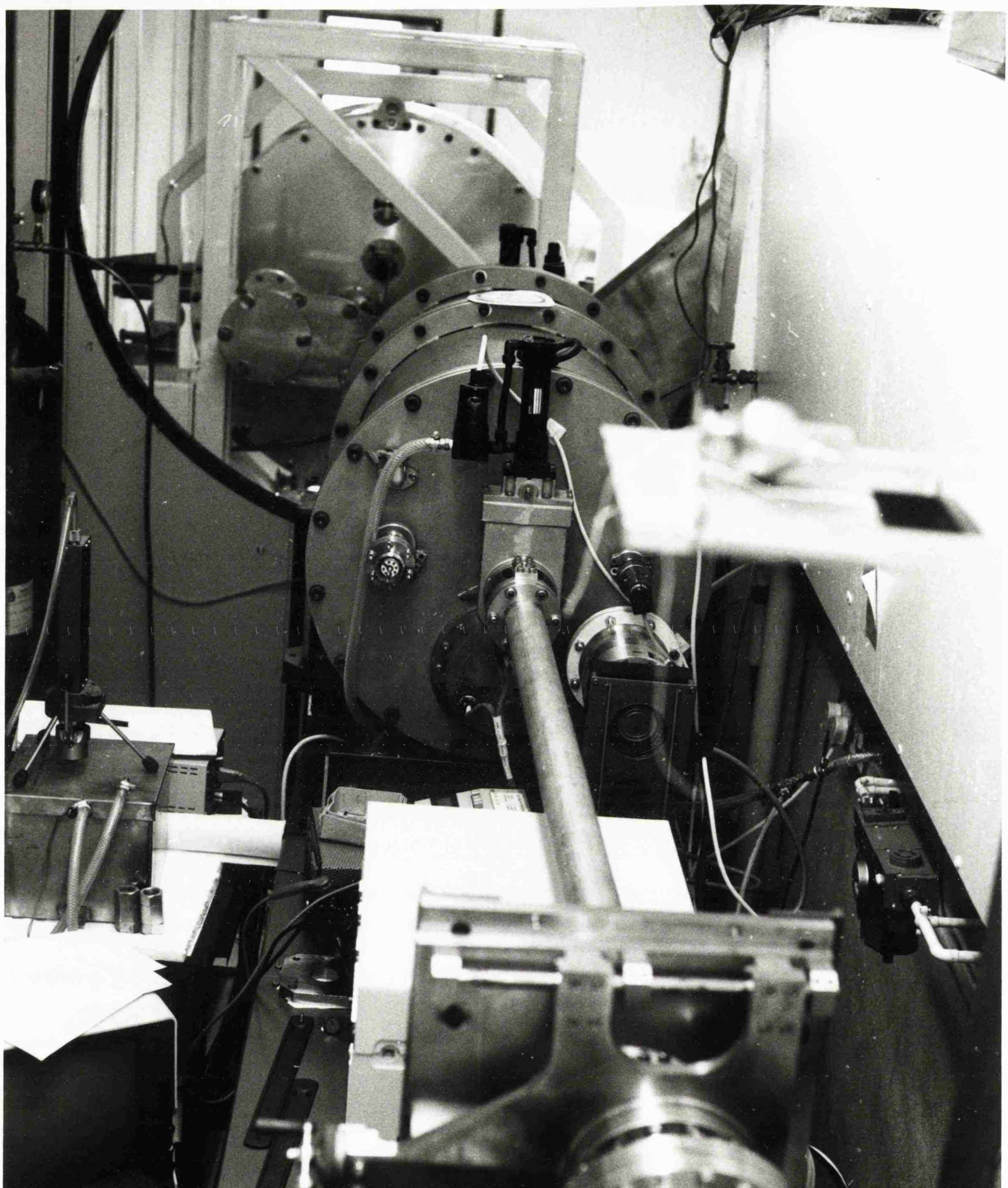

is situated inside a class 100 clean room so that the mirrors when not inside the tank are protected from the dust and hydrocarbon contamination which would impair their performance. The tank itself is mounted in a large floor standing frame which allows it to be rotated about the vertical and one horizontal axis and to be moved from side to side by about 100mm. These axes and senses of rotation are shown in figure 6.31:1, and in addition the mirrors may be rotated inside their tank about their common optical axis. The movements of the mirrors and mirror tank allow the stationary pencil beam from the slit chamber to be scanned across the mirror apertures. Motion of the tank is catered for by a flexible vacuum bellows between the slit chamber and the mirror tank, and the extent of any movement is displayed by an electronic read-out system.

On the back of the mirror tank there is three-motion carriage on which is mounted a WFC style detector (see chapter 5). The carriage allows, via another bellows, linear movement in the three axes illustrated in figure 6.31:1. The detector is mounted nominally at the focus of the mirrors to intercept the reflected beam from the mirrors, but there is sufficient movement built into the mirror tank so that it can be rotated and translated until the straight through beam, i.e. that directly from the slit chamber, falls on the detector surface. In this tank position the beam passes through the open centres of the mirror shells.

Electronics for imaging MCP detectors similar to that used for reflectivity measurements has already been described in chapter 5.

6.32 Measurement Proceedure.

The reflectivity, or reflecting efficiency, of a surface is defined as the ratio of the intensity of a beam reflected from the surface to that incident on it. In principle then, finding the reflectivity of the WFC mirrors is a simple matter of comparing the count rate with the mirror tank in the reflecting position with that in the straight through position. This gives the reflectivity of the binary mirror system, as two reflecting surfaces are of course involved.

Unfortunately, complications were introduced as a result of variations in quantum efficiency of the MCP detector with angle of illumination (a phenomenon that was discussed in chapter 5), variations in sensitivity with position, and the limited dynamic range of the detector system.

Not only does the QE change with angle, but the variability is a function of wavelength so that QE vs. angle behaviour, previuosly measured for selected wavelengths[5], was not sufficient data with which to apply a correction. It was therefore necessary to measure the relative efficiency of the detector at the various MTF incidence angles at as many wavelengths as possible.

Table 6.32:1 shows the results of a series of measurements conducted largely by M. A. Barstow using the Detector Test Facility. Included in the table are values of QE(ST)/QE(Mn) interpolated from adjacent figures, where no measured result was obtained, these are marked '*'.

When reflectivity results were first obtained it became apparent that there was a problem, since at least on two occasions reflectivities greater than unity were measured. The problem was eventually traced to the low gain of the MTF detector. Having been constructed with a front MCP which had initially been incorrectly manufactured and subsequently reprocessed, this detector had a somewhat lower peak gain than specification, also, it had accumulated a large total count since being assembled and so had a broad Pulse Height Distribution (PHD). The low MCP gain had severe implications for the detector electronics designed for use with a flight specification detector.

The miss-match between detector and electronics was a limitation, but as long as a careful watch was kept on the count rate and the pulse height distribution no significant loss of counts was experienced. As has already been noted in chapter 5, high count rates result in depression of the peak MCP gain as a consequence of the RC time constant of the channel multipliers. More accurately, gain suppression is a count rate density effect so that when a given count rate occurs over a small area of the MCP, the gain is reduced more than if the same count rate is spread over the whole detector area.

The reflectivity measurements represent just such a situation. When the straight through beam fell on the MCP surface it had dimensions of 4 $\times$ 4mm, whereas the focused spot from a mirror had a diameter of approximately 0.1 mm—a thousand fold increase in count rate density. The result in initial measurements was that if the count rate was allowed to get too high, counts would be lost from the reflected beam measurement because the gain drop pushed them below the lower level discriminator (LLD) setting of the system, into the noise.

In addition, if the detector gain was increased to minimise this effect, it was found that when the straight through beam fell on the detector towards its edge, the high gain and broad PHD under these illumination conditions resulted in counts being lost above the ADCs limit. This was because towards the edge of the field, one of the ADCs has to cope with most of the readout charge instead of approximately one quarter as is the case at the detector centre. Both these count loss situations are illustrated in figure 6.32:1, which shows a PHD in which counts from the focused beam are lost below the LLD, and one in which the high charge tail is cut-off for the straight through beam.

Another experimental complication was brought to light when a WFC detector was illuminated with an intense, focused, beam. When the spot on the detector surface was moved through distances of the order of 0.1–1.0mm, different count rates were recorded which suggested variability in the photocathode

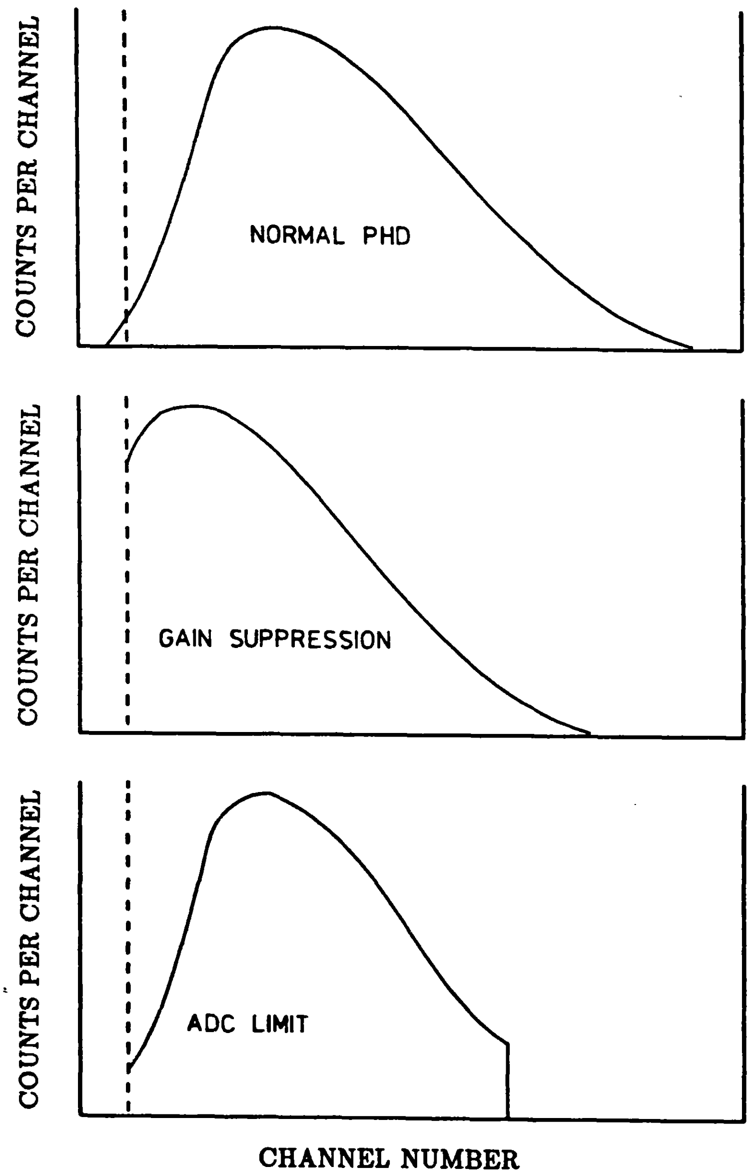

Figure 6.32:1 The loss of counts from a pulse height distribution through gain supression and ADC dynamic range miss-match.

Wavelength(nm)	$1/C_1$	$1/C_3$
4.47	0.97±0.02	0.91±0.02
11.4*	1.04±0.13	0.89±0.11
13.0	1.19±0.15	0.64±0.11
16.0	0.99±0.02	1.02±0.02
20.9*	0.99±0.09	0.96±0.08
25.6	0.99±0.09	0.87±0.08
30.4	0.90±0.03	0.83±0.03
42.0	0.93±0.03	0.87±0.03
58.4	0.97±0.02	0.95±0.02

Table 6.32:1 Detector correction factors, C_n, used during mirror measurements.

quantum efficiency on this scale. For the reflectivity measurements, this problem was overcome by stepping the detector a distance of 0.5 mm every 30 seconds during a count rate integration, thus averaging out the effect. Further investigation of this apparent small scale variability is underway at Leicester.

The detector problem having been resolved, measurements could proceed and the first was aimed at ensuring that the collimated X-ray beam fell on the correct part of each mirror. This was effected by scanning the mirror tank in translation across the nominal position of the mirror aperture, whilst recording the reflected count rate. By this technique, the middle of the front reflecting surface for each mirror was located as the mid-way point between the extinction points caused by the beam missing the front surface altogether.

Count rates were recorded in the following manner for each wavelength so as to minimise the effects of source variability and detector background:

i) Background rate. The count rate in a box on the microcomputer screen (chapter 5) was measured with the mirror tank positioned so the no beam fell on the detector.

ii) Straight through rate. Count rate in the box with the tank positioned so that the unocculted beam was contained by the box.

iii) M1 rate. Count rate with the reflected spot from M1 in the box.

iv) M3 rate. As iii) but using M3 spot.

v) Straight through rate—as ii) to verify source stability.

vi) Background rate. As i).

The reflectivity was then calculated as:

$$R(Mn) = (RATE(Mn) - BGND) * Cn/(ST - BGND)$$

Cn is the detector angle correction for the appropriate mirror angle and wavelength from Table 6.32:1.

6.40 Results.

Two surface reflection efficiencies were measured at the wavelengths listed in Table 6.40:1, which also includes the source gas, approximate source conditions, and where possible the identity of the emission line. The range of measurement extends from 58.4nm to about 9.5nm using the monochromator and PS, the latter measurement requiring the use of a WFC style carbon/lexan filter[6] to eliminate long wavelength background light, visible towards the short wavelength limit of the instrument (chapter 3). Two wavelengths were accessible using the Coolidge source, 4.47nm and 11.4nm, using a carbon target plus macrofol filter, and a beryllium target respectively.

TABLE 6.40:1

Measured WFC Mirror Reflectivities

Wavelength(nm)	**Energy(eV)**	**M1, M3 Reflectivities(%)**	**Source conditions**
4.47 C_k	277	2.7±0.6, 1.2±0.4	(Coolidge) Carbon target+filter
9.5 Al	131	57±19, 42±15	(PS) Argon: high current
10.9 Al	114	44±5, 41.5±4.0	(PS) Argon: high current
11.4 Be_k	108.8	48±2, 50±2	(Coolidge) Berylium target
13.0 AlIII	95.4	44.8±2.5, 52.7±4.0	(PS) Argon: high current
16 AlIV	77.5	48±3, 40.5±5.0	(PS) Argon: moderate current
20.8 Ne	60	45±5, 32±4	(PS) Neon: high current
25.6 HeII	48.0	47±3, 39±2	(PS) Helium at moderate current
30.4 HeII	41.8	52.7±2.5, 46.3± 2.5	(PS) Helium: moderate current
42.0 NeIII	29.8	54±2, 53±2	(PS) Neon at moderate current
58.4 HeI	21.2	56±4, 47±4	(PS) Helium: high current

To check that the mirror surfaces were uniform over large areas, the reflectivity was measured at a number of positions around the mirror apertures. Also, the size of the pencil beam and the steep surfaces meant that at each position, the beam intercepted the front surface over at least 50% of its length, this is illustrated in figure 6.40:1.

Figures 6.40:2 and 6.40:3 show the measured reflection efficiencies for the M1 and M3 mirrors. The measurements are represented by dots with error bars that indicate the uncertainties due to counting statistics and source variability. Other systematic errors due to the PHD problems discussed in section 6.32 and the errors in the detector angle correction measurements are not included but are thought to amount to an additional 3%. Wavelength errors are indicated for the short wavelengths lines from the PS where monochromator background made spectral purity difficult to guarantee, and for the wavelengths generated using the Coolidge source.

Both curves in figures 6.40:2 and 6.40:3 are calculated reflectivities based on published optical constants for gold, those for the full lines are taken from Henke[7] while those of the broken lines are from Hagemann[8].

6.50 Discusson of the Results.

Both the full and the broken lines of figures 6.40:2 and 6.40:3 were calculated using the Fresnel equations[9], but with optical constants from two sources. The constants published by Henke and Hagemann were calculated using anomalous dispersion theory from photoabsorption cross sections derived from transmission measurements. Indeed the constants are based on the same data in the 100 to 200eV band, although the resulting reflectivity predictions here differ as figures 6.40:2 and 6.40:3 show.

Looking at the differences between theory and measurement, it is clear that for both mirrors the agreement is good below about 40eV (Hagemann) and above 150eV (Henke). Between these limits, however, there is a significant discrepancy which is more pronounced for M3 with a maximum difference of approximately 15% at 60eV. Such differences between measured and predicted reflectivities could be attributed to the following causes:

1) The density of the sputtered reflecting layer may be lower than that of bulk material.
2) Scattering or shadowing by surface roughness features may lower the reflectivity.
3) The presence of surface contamination may lower the reflectivity.
4) The optical constants upon which the predictions are based may be incorrect.

It is well known that the density of evaporated or sputter coated films may be lower than the bulk density of the material, indeed Henke cites this as a common reason for disagreement between

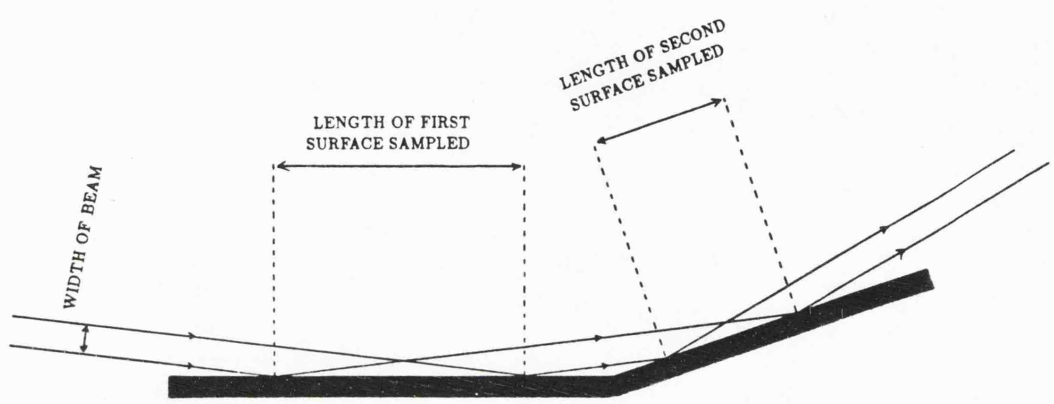

Figure 6.40:1 A pencil beam samples a long strip down a mirror surface due to the small grazing angle of incidence.

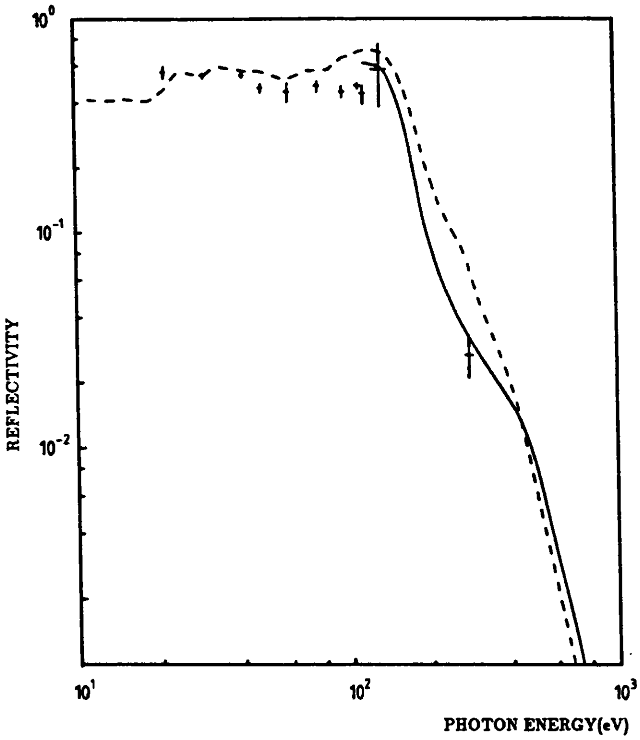

Figure 6.40:2 Measured two-surface reflection efficiencies for the M1 mirror compared with calculations based on Henke (—) and Hagemann (- -) optical constants.

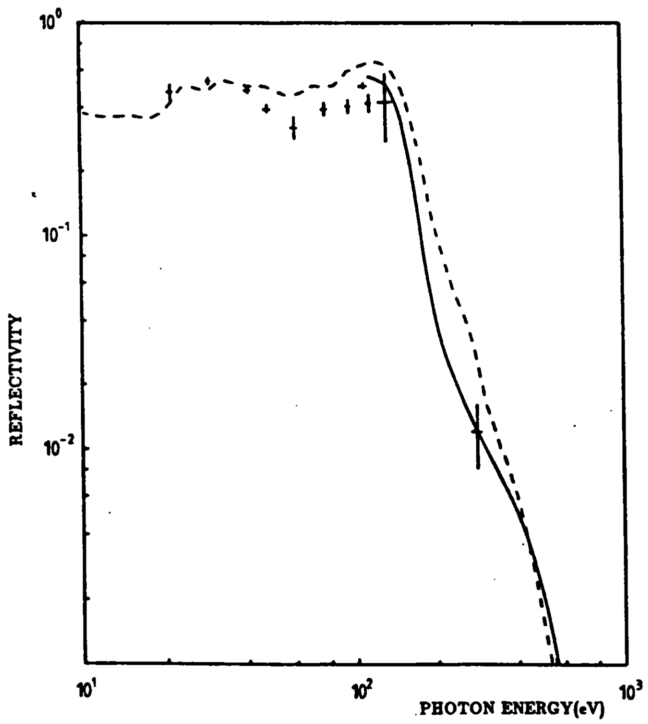

Figure 6.40:3 Measured two-surface reflection efficiencies for the M3 mirror compared with calculations based on Henke (—) and Hagemann (- -) optical constants.

measurement and theory. However, calculation showed that in order to restore agreement in the range 40 to 150eV it was necessary to reduce the film density by nearly a factor of two, and then the fit outside this range was very much worse; figure 6.50:1. For this reason, and the fact that it seems unlikely that the density could be so low given a sputtering pressure in argon of $\approx 10^{-5}$mbar during gold deposition, low density cannot be the dominant effect.

Considering the second point above, the advantage of making the reflectivity measurements using an imaging detector becomes apparent as any scattering problem is easily recognised. As mentioned in section 6.32, all reflectivity count rates were measured using a box, or image window, ensuring a low background count. In order that the measurements be effected by scattering from a rough mirror surface, it would be necessary for XUV light to be scattered beyond the limits of the image window used. This is discounted, however, as long exposures of the reflected beam using the full detector area did not show measurable scattered intensity beyond 12 arc seconds from the specular direction, whereas a 60 arc second window was used throughout the reflectivity measurements.

Surface contamination, especially by hydrocarbons, is a well known problem with X-ray optics and has the effect of reducing reflection efficiency; in the case of synchrotron optics thermal failure may also result. To explain the observations by this mechanism requires a surface layer of hydrocarbon (or carbon for computational purposes) approximately 2.5nm thick. Such a layer should exhibit 10% less reflectivity than is predicted for gold at 100eV but below 80eV, the cut-off energy of the layer, its reflectivity should be comparable with that of gold. In addition there would not be much effect at 277eV (C_k) as the layer would largely be transparent here so that the gold reflectivity would dominate. Hydrocarbon contamination is then a good candidate as the cause of the low reflectivity, but this conclusion must be viewed in the context of the two models chosen since the explanation in terms of oil layers is only convincing if the Hagemann curve is adopted at low energies and the Henke curve at high energies. If the measurements are compared with the Hagemann curve only then hyd rocarbon contamination cannot account for the discrepancy at 277eV.

The difference between the two theoretical curves is disturbing, particularly as they are both based on the same absorption data in the region around 100eV. For M1 the difference between the curves is comparable with the difference between the measurements and theory, so it is not unreasonable to suppose that the optical constants are in error and that this is the reason for the dissagreement.

To clarify the origin of the differing predicted reflectivities figure 6.50:2 shows the absorption data upon which the calculated optical constants are based. Clearly the absorption coefficients from the two sources are in substantial agreement, however, if this is compared with the real part of the atomic

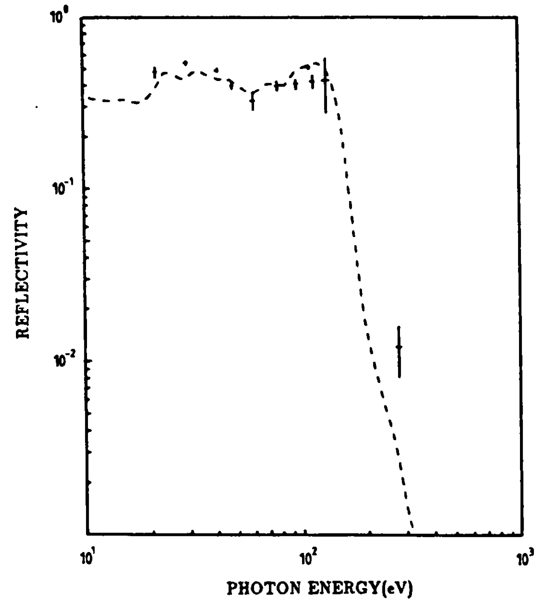

Figure 6.50:1 Best fit to the measured M3 reflectivities using the Hagemann optical constants and varying the film density.

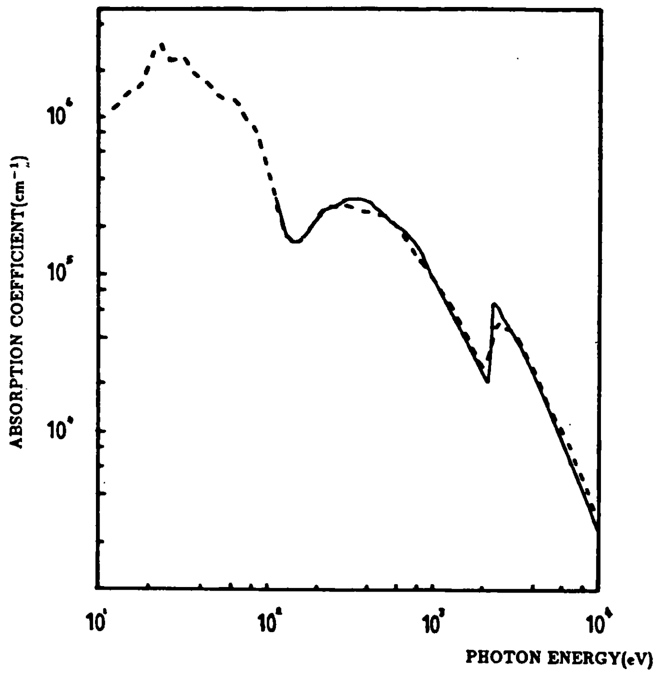

Figure 6.50:2 Absorption coefficients used by Hagemann and Henke to derive optical constants for gold.

scattering factor as plotted in figure 6.50:3a some discrepancy has been introduced.

Atomic scattering factors can be calculated from absorption coeffcients using the Kramers-Kronig integral:

$$f_1 = Z + C\int_0^\infty \frac{\epsilon^2\mu_a(\epsilon)d\epsilon}{E^2-\epsilon^2} \qquad 6.50:1$$

this may be derived by the application of anomalous dispertion theory[7], but as Henke has pointed out the result is strongly dependent on the accurate knowledge of absorption cross sections for a wide range of energies. f_1 from equation 6.50:1 is the real part of the complex atomic scattering factor which describes the way in which light propogates in absorbing media, thus the reflectivity of a material is dependent on f_1. The imaginary part of the scattering factor, f_2, is related to the absorption cross section by:

$$f_2 = (1/2)\pi C E\mu_a(E). \qquad 6.50:2$$

$$C = (\pi r_o hc)^{-1}$$

and describes the absorption of a medium. Figure 6.50:3b shows that there is good agreement between Henke and Hagemann for the value of f_2 for gold, particularly around 100eV where the same absorption data was used.

To decide whether an error in the real part of the atomic scattering factor could produce the kind of discrepancy observed, a scaling factor was introduced and reflectivities were recalculated. Figure 6.50:4 shows that a good fit to the measurements is obtained with a scaling factor of 0.67. Since the density is also a parameter of the reflectivity calculation, this was then varied with the f_1 scaling giving the result that a density change of +1.08 times with a scaling of 0.68 was required to give the curve of figure 6.50:5.

Malina and Cash[10] have published measurements of the reflectivity of deposited gold surfaces in the WFC waveband. Their measurements were made on small scale sample flats, fabricated by deposition of nickel onto beryllium substrates, polishing, and finally gold coating. The flats thus represent a similar surface to the WFC mirrors particularly as the gold deposition was conducted at similar pressures and rates.

Figures 6.50:6 and 6.50:7 show the WFC measurements compared with data from reference 10. The published reflectivities at grazing angles of 7.5 degrees for M1 and 8.5 degrees for M3 were squared to represent reflection from two surfaces.

* Z is atomic number of the material, $\mu_a(\epsilon)$ is the absorption coefficient at energy ϵ, E is the photon energy, and r_o is the classical electron radius.

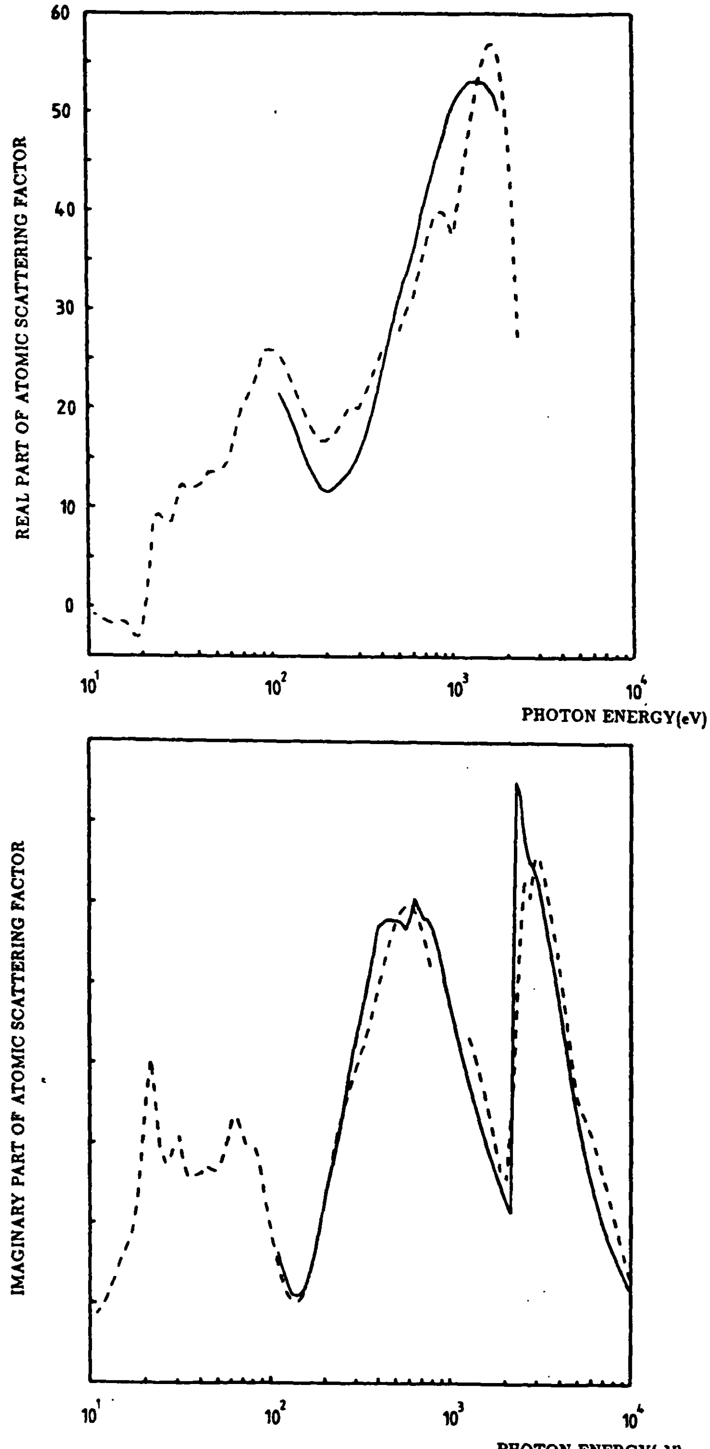

Figure 6.50:3 The real (f_1) and imaginary (f_2) parts of the atomic scattering factors for gold, from Henke (—) and Hagemann (- -).

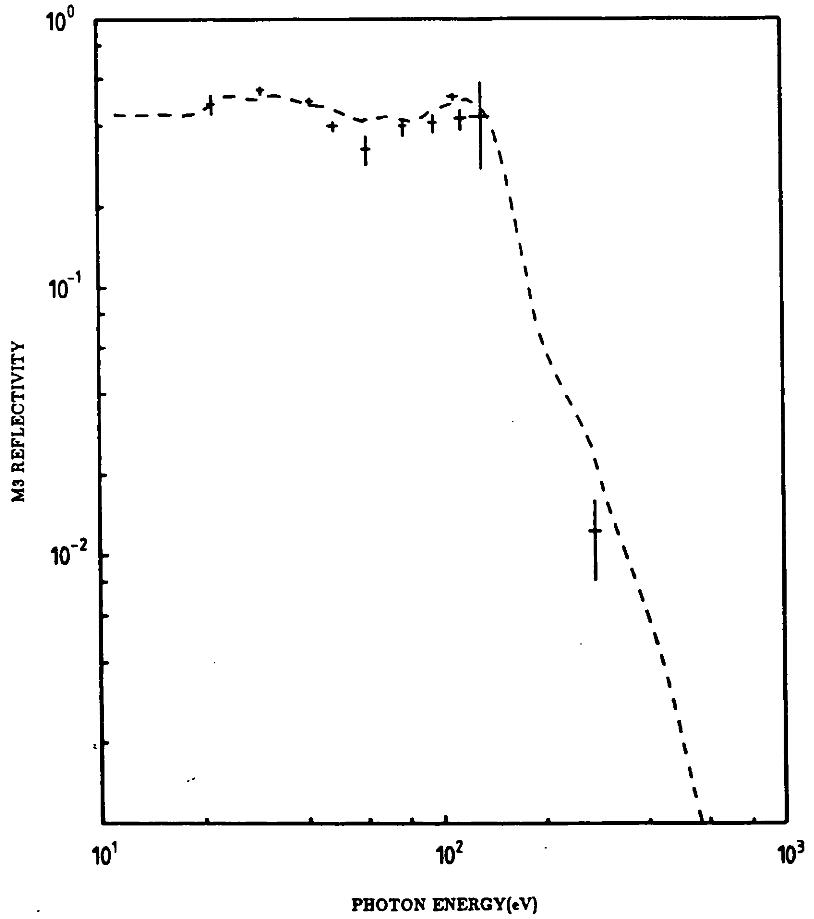

Figure 6.50:4 Best fit to the measured M3 reflectivities using the Hagemann optical constants with a scaling factor for f_1 of 0.67.

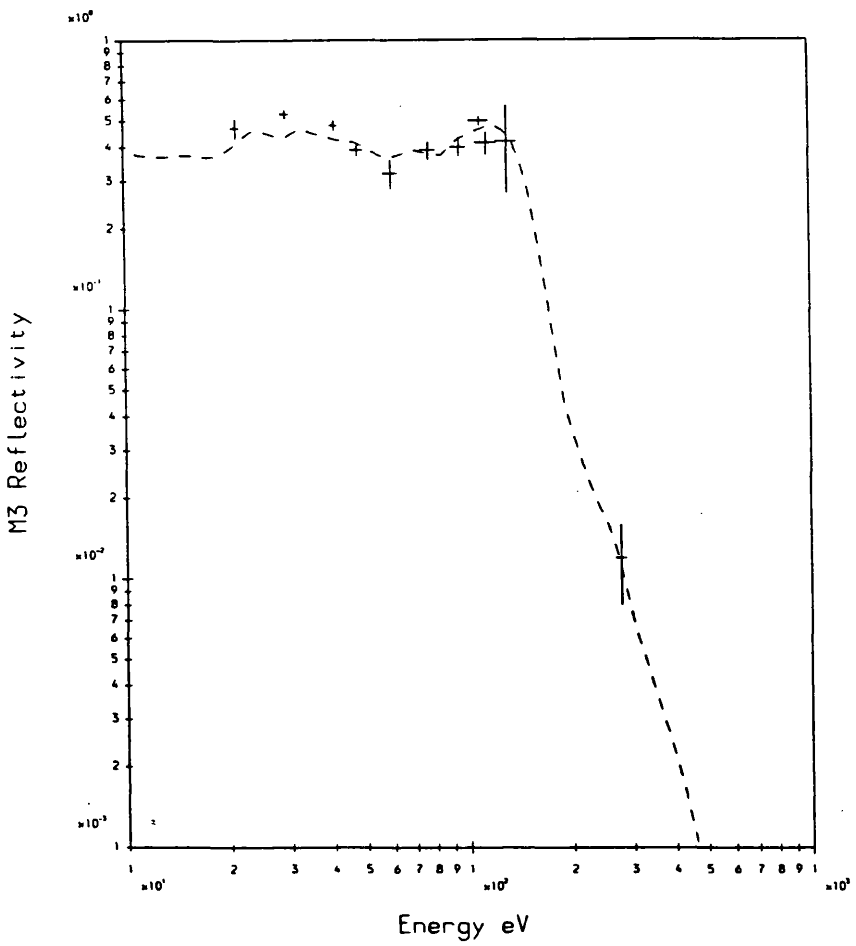

Figure 6.50:5 Best fit to the measured M3 reflectivities using Hagemann optical constants and varying film density and f_1 scaling.

The two sets of data are in very good agreement particularly for wavelengths longer than 9nm, though the published figures at 4.4nm are rather low compared with those measured at Leicester. This may be a result of the greater surface roughness quoted by Malina and Cash (2–2.5nm RMS) compared with that measured for the WFC mirrors (<1nm).

6.60 Conclusions.

The two surface reflection efficiencies of the inner and outer WFC mirrors were successfully measured for wavelengths between 4.4 and 58.4nm. All results were within 15% of values calculated using the Fresnel equations with published optical constants. It has been shown that the discrepancy between measurement and theory can be reduced by scaling the real part of the atomic scattering factors published by Hagemann. Differences between reflectivities calculated using constants from these sources indicate that the optical constants for deposited gold may still be inprecise.

A qualitative understanding of the departure of theory and experiment is also possible by hypothesising a 2.5nm layer of hydrocarbon contaminant. Such contaminants were known to be present in the vacuum chamber, at a low level, during the measurements, but a more significant contamination risk was probably posed by the clean room conditions under which the mirrors were handled when not in the MTF tank. No continous monitoring of hydrocarbon levels was possible during the handling operations so conaminant concentrations were unknown. However, the clean room was equipped with hydrocarbon filters to minimise the effect of sources of contamination from outside the clean area.

Optical and XUV measurements have shown the Wolter-Scwartzschild profiles and the surface microroughness to be within specification.

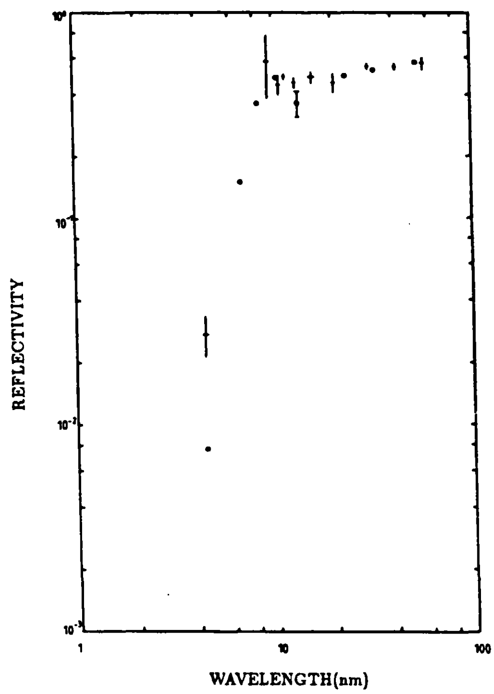

Figure 6.50:6 Comparison of measured M1 reflection efficiencies with the square of the 7.5 degree reflectivies measured by Malina and Cash (reference 10).

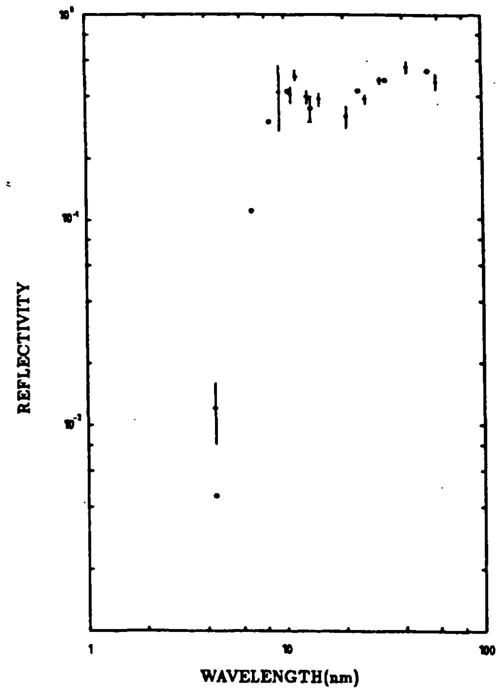

Figure 6.50:7 Comparison of measured M3 reflection efficiencies with the square of the 8.5 degree reflectivies measured by Malina and Cash (reference 10).

CHAPTER 7

WFC Particle Background Reduction.

7.10 Introduction to WFC Backgrounds.

Apart from self generated phenomena such as detector hotspots, there are two expected causes of background in WFC images attributable to sources external to the ROSAT spacecraft. These are XUV photons and charged particles.

The photon component is a result of two types of background; the general XUV cosmic sky background and scattering of sunlight by ionic and atomic species local to the Earth. The cosmic background is broad band in spectrum and can be modelled by supposing a black body spectrum for the emission between 50nm and 175nm, with a temperature of about 10^4K. This temperature is consistent with contributions from O and B type stars[1]. At shorter wavelengths a temperature of 10^5K is more appropriate. A more complete discussion of this background is to be found in reference 1, and in references therein.

Scattering of sunlight by ions and atoms in the vicinty of the Earth causes background emissions known as geocoronal and airglow backgrounds respectively. Both these effects have the form of line emission. Most significant are the lines at 25.6nm, 30.4nm, and 58.4nm due to HeII and HeI and the Lyman series of hydrogen at 121.6nm and 102.5nm, plus the 130.4nm line due to OI. The majority of this scattered light has its origin close to the Earth because of the population of resonant scatterers in the plasmaphere, but there is also a contribution from the interplanetary medium.

Geocoronal and airglow backgrounds have been the subject of considerable experimental investigation[eg. 2, 3, and 4], and have been successfully modelled using the theory of radiative transfer[5]. It is therefore clear that this background extends into the Earths shadow because of the extent of the scattering atmosphere (see figure 7.10:1). Published 30.4nm HeII geocoronal background measurements show that fluxes in the range 1–10 Rayleighs ($10^6 s^{-1} cm^{-2} str^{-1}$) might be expected in some viewing directions.

Any space experiment is subject to a barrage of high energy, ionizing radiation. Fortunately, the WFC body will exclude most of this and the interaction cross section of the detector to that fraction which does penetrate the telescope structure, will be small. Electron ranges in aluminium are typically less than 4mm for energies less than about 10MeV.

In addition to the 'direct' high energy particle environment from the sun and cosmic sources, there

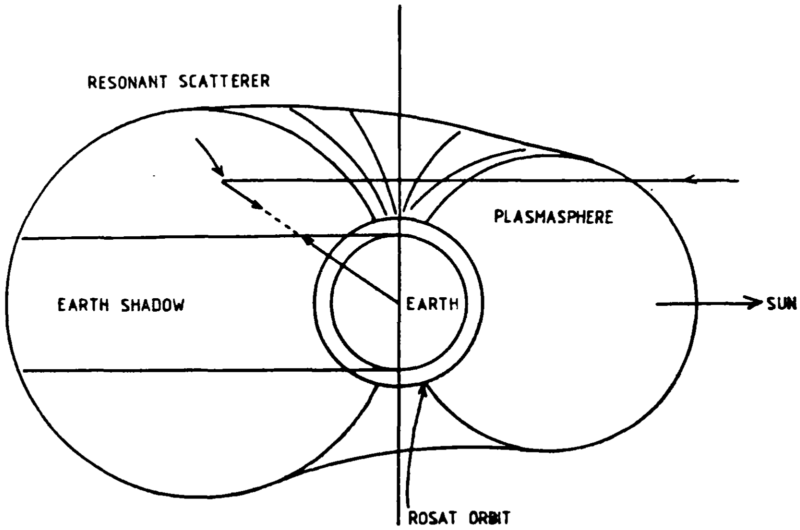

Figure 7.10:1 Scattering of sunlight into the earths shadow by ions and atoms in the plasmashere.

is also a population of particles (mostly energetic electrons) associated with the Earths magnetic field occurring in well defined regions or belts. Close to the Earths magnetic poles, the trapped or quasi-trapped electrons in the radiation belts, interact with the atmosphere producing aurorae. This gives the areas close to the poles the name 'auroral zones', and the altitude and inclination of the ROSAT orbit will be such that the satellite will pass into them.

Should auroral electrons manage to propogate through the mirrors, they would constitute a potentially hazardous background in the detector. The possibility of hazard stems from the finite lifetime of MCP detectors. It is well established that the gain of a microchannel plate declines with extracted charge[7], or in other words, with accumulated count. If then, the detector were to be regularly exposed to high background rates, the useful lifetime of the experiment might be reduced.

How effectively electrons could scatter through the mirror assembly in reality is something of an open question. The only experimental evidence encountered which was representative of the expected conditions, was that presented by Kanter[8]. This work on the scattering of 10 to 100 keV electrons from surfaces of aluminium and gold demonstrates a strong beaming of scattered flux close to the direction expected for specular reflection, a tendency which becomes pronounced at grazing angles of incidence at higher energies. It would therefore seem that significant disturbance to the WFC observing time may result from passage through the auroral zones[9], a conclusion which applies equally to the ROSAT main telescope[10].

It has not been possible to model the scattering of electrons from gold surfaces. Adopting a simple potential step to represent the surface, for example, demonstrates that significant specular scattering takes place especially at grazing incidence but that this tendency is less for higher energies contrary to the observations of Kanter. Probably Kanters results demonstrate that the electrons passing into the material surface undergo inelastic collisions within the metal resulting in the production of a nearly isotropic distribution of electron energies and directions. Kanters measurements were sensitive to electrons in the energy range $\Delta E/E=1$, where E is the incident electron energy.

Figure 7.10:2 shows the ROSAT orbit superimposed onto a map illustrating the extent of the auroral zones. Passage of the satellite through the auroral zones and the South Atlantic Anomoly (also associated with trapped electron populations) could result in the loss of observing time. Clearly this is a severe restriction, and with the transmission efficiency of the mirror for electrons unknown there exists the possibility that any other sources of electrons might interfere, at other latitudes, to the extent that the scientific objectives of the mission become compromised.

Candidates for these other electron sources are the bands, at mid-latitudes, of electrons precipitated

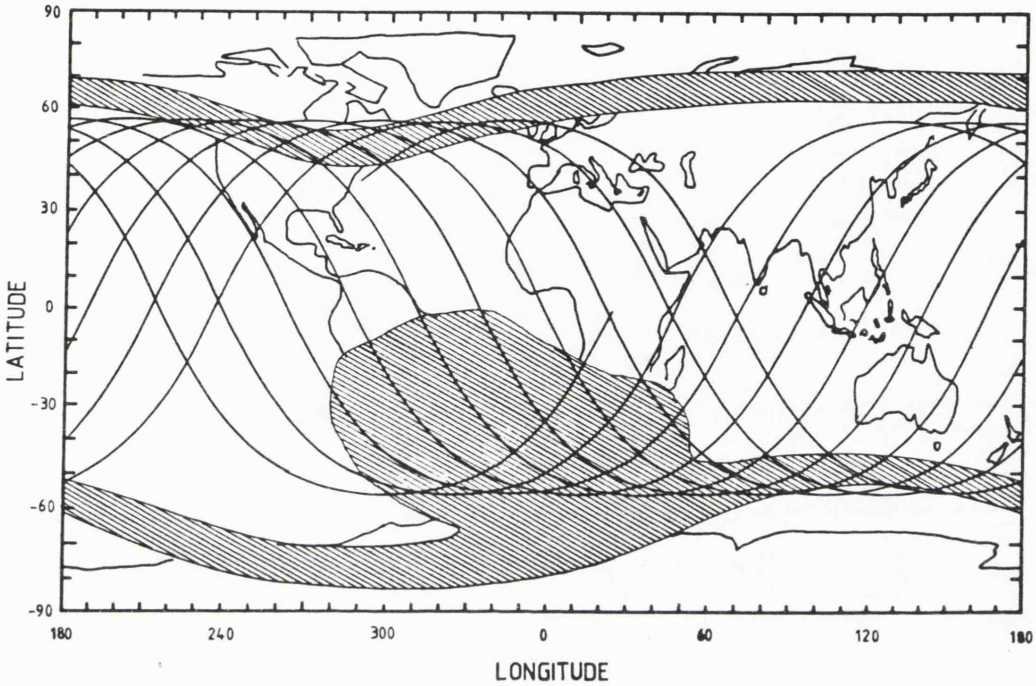

Figure 7.10:2 The ROSAT orbit superimposed on a map showing the auroral zones and South Atlantic Anomoly (shaded areas).

from the radiation belts by, it is thought, wave particle interactions in the magnetosphere[11]. Measurements of electron fluxes and spectra have been reported [eg. 12,13] but these do not provide a definitive prediction of levels likely to be encountered by the WFC since there are gross variations apparent with solar activity, direction of observation with respect to the Earths magnetic field, and altitude. It is, however, clear from figure 7.10:3b which models this component, that without some protection from electrons the WFC background rate could prove troublesome.

Figure 7.10:3 shows predicted background rates for two typical orbits; one in which the spacecraft encounters the auroral zones, and one in which it doesn't. These curves, generated by J. Daniels[6], show that the electron background may be expected to be between 500 and $10^6 s^{-1}$ in the energy band 10–50keV using the assumption that electrons propogate through the mirror system much as XUV light would.

7.20 Photon and Electron Background Exclusion.

Any broadband photon background in the XUV band, ie. from the diffuse cosmic sky background, cannot be excluded from the WFC because this would obviously also exclude sources of interest. EUV and UV, however, are distinct enough from the main observation band to be separable from it by means of filters.

It is the role of the WFC filters (chapter 1) not only to divide up the XUV band, so that colour photometry may be performed, but also to exclude long wavelength radiation, particularly that due to the 30.4nm HeII geocoronal line. Manufacture of the WFC filters is the responsibility of Dr. B. Kent, of RAL, and some progress has been reported[14]. Indications at the time of writing were that the cosmic background would dominate the line background due to the inclusion of filters. Representative count rates are 60 to 100 counts per second from cosmic sources and less than 4 counts per second from geocoronal and airglow sources.

The effectiveness of the filters as barriers to electrons is limited by their construction. The thickness of the WFC filters is of the order 500nm and they consist of multilayers of plastics with a coating of carbon, berylium, or aluminium. Thickness was optimised for the elimination of geocoronal background and is not sufficient to substantially attenuate a beam of electrons with energies greater than about 5keV[15]. Low energy electrons are excluded from WFC detectors by a repeller grid which is held at a potential of about 4kV with respect to the mirror assembly. In chapter 5, the function of the repeller grid in deflecting photoelectrons from the photocathode into MCP channels was described, and it was pointed out that a 100V potential was established between the grid and the front MCP. Since the potential of

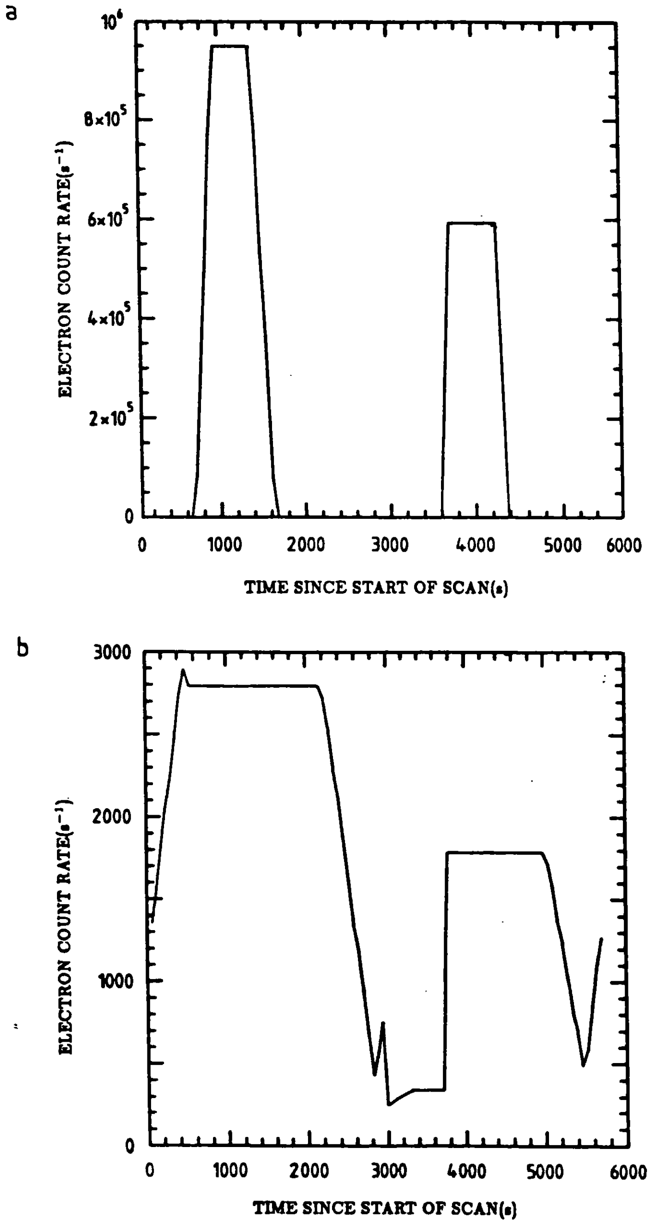

Figure 7.10:3 Predicted 10–50keV electron background rates: a) orbit penetrating auroral zones, b) orbit avoids auroral zones. The data, supplied by J. Daniels, assumes that electrons scatter through the mirrors efficiently.

the front MCP is approximately 3800V with respect to the WFC structure, the repeller grid effectivily excludes electrons with energies less than about 4keV from the detector.

Published electron spectra demonstrate a power law type spectrum which is strongly peaked at low energies[13], so it is not unreasonable to suppose that the chief background component will be from electrons in the range 10–100 keV. Any exclusion technique must rely on deflecting an offending particle rather than intercepting it, which in turn implies the use of electric or magnetic fields. Calculation shows the magnetudes of the fields required means that it is unlikely that anything more energetic than 100keV could be removed. Effectively the lower energy limit to the deflector transmission would be approximately 100keV.

Rather than deflect the electrons there exits the possiblity that the detector could be switched off upon entering regions of high electron density. This, however, might adversly restrict the observation time of the WFC if there exist at latitudes well separated from the auroral zones, significant areas of low energy electrons, and the scattering efficiency through the mirrors is high. A magnetic deflection scheme was thus adopted for the WFC because for electrons with energies as high as 100keV, the electric fields required to produce significant deflection would be so large as to threaten unwanted phenomena associated with the residual gas in the WFC (for example glow discharges). In addition there is the question of power requirements for high voltage supplies.

The attraction of using a magnetic field as a deflector was that at the cost of some additional spacecraft mass, the field could be generated by permanant magnets. One penalty for opting for a magnetic solution was, however, that it became somewhat more difficult to predict the effect on electron trajectories of a given field configuration than is generally the case with an electric field. The resolution of this problem is dealt with in the next chapter.

CHAPTER 8

Electron Diverter Performance.

8.10 Electron Diverter Design.

Imperial College of Science and Technology (ICST) were responsible for the design of the magnetic diverter within the WFC consortium, but preliminary simulation work was undertaken in parallel at Leicester. The initial design criteria may be summarised as:-

a) The combined mass of the magnets and support structure must lie within the budget allowed of 5.2 kg.

b) The highest possible field must be achieved in the X-ray beam path.

c) The whole structure must be as close to the mirror assembly as possible to maximise the effect of any deflection.

d) The resultant magnetic moment should be small to reduce the torque produced on the spacecraft by interaction with the Earths field.

e) The magnets should contribute no contamination risk to the mirrors.

f) The magnets should be held rigidly

A design of diverter was produced which at least fulfilled b), c) and f) above. The field strength and the total magnetic moment would then depend on the orientation of magnets chosen within the support structure. Figure 8.10:1 shows the structural design, but although the magnets are also illustrated there is no indication of the orientation of their dipole moments. This is because no attempt was made to decide between the two simple alternatives illustrated in figure 8.10:2 of either radially or alternately arranged magnetic moments. In order to distinguish the better design some detailed simulation of their behaviour was first necessary, and ultimately it was hoped to compare them experimentally.

The requirement for maximum field in the beam line dictated that the magnets be made of a material with a high remanence, together with a high coercive force. These quantities (B_r and H_c respectively) are illustrated on the hysteresis curve in figure 8.10:3. The material which best fits this description and yet is commercially available, is sintered Samarium-Cobalt. Magnets made of this material are capable of producing large magnetic inductances, but are not easily demagnetised. However, the field produced by any example depends on the shape and magnetic environment of the sample, since it is this that determines the point on the demagnetisation curve relevant to a given magnet[1]. It was therefore not

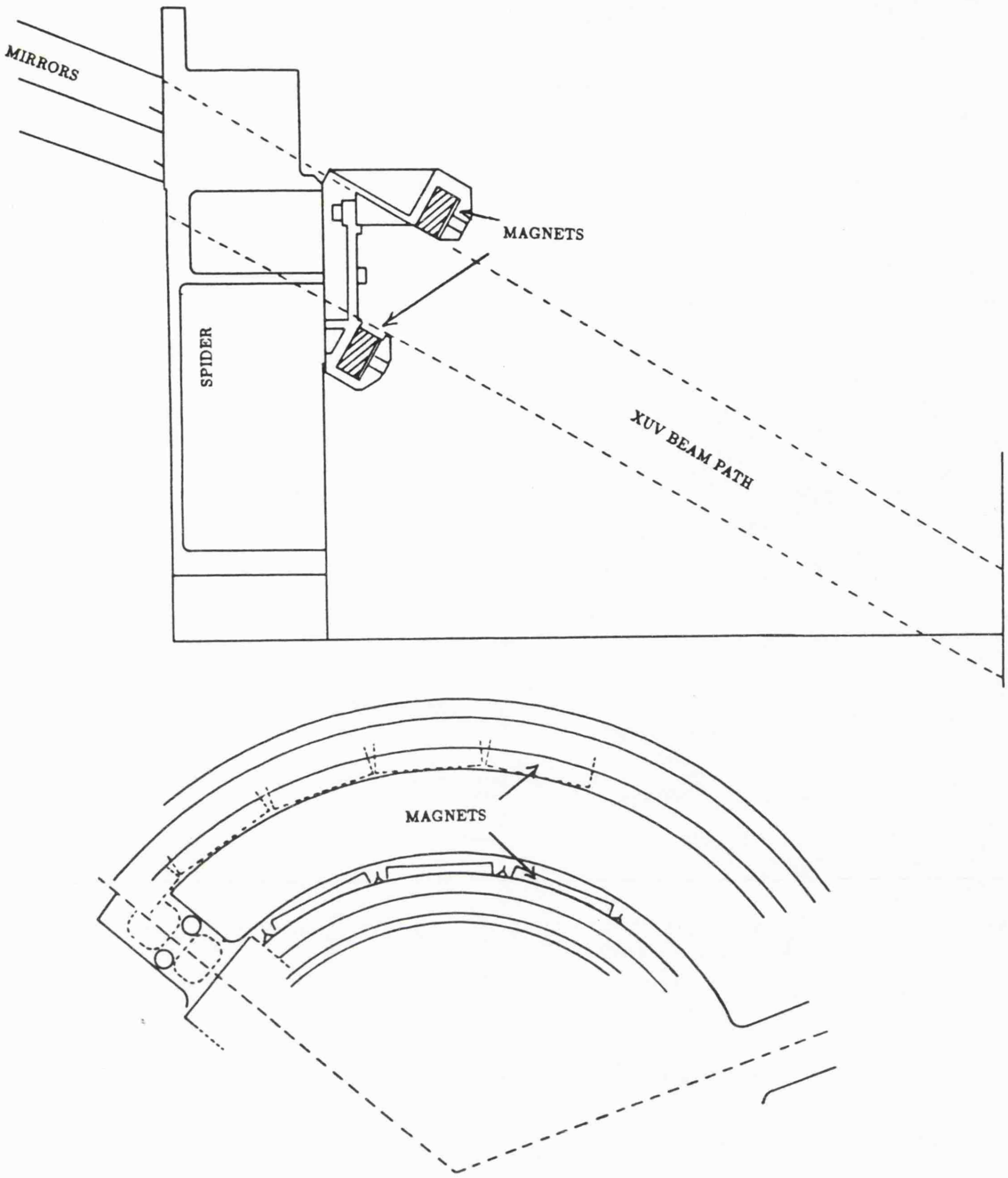

Figure 8.10:1 Diagram of the magnetic diverter structure showing its approximate position with respect to the mirrors and focal plane, and the positions of magnets in each ring.

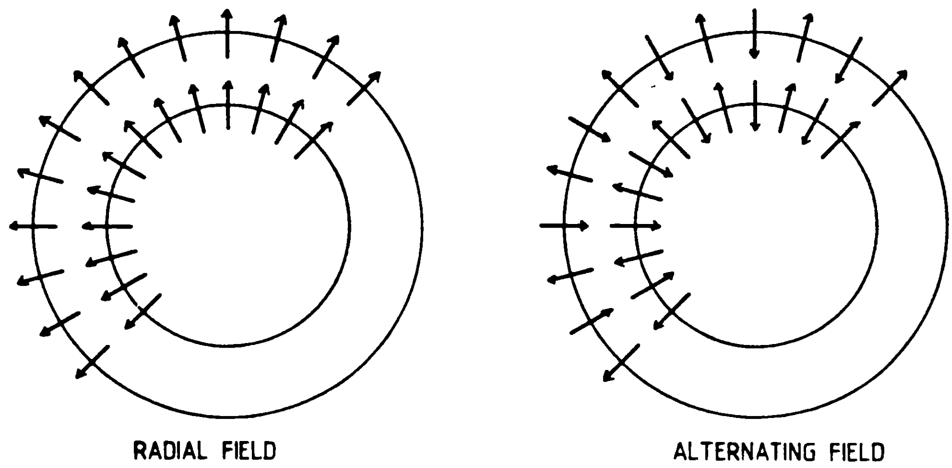

Figure 8.10:2 The two competing magnet orientations considered at ICST and Leicester.

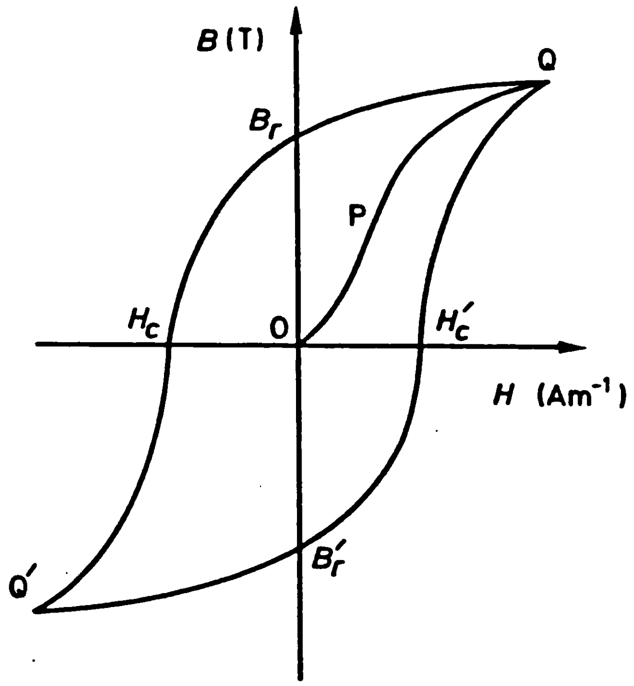

Figure 8.10:3 A hysteresis curve typical of a ferromagnetic material; the remnance, B_r, and the coercive force, H_c, are indicated in the demagnetisation quadrant of the curve. From reference 16.

possible to determine in advance the final magnitude of the deflector field, so all simulation work was done using a representative field initially.

Using Samarium-Cobalt magnets does have disadvantages, particularly where they are to be used in vacuo and in close proximity to items which are sensitive to contamination, as is the case with the mirror assembly. The threat of contamination stems from the porosity of sintered materials, in vacuum any contaminants absorbed will be desorbed and may condense on the mirror surfaces reducing their reflectivity. Also Samarium-Cobalt magnets are very brittle, a property which makes securing each magnet in the diverter structure difficult, but which also threatens the magnetic performance of the magnets since cracked magnets lie at a lower BH value on the demagnetisation curve.

8.20 Electron Tracing Through Magnetic Fields.

When finalising the design of the magnetic diverter, it was necessary to have some means of predicting the effect of the diverter field on electron trajectories. One way would have been to construct a model of the diverter using a set of representative magnets, and then performing tests using an electron gun in a suitable vacuum tank. This approach was not considered because of the high cost and the engineering effort involved, instead it was decided to produce a computer model of the field and assess the effect on electrons using a ray-tracing routine.

The following subsections outline this approach.

8.21 Model of the Magnetic field.

Of the two cases illustrated in figure 8.10:2, of 'radial' or 'opposed' magnet arrangements, the radial case was analysed at Leicester and the opposed case was investigated at ICST. In adopting a mathematical description of the magnetic field it was necessary to compromise between precision and speed of computation. Clearly, if electrons are to be traced through a magnetic field then the field must be known, at least within a given limit of precision, at all points along the trajectory, and this could mean many separate field calculations.

Instead of adopting a descrete dipole approximation to the field, it was found to be quicker to model the field using current loops by the Biot-Savart law:

$$\mathbf{B}(\mathbf{r}) = \frac{\mu_o I}{4\pi} \oint \frac{d\mathbf{l}' \times (\mathbf{r} - \mathbf{r}')}{|\mathbf{r} - \mathbf{r}'|^3} \qquad 8.21:1$$

where $\mathbf{B}$ is the magnetic induction at position vector $\mathbf{r}$, due to a current element $d\mathbf{l}'$ at $\mathbf{r}'$.

Figure 8.21:1 shows schematically, the arrangement of current loops used to represent the system of permanent magnets, they are labelled 1–4. The V-shaped feature represents the XUV beam line from

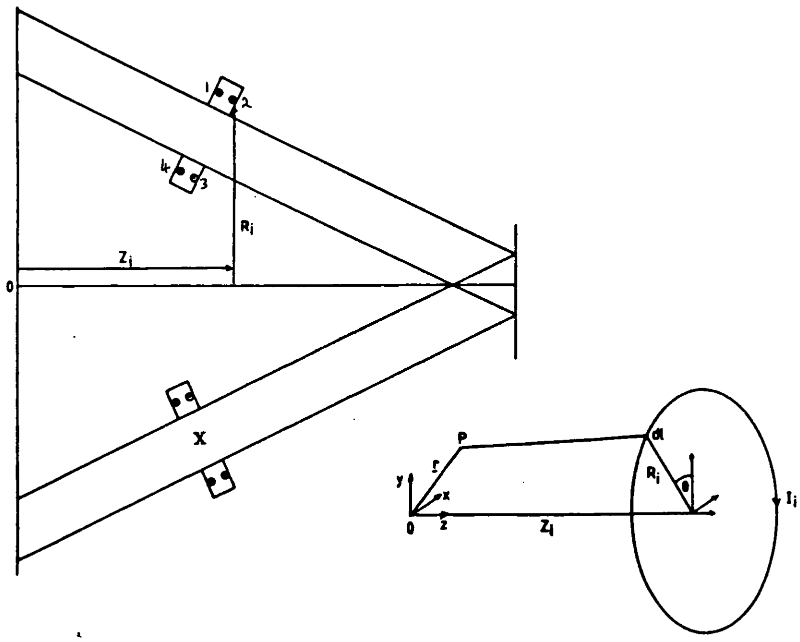

Figure 8.21:1 Schematic of the current loop arrangement used to simulate the field due to the diverter magnets.

the mirrors converging on the detector. Equation 8.21:1 can then be expanded and summed over the four loops to give the field due to the diverter as:

$$B_x(r,z)=\sum_{i=1}^{4}\frac{\mu_o I_i}{4\pi}\int_0^{\pi}\frac{R_i(z-Z_i)cos\theta d\theta}{(r^2+z^2+R_i^2+Z_i^2-2(rR_icos\theta+zZ_i))^{3/2}}$$

$$B_y(r,z)=0 \qquad 8.21:2$$

$$B_z(r,z)=\sum_{i=1}^{4}\frac{\mu_o I_i}{4\pi}\int_0^{\pi}\frac{R_i(R_i-rcos\theta)d\theta}{(r^2+z^2+R_i^2+Z_i^2-2(rR_icos\theta+zZ_i))^{3/2}}$$

where: R_i is the radius of the current loop, Z_i is its position along the WFC axis and θ is the angle around the axis (figure 8.21:1). Varying the currents I_i flowing in each loop can be used to reflect a difference in either the size, or the magnetisation, of the inner ring magnets with respect to the outer ring. Initially the values chosen for I_i were somewhat arbitrary, this was because the field being modelled was unknown, it was not until a few sample magnets became available that it was possible to introduce a more realistic figure. Until then, electron tracing was based on a field in the centre of the WFC beam path (point X in figure 8.21:1) of 70 gauss.

8.22 Electron Dynamics.

The electrons under consideration as the prime threat to WFC observing time are in the range 5keV to 100 keV, and towards the high energy limit in particular must be considered as relativistic. For relativistic bodies the momentum is written as:

$$\mathbf{P}=\gamma M_o\mathbf{v} \qquad 8.22:1$$

where γ is the relativistic gamma factor, M_o is the rest mass of the body and $\mathbf{v}$ is its velocity. The force on an electron in a magnetic field is the Lorentz force given by:

$$\mathbf{F}=-e(\mathbf{v}\times\mathbf{B})$$

After a time dT the change in momentum, $d\mathbf{P}$, is then:

$$d\mathbf{P}=\mathbf{F}dT$$

therefore

$$d\mathbf{P}=-e(\mathbf{v}\times\mathbf{B})dT$$

and if dT is sufficiently small then:

$$\mathbf{P}(T + dT) = \mathbf{P}(T) + d\mathbf{P}(T)$$

$$= \mathbf{P}(T) - e(\mathbf{v} \times \mathbf{B})dT \qquad 8.22:2$$

Equation 8.22:2 is the basis of simulating the passage of electrons through a magnetic field. At every point of interest along the electron path, the change in momentum due to the field can be calculated, and from this the change in the electron velocity and hence position can be found. This procedure is repeated every time interval dT, and if this is small, so that the distance moved $V(T)dT$ is small compared with the Larmor radius, then a good approximation to an electron path through the field will be obtained. To make best use of the available computer time it was convenient to make $dT = dT(B)$ so that in regions of high field, where the rate of change of momentum (force) was high, dT was small but in regions of low field dT was large.

Using the procedures outlined above, a set of software was written for the University of Leicester's CDC (Control Data Corporation) Cyber 73 computer, with which to simulate the passage of electrons through a magnetic field modelled on that produced by the WFC electron diverter.

It has already been stated that the details of electron propogation through the mirror system is poorly understood, and that this meant that the electron distribution (both energetic and spatial) was largely unknown. To put some limit on the input parameters for the electron trajectories to be considered, it was decided to use the extremes of the spread in possible XUV input angles derived by Dr. R. Willingale from XUV ray-tracing[2]. These limits were ± 13 degrees in the tangential sense indicated in figure 8.20:1, and ± 5 degrees in the radial sense.

Electrons with the above spread in input angles were traced from the focal plane side of the mirrors, until they either reached the focal plane or else were further than 1m from the detector and so beyond the influence of the magnetic field. Several possible forms of output were possible, for example it was instructive to plot out the projection of electron trajectories onto one of the planes in the WFC as in figure 8.20:2.

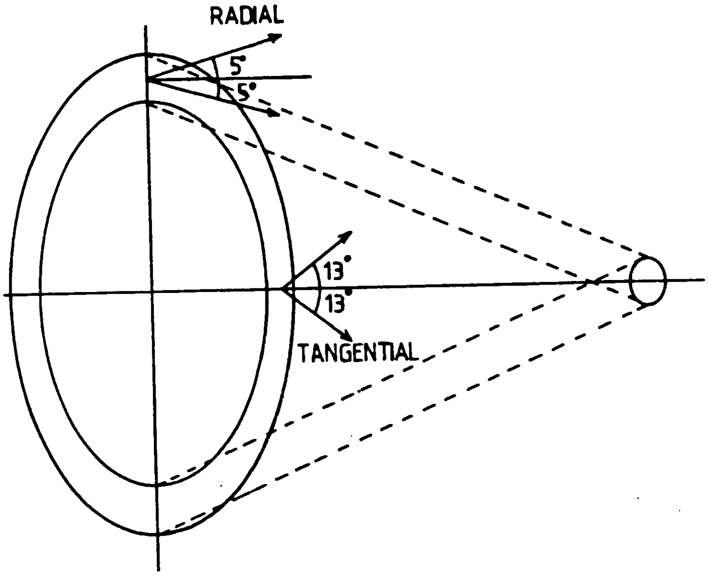

Figure 8.20:1 The limits of the electron tracing trajectories illustrated with respect to the mirrors.

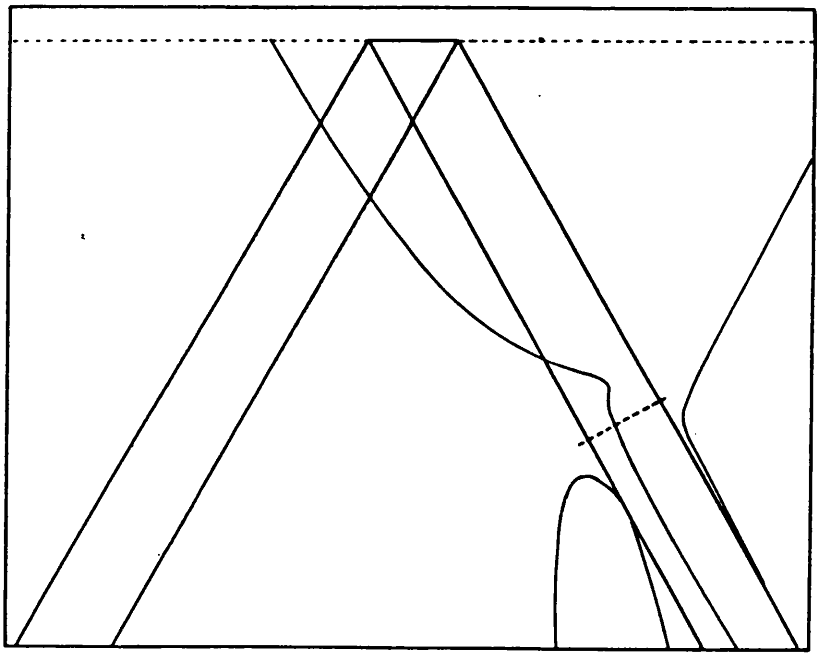

Figure 8.20:2 A plot of typical electron paths in the diverter field.

8.30 Checks on the Accuracy of the Tracing Routine.

One of the major difficulties with a Monte Carlo program is that of verifying the results produced. Several checks were therefore performed on the the field generating routine and the tracing routine to confirm their accuracy.

The equations 8.21:2 form the basis of the field generating routine, but it can be seen that they contain integrals which under most circumstances cannot be evaluated analytically. However, when the point of interest corresponds with the centre of one of the current loops, then the field at that point due to the loop is easily calculable. Using the field routine to supply the field at the centre of each loop therefore provided a useful diagnostic tool.

Checks on the general form and symmetry of the field were provided by plotting the magnitude of the field along lines in the WFC, for example the principal axis (figure 8.30:1), and by plotting contours of constant field strength in various planes (figure 8.30:2). In figure 8.30:2 the pair of straight lines represents the XUV beam path while the curved lines are contours of constant magnetic induction showing the density of field lines.

The tracing program itself was checked by tracing particles through a region of well defined, constant, field and by comparing the result with that calculated from the simple theory of charged particle motion in magnetic fields. It was found that good agreement could be obtained if the time increment was chosen appropriately.

With this in mind, a single electron was traced through the real diverter field from identical starting positions, several times. Each time, the time increment was shorter until the point was reached where further decreasing the time interval no longer effected the final position of the traced particle. It was thus possible to be confident that electrons could be reliably traced through the field generated by the current model, however, the accuracy with which this approximation represented the field due to an assembly of permanent magnets was not established. This will be discussed in section 8.40

8.40 Prototype Diverter.

The basic diverter design has been presented, but the details quoted were specific to what was in effect a developement model and for a prototype assembly to be produced several small modifications were necessary. In particular, the numbers of magnets in each ring was increased and their sizes reduced because the manufacturer (Preformations Ltd) found that the larger magnets were difficult to produce free from cracks. It was also found to be necessary to move the diverter about 20mm away from the rear of the mirrors to allow access for metrological instruments during WFC assembly. These changes,

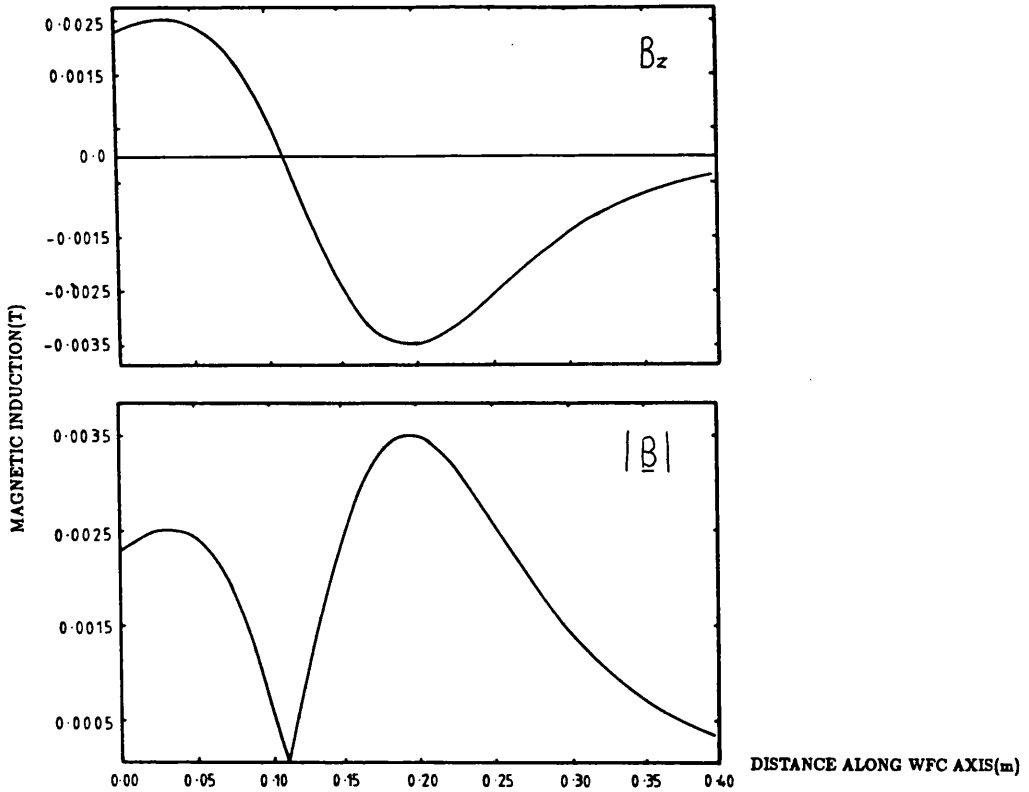

Figure 8.30:1 Plots of a single field component, and of the total field, against position along the diverter axis.

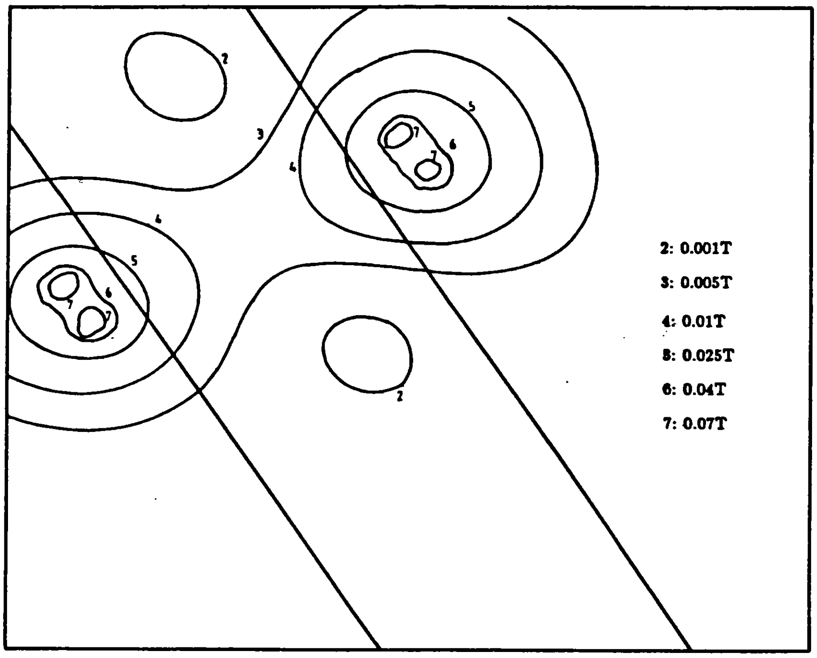

Figure 8.30:2 Contours of constant magnetic induction in relation to the XUV beam path (straight lines).

although likely to result in some shortfall in diverter performance, are small enough not to significantly alter any conclusions arrived at, as a result of the simulations carried out at Leicester using the original configuration.

The validity of the electron tracing simulations depends on the ability to accurately model the magnetic field due to the assembly of magnets, so when a set of sample magnets became available field measurements were made to allow comparison with the model. Figure 8.40:1 shows figures supplied by Alan Entwistle of ICST and predicted fields for the region of strongest field in the WFC beam path.

The field measurements are denoted in figure 8.40:1 by ICST and the error bars indicated show the field variation around the magnet rings due to the discrete nature of the magnets. The lines labelled Case 1–4, illustrate values obtained from the field model under various current loop conditions. The magnitudes of the currents used to represent each ring of magnets were adjusted to reflect the differing quantities of magnetic material in each ring. Differing loop separations were also used to simulate the departure of permanent magnets from ideal dipoles, particularly at their ends.

Case 1 is the situation which is closest to the measurements and is the configuation used in all electron tracing, though normalised to an arbitrary central field of 70 gauss compared with closer to 300 gauss as indicated by measurement. This apparent anomoly is in fact insignificant since all tracing results can be scaled to a different central field by scaling the electron energy accordingly. This can be seen by considering an element of electron path through a region in which the field is made constant by chosing a sufficiently small increment in distance travelled (figure 8.40:2). The path length through the region is given by:

$$dl = r d\theta$$

where r is the radius of the electron path:

$$r = \frac{\gamma M_o v}{eB} = dl/d\theta$$

hence:

$$\int_p B dl = \int \frac{E}{ec}\sqrt{\left(1 - \left(\frac{M_o c^2}{E}\right)^2\right)} d\theta = \frac{E}{ec}\sqrt{\left(1 - \left(\frac{M_o c^2}{E}\right)^2\right)}\theta$$

where the integral is over the electron path and θ is the angle of deflection with respect to the initial electron trajectory. The last equation gives the deflection of an electron of energy E on travelling a path p through a field B, but the quantity

$$\frac{E}{ec}\sqrt{\left(1 - \left(\frac{M_o c^2}{E}\right)^2\right)}$$

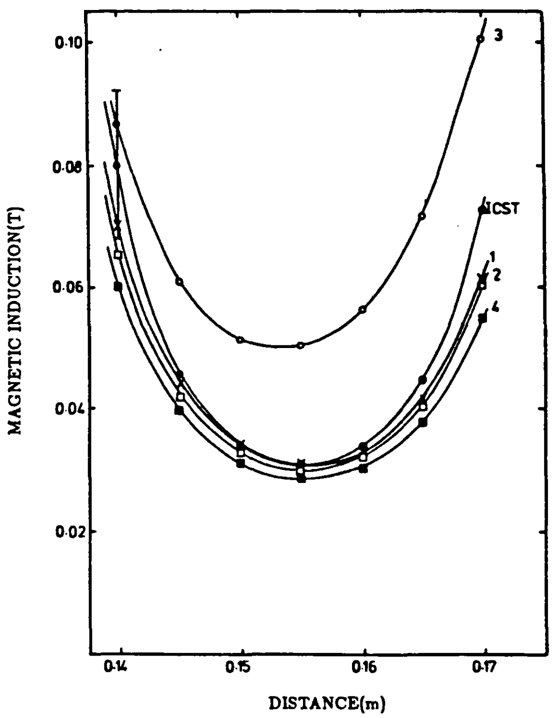

Figure 8.40:1 Predicted diverter fields (cases 1–4) compared with measued values supplied by Alan Entwistle of ICST.

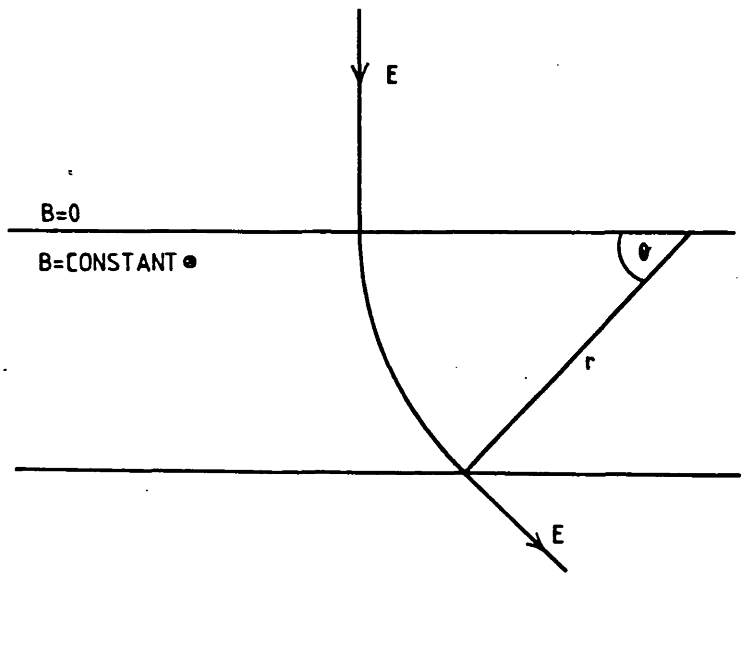

Figure 8.40:2 The deflection of an electron on passing through a region of constant field.

is independent of p so that an electron of energy E' will travel the same path p in a field kB, where k is a constant, if:

$$\int_p kBdl = \frac{E'}{ec}\sqrt{\left(1 - \left(\frac{M_o c^2}{E'}\right)^2\right)}$$

this gives,

$$E'\sqrt{\left(1 - \left(\frac{M_o c^2}{E'}\right)^2\right)} = kE\sqrt{\left(1 - \left(\frac{M_o c^2}{E}\right)^2\right)}$$

and so:

$$E' = \sqrt{(k^2(E^2 - M_o^2 c^4) + M_o^2 c^4)} \qquad 8.40:2$$

This allows a scaling of results obtained at a field normalised to 70 gauss and electron energy E to any other field value, as long as the form of the field is preserved. This is illustrated in figure 8.40:3, which is a plot of field integral vs. energy and shows how the field normalisation scales the electron energy. The value of 70 gauss was a relic of previous attempts at establishing the field in the beam gap, and it was decided to keep to this value to allow comparison between the older field configurations and that finally adopted.

8.50 Electron Tracing Results.

Figures 8.50:1 and 8.50:2 show the effect of tracing the trajectories of 200 monoenergetic electrons through the diverter field. The input trajectories cover the range available to XUV photons reflected from the mirrors, as discussed in section 8.22, the starting points of these trajectories are distributed along a line running radially across the rear of the mirrors and is indicated by a heavy line. In the figures, crosses represent the points where the input trajectories intersect the focal plane, the small circle denoting the MCP detector, and the dots show the points of impact of deflected electrons.

It can be seen from these data that the overall pattern of electron deflection is a movement of the centroid of the distribution in the direction implied by the average direction of the magnetic field, together with some scattering in arbitrary directions. It is also clear that even at 10keV, a 70 gauss field is not able to exclude all electrons from the detector. Those electrons which did hit the detector were identified with those whose initial (undeflected) positions were furthest from the detector in the direction oposite to the deflection direction, ie. those at the extreme of the ± 13 degree distribution.

This 'leaking' of the extreme of the electron distribution into the detector was expected, afterall the action of the diverter is simply to divert, and with an isotropic distribution of electron trajectories as many electrons could be deflected towards as away from the detector. The situation in the WFC is not so extreme. Even were the electron distribution isotropic some improvement in count rate might

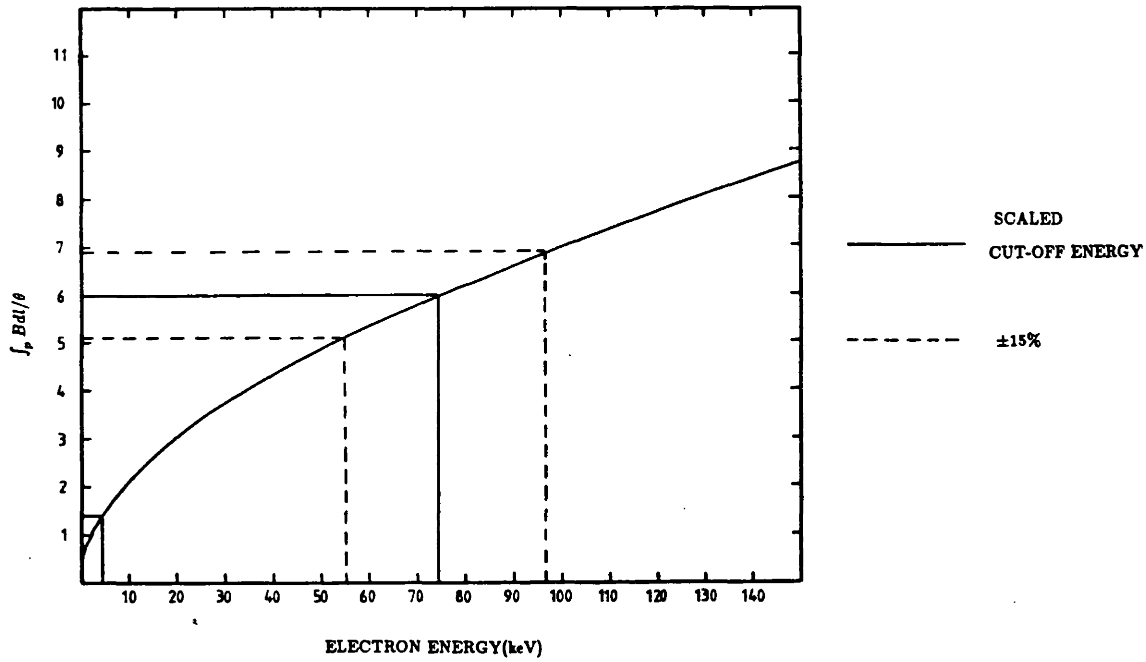

Figure 8.40:3 **A plot of** $\int_p Bdl/\theta$ **vs. electron energy.**

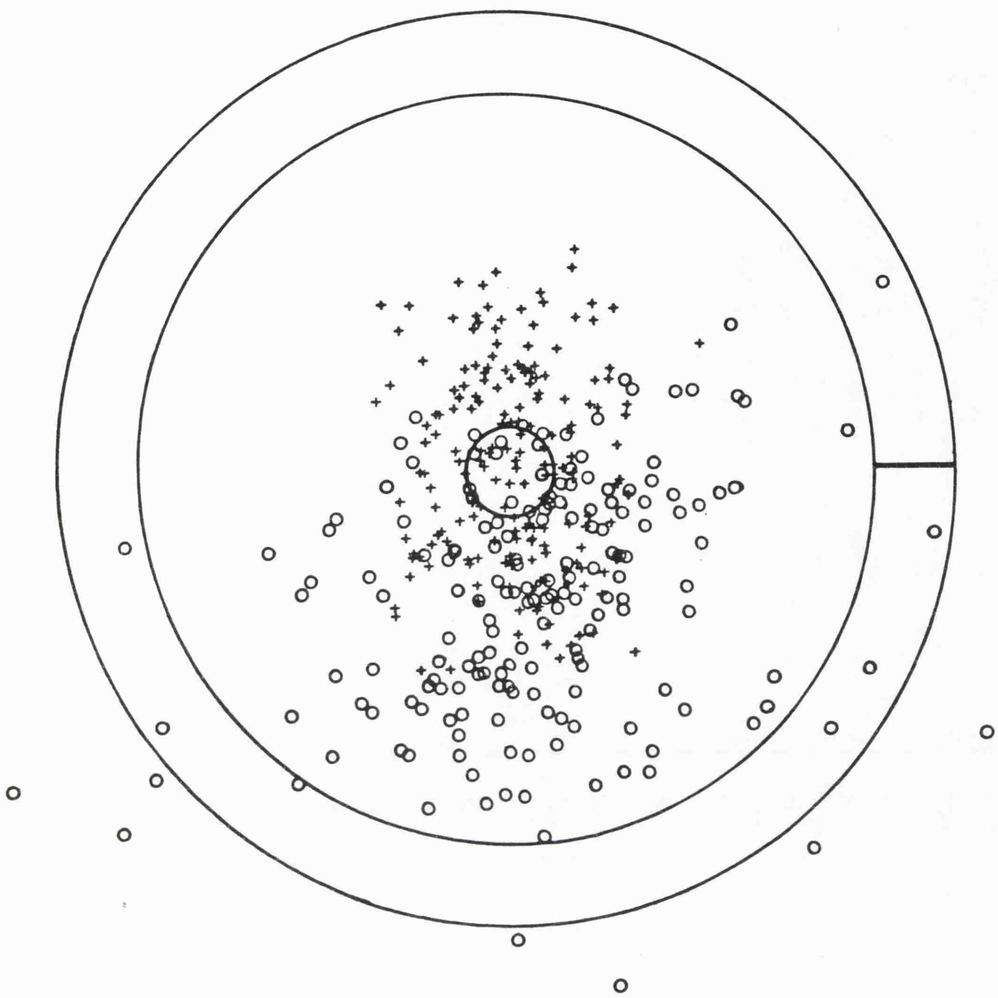

Figure 8.50:1 The effect of tracing 200 25keV electrons through the diverter with field normalised to 70 gauss. The crosses represent the undeflected impact points of the electrons in the focal plane, and the small circles the deflected impact points. The two larger circles depict the focal plane side of the mirror nest with the heavy line indicating the electron injection line; the smaller circle represents the MCP detector in the focal plane.

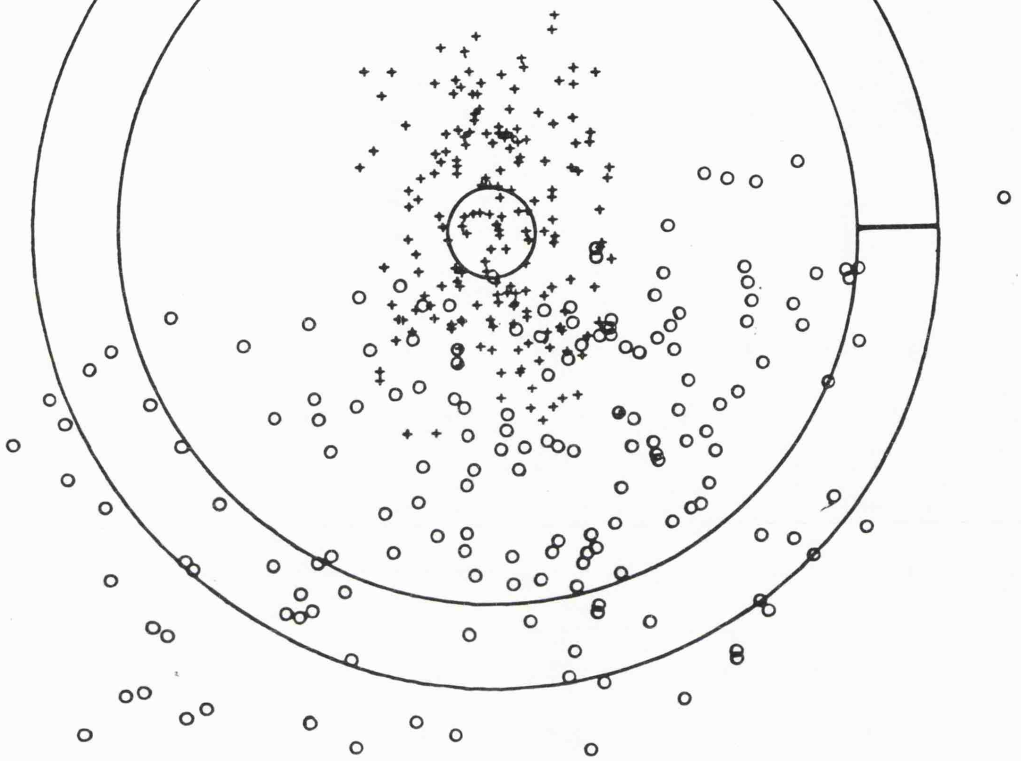

Figure 8.50:2 The effect of tracing 200 10keV electrons through the diverter with field normalised to 70 gauss. The crosses represent the undeflected impact points of the electrons in the focal plane, and the small circles the deflected impact points. The two larger circles depict the focal plane side of the mirror nest with the heavy line indicating the electron injection line; the smaller circle represents the MCP detector in the focal plane.

be expected, as many electrons would undergo collisions with the telescope structure resulting in their elimination from the distribution. It is true, however, that any magnetic diverter depends to a large extent on the mirrors confining the electron distribution to be within some limit, and any performance figures must take this limit into account.

Having identified the troublesome component it was possible to concentrate on it, so that a figure for the cut-off energy could be established. Consequently, a series of electron energies was considered and the extreme +13 degree component of the assumed distribution was traced through the diverter field. Figure 8.50:3 shows the result of superposing the deflected distributions, and the solid lines through them illustrate the extent of the deflection. Twenty trajectories were traced for 3, 5, and 10keV, and single particle deflections are indicated for 25 and 45keV. When these data are transfered to a plot of deflection vs. energy it is simple to determine the 13 degree cut-off energy, as in figure 8.50:4, and for a 70 gauss field this figure is approximately 4.5keV. Having obtained the cut-off energy at the arbitrary field of 70 gauss, equation 8.40:2 allows a figure to be calculated for the more realistic field of 300 gauss suggested by field measurements (figure 8.40:1). This gives a 13 degree cut-off energy of 77keV for 300 gauss.

8.51 Limitations of Computer Simulation as a means of Assessing Diverter Performance.

The technique outlined above for determining the response of a magnetic electron screen to electrons in the energy range 10–100 keV has several limitations, the largest steming from the fact that an axially symmetric model was adopted for a field generated by discrete permanent magnets.

It can be seen from figure 8.40:1 that a realistic field could have variations of the order of ±15% around the region of maximum field in the XUV beam path. The consequences of this in terms of 13 degree cut-off energy can by assessed by referring to figure 8.40:2. By considering a cut-off energy of 77 keV, the corresponding path integral constant has a value of 6 (arbitrary units) and so a range of ±15% leads to a ±20keV variation in the cut-off around the magnet ring. This assumes, however, that the field remains broadly similar to that generated by the current loop model, an assumption that is probably not valid in regions opposite the gaps between magnets as field gradients will certainly be introduced.

Another shortcomming of the approach taken was that no account was taken of scattering or electron absorption by elements of the WFC structure. This was partly due to the limited time available, but it was also felt that this additional factor might obscure the influence of the diverter itself on the electron background. For this reason these preliminary studies also did not consider the effect of adding electron baffles to the model to improve the exclusion efficiency.

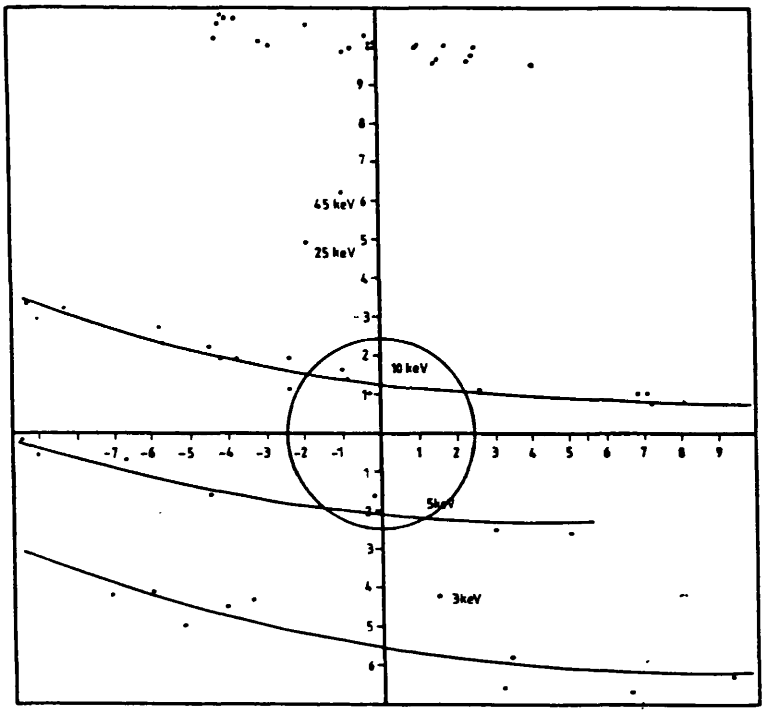

Figure 8.50:3 Deflection of the +13° component of the electron distribution, at several energies, with respect to the MCP detector. Solid lines indicate the extent of the deflection.

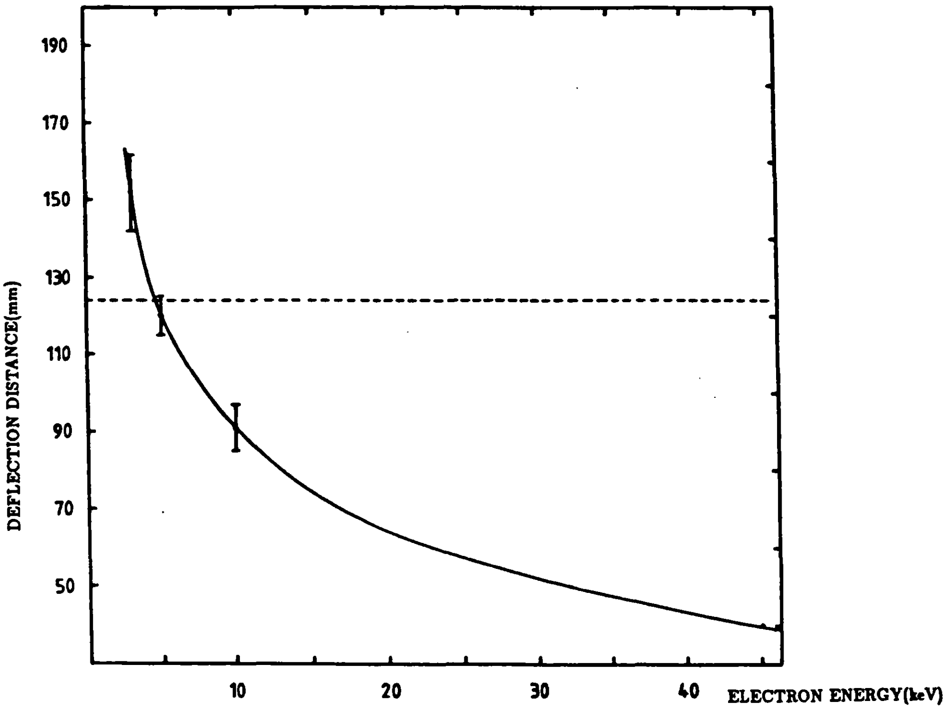

Figure 8.50:4 A plot of deflection distance in the focal plane against electron energy. The cut-off energy for the +13° component is indicated.

Although the analysis presented so far does demonstrate that electrons in the problem energy band can be deflected sufficiently to avoid the detector, no transmission figure is provided. This would be obtained if a large enough number of electrons were traced through the field with a sufficiently wide cross-section of the available starting trajectories considered. However, the amount of time required to do this rendered it impracticable for this study but this approach was undertaken at ICST, both for the alternating and the radial case.

Data provided by ICST[3] shows some difference between the transmission of the two configurations. Although both are small, less than 3%, the radial case seems to transmit more than the alternating case. The radial configuration does, however, offer the advantage of deflecting particles in an easily understood manner rather than scattering them, provided the field is reasonably free of the 'holes' introduced by the discrete magnets. It is therefore easier to see how the divertor will respond at energies for which there is no tracing data.

Ultimately, the only way to assess the performance of the magnetic screen, and to decide between the configurations, was to instigate an experimental investigation. Some preliminary work along these lines has been done at Leicester by Dr. M. Sims[4], using the MTF.

8.60 Magnetic Diverter Electron Beam Tests.

The scheme adopted with which to test the magnetic diverter involved use of the Mirror Test Facility, which was discussed in chapter 6. The tank designed to hold the WFC mirrors under XUV test, was found to be a good approximation in geometry to the WFC itself as it is capable of holding mirrors, diverter and detector in their appropriate positions. In addition, an unused vacuum port was available in a position suitable for installing an electron gun to simulate the electron flux incident on the mirror aperture.

Figure 8.60:1 shows schematically the test configuration adopted. The relative positions of the various components is illustrated, and the positions of electron baffles are indicated. Electron baffles were included as a result of work done at ICST which demonstrated that they provide surfaces upon which deflected electrons may be absorbed, also in these tests they represented parts of the WFC structure which are close to the XUV beam path.

The electron gun proved troublesome in that no suitable 'off the shelf' item could be found. Most commercially manufactured guns produce a high current (microamps to milliamps) focused beam, whereas the requirement for the diverter test were the exact opposite of this, ie. low current of the order of 10^{-16}Amps with a beam divergence of several degrees. To meet these specifications a gun had to be

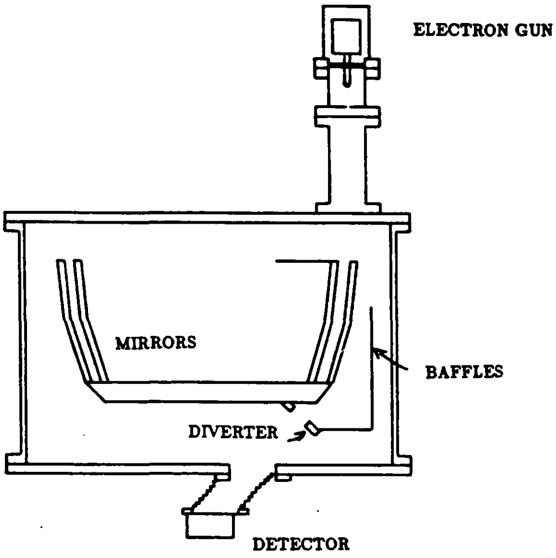

Figure 8.60:1 Electron beam test configuration showing: the mirror tank, dumby mirrors, diverter, baffles, electron gun, and detector. From reference 5.

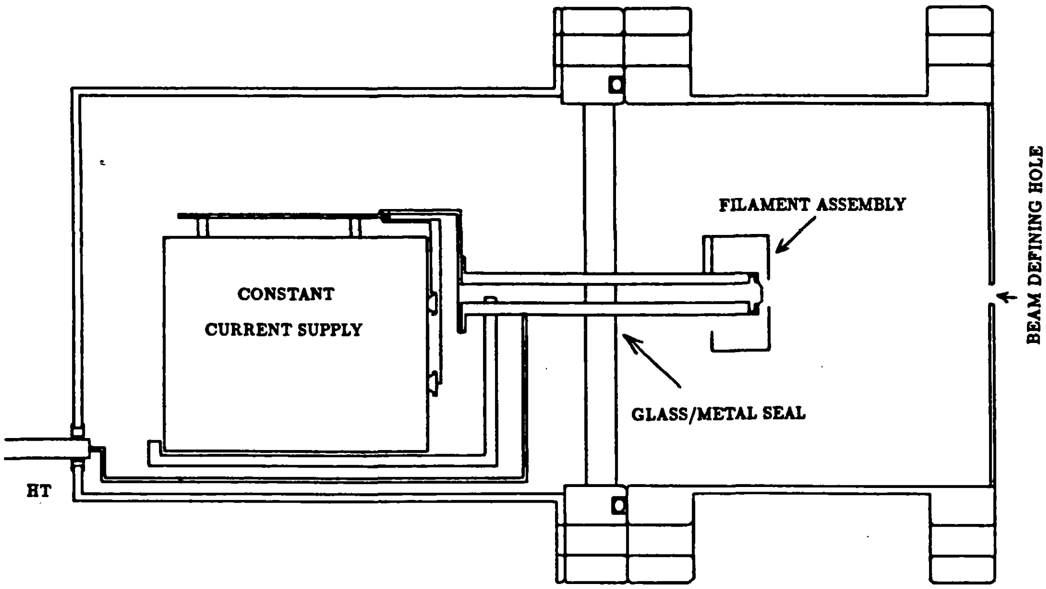

Figure 8.60:2 Section through the electron gun.

designed in house. Figure 8.60:2 shows a section through the resulting electron gun illustrating its principal components, ie. a tungsten filament with battery powered constant current supply, a glass-to-metal sealed high vacuum feed-through, and a molybdenum earthed plane with beam defining hole. The energy of the emerging electron beam is determined by the HT voltage existing between the filament and the earthed plane.

The requirement for a diverging beam was, of course, because the gun flux was intended to simulated the more or less isotropic electron distribution expected in orbit. A low electron current, on the other hand, was a consequence of the high detection efficiency of MCP detectors[5] and their sensitivity to high count rates.

Figure 8.60:3 is a photograph of the mirrors and diverter structure in the mirror tank, taken from the direction of the detector. The use of the diverter structure without magnets was a method of confirming that any changes in count rate were due to the magnetic field and not just to the magnet supports occulting the beam or scattering electrons into the beam.

Having initially established the optimum filament current for the electron gun by adjusting the current until a count rate of $1000\mathrm{s}^{-1}$ was measured by the detector without the mirrors installed, the detector count rate was measured. with the mirrors in position but without the diverter. The count rate was next recorded with the mirrors and diverter structure present, and finally the rate with mirrors, structure and magnets was measured. Energies of 10, 15, and 22 keV were used for these measurements, and some were made at 25 keV although high voltage breakdown prevented a complete data set being obtained here.

Table 8.60:1 has been reproduced from reference[4] and it shows the results obtained. The figures clearly show that the magnetic diverter is an effective screen for electrons in the test energy range, but that there is no clear trend in the transmission figures with energy. If any trend is discernable it is that, contrary to expectation, the diverter deflects more towards higher electron energies.

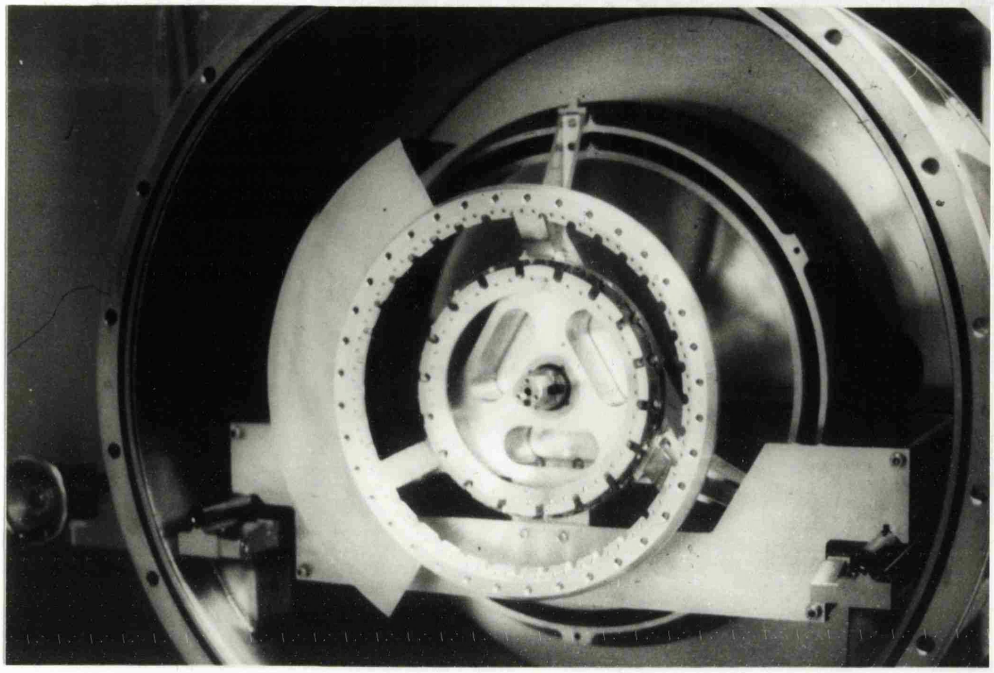

Figure 8.60:3 Photograph of mirrors and diverter structure in the mirror tank. M. Sims.

Electron energy(keV)	Diverter transmission(%)
10	2.23±0.05
15	2.39±0.05
22	2.14±0.07
25	1.56±0.03

Table 8.60:1 Diverter electron test results. From reference 5.

8.61 Limitations of the Electron Beam Tests.

As far as this work is concerned the greatest limitation of the electron beam tests outlind above, is the fact that pressure on the MTF meant that no comparison between the two field configrations was possible. Whilst this is regretable the results do however confirm that the magnetic aproach is a relatively effective way of excluding electrons, at least in the energy range to 25 keV.

As has already been observed, the majority of the electrons to which the WFC will b vulnerable in orbit, lie in the range 10 to 25 keV, and so the fact that the tests were confined to thi range due to the limitations of the electron gun is of little importance, at least as far as deflection of nid-latitude electrons is concerned.

Another area in which the diverter may have been under tested is the distributionof electron trajectories. The divergence of the electron gun beam was of the order of 3.5 degrees, so thedistribution emerging from the mirrors to enter the diverter may differ significantly from that assumedthroughout the computer simulations. In what way the distribution differed is unclear, since althoug the spread in electron directions entering the mirrors was probably smaller that is realistic, the mirros used were essentially unpolised and there were in fact only two of them. Unpolished mirrors would ten to broaden the distribution emerging from the mirrors by enhancing scattering through large angles.

The question of electron distributions might have been resolved had there been enoug movement in the detector position to detect the limits of the beam, or if the electron gun could havebeen moved to vary the input direction. This was, however, beyond the scope of a preliminary test.

The figures quoted in table 8.60:1 are given with an associated error. These errors are lerived from the statistics of event counting and do not appear to take account of possible systematic efects.

Although some care was taken to ensure that electron source variability over short tie scales did not adversly influence results, it was not possible to rule out long period effects. The electon gun was known to be stable to within a few percent over times greater than 20s, but there was noopportunity to compare count rates before and after the mirror tank had been let up to atmospheric pressure and re-evacuated. It is conceivable that some variability with pressure cycling might occur, alsoit is possible that variations may have been experienced when the filament supply battery was changed, something that was necessary after about half an hour of operation.

Most of the points made above are either of little importance, or else only relevant in trying to put the measured transmission into the context of the real WFC in orbit, which would be difficult under most test conditions short of full scale tests on the completed WFC. This course of action is being considered to help decide between the competing magnet orientations. At the time of writing, the altrnating configuration was the baseline for the flight diverter—largely because it is the design which produces the smaller net magnetic moment. It is possible, however, that a hybrid alternative might prove attractive, in which the diverter is divided into sectors, each sector having a radial field but with the field direction alternating between sectors. This might allow a higher mean field while minimising the residual magnetic moment.

8.70 Effect of the Magnetic Diverter on the Electron Background.

Having shown by computer simulation that a magnetic diverter is a workable approach to electron exclusion, and having presented experimental results which confirm this (albeit for a field differing in detail from that considered), it is appropriate to consider the implications for the electron background in the WFC. However, it is first necessary to adopt models for electron propogation through the WFC mirrors, and for the encountered electron spectrum.

To estimate the transmission of the mirrors, it is reasonable to consider the electrons as if they were photons which scatter rather than reflect. This allows the use of the ranges of angles which XUV photons are expected to make with the mirror surfaces. The transmitted fraction will then be that fraction that are scattered into a range of angles which are allowed for XUV photons in order that they be detected.

This scattered fraction must be estimated from scattering probabilities like those measured by Kanter[6]. Kanters data has been summerised by J. Quenby[7] as:

$$F = I \times 4.06S \qquad 8.70:1$$

where F is the flux scattered in the forward direction into solid angle S ($<< 1$)from an incident flux I.

For the front mirror, the range of angles is ± 10 degrees around the mirror surface, and 0–8 degrees perpendicular to the surface, giving a solid angle of 2.4×10^{-2}str. The corresponding figure for the second mirror is 3.2×10^{-2}str. which gives a mirror transmission of:

$$T = AS \times 2.4 \times 10^{-2} \times 3.2 \times 10^{-2} I_o s^{-1}$$

where AS is the area/solid angle product for the WFC mirrors. I_o is the flux incident on the WFC.

Aschenbach et al[8] show data due to Torr for electron fluxes in the range 1–26 keV, which although it doesn't cover the whole of the range of importance for the WFC does cover the range of electron measurements made at Leicester and is likely to provide at least an order of magnitude estimate of I_o. These data give $I_o = 10^3$ for mid-latitudes and 10^6 for the auroral regions. This gives $2s^{-1}$ at mid latitude and $2000s^{-1}$ at high latitude transmitted by the mirrors. A diverter transmission of 2% will therefore result in count rates of .04 and 40 per sec. respectively, assuming a 100% detection efficiency for the MCP.

If data from other sources is considered, as in figure 7.10:3 which included the above estimate of the mirror transmission, then the predicted count rate is high for most orbits. Including the predicted diverter transmission then, in figure 8.70:1, demonstrates the dramatic improvement in count rate. Over most of the two orbits represented, the electron background rate should be below $100s^{-1}$ and only where penetration into the auroral zones occurs should the detector need to be switched off to restrict accumulated count. It is therefore clear that a magnetic diverter is unable to protect the detector when experiencing the high fluxes expected in the auroral zones, but would allow observations to be made outside these areas. Indeed without the diverter it is probable that the detector background would be consistently greater than $200s^{-1}$ telemetry limit.

It should be noted, however, that electron background data is not plentiful and this view of the background may be modified as more, and better, data becomes available.

From work done at ICST, and the study presented in this and the previous chapter, it is apparent that a magnetic screen is a worthwhile addition to the WFC instrument. Although more experimental work needs to be done, particularly in defining the higher energy performance of the diverter and the effect of the mirrors on the electon distribution, computer simulation has proved an effective tool in demonstrating that 5–100keV electrons can be excluded from the detector. However, it is clear that the currently proposed orbit is far from ideal as far as electron background is concerned, and a more equatorial orbit would result in increased observing time, were the provision of ground station facilities to allow this.

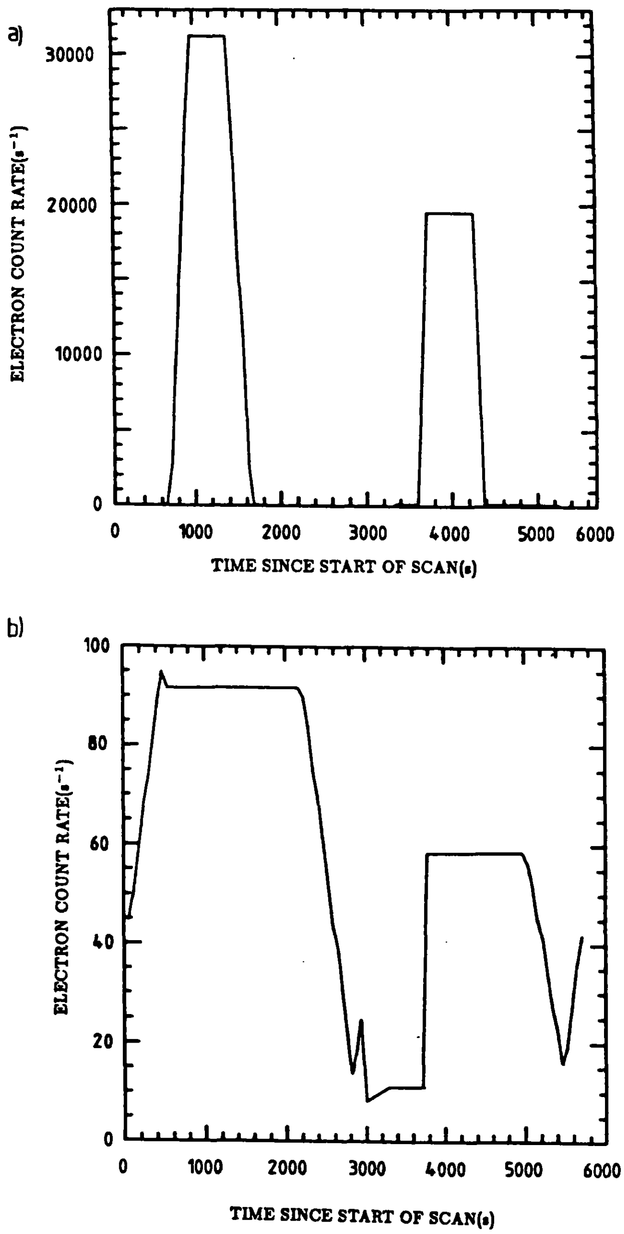

Figure 8.70:1 Predicted 10–50keV electron background with the magnetic diverter in position. Electron background data was supplied by J. Daniels. As in figure 7.10:3, a) is for an orbit penetrating the auroral zones, b) avoids them.

CHAPTER 9

Conclusions and Future Work.

9.10 Conclusions.

This thesis has been concerned with the XUV calibration of the major components of the ROSAT Wide Field Camera and with the reduction of the low energy electron background in orbit. To this end, a brief description of the ROSAT mission has been presented, the WFC has been discussed, and the calibration requirements and electron background problem have been outlined.

Calibration of the WFC mirrors and detectors required the development of an XUV source and monochromator at Leicester. The Penning discharge source used was found to be suitable for the generation of XUV lines in the wavelength range 9–150nm, although observation of short wavelengths required some effort in eliminating stray light in the monochromator. Of most use in the calibration work undertaken so far have been the 13 and 16nm lines due to aluminium, the 25.6, 30.4, and 58.4nm lines from helium, and lines from neon in the 20nm and 40nm wavelength regions.

Using the source and monochromator, quantum efficiency measurements were made on prototype WFC detectors which were in substantial agreement with a published model of CsI coated microchannel plate detectors. The results fill a gap in the published data in the 10–25nm waveband and show that peak detector efficiencies of about 60% are feasible in the middle of the WFC observational range around 13nm.

Reflectivities have been reported on two of the three WFC flight mirrors in the wavelength range 4.5–60nm. It has been shown that the results are within 15% of the values predicted by theory using published optical constants, and that the difference can be attributed to either: low density gold reflecting surfaces, hydrocarbon contamination, or inaccurate optical constants. Scattering by surface roughness was, however, ruled out as the cause of low reflectivity since the the measurement technique involved an imaging detector which indicated scattering much less than that required.

Assuming the remaining mirror proves to be as successful as those tested so far, it is possible to estimate the Wide Field Cameras' on-axis effective area. Figure 9.10:1 shows a plot of effective area vs. wavelength for three representative filter compositions; filter transmissions were calculated using measured absorption data supplied by M. A. Barstow from references 1–6. A more detailed collecting area will be computed when the flight filter compositions have been decided, but figure 9.10:1 is a worthwhile indicator of the instruments on-axis performance as the flight filters will only differ in detail from those considered here.

Low energy electron background has been shown to be potentially a serious threat to WFC observing time, especially because the ROSAT orbit takes the spacecraft into the auroral zones and the principal areas of electron precipitation. Computer simulation of a magnetic electron diverter has shown that this problem can be reduced, particularly at mid latitudes, if the electrons scatter through the mirrors in a reasionably well defined distribution. In addition, electron deflection tests on such a diverter have shown that electrons in the energy range 10–25keV can be excluded from the focal plane detector with an efficiency of about 98%. Without the magnetic diverter the WFC performance would be seriously compromised.

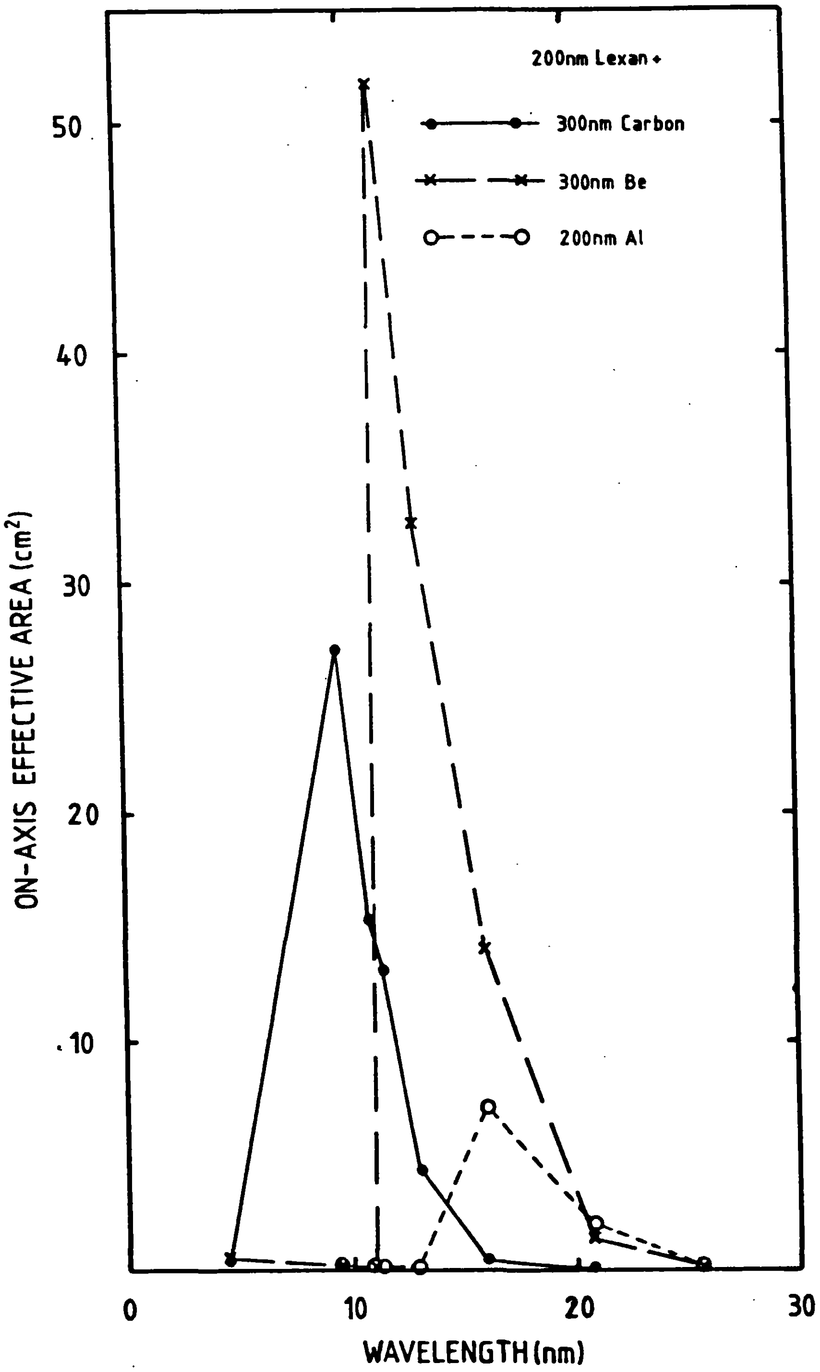

Figure 9.10:1 Plot of estimated WFC effective area calculated using measured mirror and detector efficiencies and filter transmissions calculated from published absorption data.

9.20 Future Work

Although many measurements have been successfully performed using the PS and monochromator they have been rather time consuming, especially when the source is run with argon as discharge gas, because cathode erosion is rapid. Replacing the cathodes involves breaking vacuum and completely dismantling the source for a thorough clean to remove the accumulated aluminium deposites. A redesign of the PS to make this a simpler and quicker proceedure is essential as is an improved RF screen to prevent it from interfering with sensitive electronic equipment.

Other improvements to the PS/monochromator would be worthwhile; for example it is possible that automatic pressure regulation might help to reduce source dependence on the operator by maintaining a constant pressure, and hence current. Adoption of computer control for the monochromator would also be useful as the system could then be operated remotely, instead of by operating switches on the stepper motor controller.

Experimentally much still remains to be done to fully exploit the potential of the source, for example the use of other discharge gases and cathode materials could introduce new lines into the spectrum, particulaly in the 9–12nm wavelength band. Magnesium and calcium are potential cathode materials that would allow the introduction of metal vapours into the discharge, whereas titanium and tungsten are materials which could allow the source to be run without contaminating gas spectra with unwanted strong lines.

Further experimental work is also required on the transfer standard used to calibrate the MCP detectors in efficiency. The current standard CEM needs to be suplimented by a second so that the two can be periodically compared to improve confidence in the stability of their calibration. Also an extension of the work described in this thesis would improve the accuracy of the calibration, particularly in the 10–20nm region, by using a more recently calibrated photodiode in a hydrocarbon free vacuum system. Measurements on the flight WFC detectors would, as a result of these improvements, be a more precise calibration.

The remaining mirror calibrations are essentially a continuation of the work already described. All that remains as far as pencil beam tests at Leicester are concerned, is the reflectivity calibration of the remaining mirror of the nest, M2. Scattering measurements performed on all mirrors will be reported elsewhere.

The final WFC calibrations will be a series of full aperture tests planned to measure the full aperture efficiency of the instrument, on and off axis. These full aperture tests are currently scheduled to be performed in the Panter Facility in Germany early in 1987.

Further work is also required on the magnetic diverter, in particular the electron beam tests performed so far should be extended in energy to at least 100keV (possibly by use of β^- sources) and it is important that an isotropic electron distribution be incident on the mirrors to simulate the electron flux in orbit. Such tests will permit greater confidence in the diverter and will allow more detailed comparisons to be made with the computer simulations performed at Leicester and ICST.

REFERENCES

Chapter 1.

1) B. Aschenbach; Proceedings of RAL Symposium on New Techniques in X-ray and XUV Optics, July 1982. Edited by B. Kent and B. Patchet.1–35
2) H. Wolter; Ann. Phys. 10, 94, 1954.
3) E. Pfefferman and U. Briel; 'X-ray Instrumentation in Astronomy', J. L. Culhane, Editor, Proc. SPIE 597, 146-151(1986).
4) R. Giacconi et al. Apt. J. 230, 540-550 June 1979 and references therein.
5) R. Willingale; Proceedings of RAL Symposium on New Techniques in X-ray and XUV Optics. B. Kent and B. E. Patchet. 124–134
6) A. Wells; 'X-ray Instrumentation in Astronomy', J. L. Culhane, Editor, Proc. SPIE 597, 146-151(1986).
7) G. W. Fraser; NIM 206 (1985b) 265
8) M. A. Barstow et al; Optica Acta 1985 Vol.32, No.2 197-207.

Chapter 2.

1) J. Brand 'A Hollow Cathode EUV-Source for the EXOSAT Program; Performance and Applications', A report from the Cosmic Ray Working Group of the Royal Dutch Academy of Sciences, Huygens Laboratory, Leiden, The Netherlands.
2) D. Srdoc and B. C. Clark; NIM 78 (1970) 307-313.
3) E. Hinnov; Phys. Rev. A; Vol.14, No.4 1976, p.1533.
4) J. R. J. Bennett; IEEE NS-19 part 2 1972 p.78.
5) K. Danzmann et al.; J. Phys. D. Appl. Phys. 18 (1985) 1299-1305.
6) F. M. Penning; Physica, 4, 71, (1937).
7) J. R. J. Bennett; IEEE NS-18 part 2 1971, p. 55.
8) R. D. Deslattes et al.; J. Opt. Soc. Am. 53, p.302 (1963)
9) E. S. Warden and H. W. Moos; Appl. Opt. Vol.16, No.7, p. 1902, 1977.
10) D. S. Finlay et al.; Appl. Opt. Vol.18, No. 5, p. 649, 1979.
11) R. Papoular: 'Electrical Phenomena in Gases'; ILIFFE Books Ltd. London, 1965.
12) S. C. Brown: 'Introduction to Electrical Discharges in Gases'; John Wiley and Sons Inc. 1966.

13) D. Bohm: 'Characteristics of Electrical Discharges in Magnetic Fields' Edited by A. Guthrie and R. K. Wakerling, McGraw-Hill 1949.

14) J. Backus: 'Studies of Cold Cathode Discharges in Magnetic Fields'; J. Appl. Phys. Vol. 30, No. 12, Dec 1959.

15) H. Baumann et al: 'The Emittance and Brightness of Ion Beams from a PIG Ion Source with End Extraction'; IEEE NS-23, No.2 1976, p.1081

16) L. Bex et al. 'Emittance Measurements of High Charge State Argon Beams from a PIG Source'; IEEE NS-23 No. 2, 1976, p.1077

17) J. A. R. Samson 'Techniques of Vacuum Ultraviolet Spectroscopy' John Wiley and Sons. Inc. 1967.

18) R. S. Longhurst 'Geometrical and Physical Optics' Longmann, London 1973, p. 281.

19) T Namioka; J. Opt. Soc. Am. Vol 49, No.5, 1959, p.446

Chapter 3.

1) D. S. Finlay Appl. Opt. Vol.18, No.5 1979 p.649. and E. S. Warden and H. W. Moos Appl. Opt. Vol.16, No.7, p.1902 1977.

2) J. A. R. Samson 'Techniques of Vacuum Ultraviolet Spectroscopy' John Wiley and Sons Inc. 1967.

3) L. B. Lapson and J. G. Timothy Appl. Opt. Vol.15, No.5, 1976, p.1218.

4) J. R. Acton and J. D. Swift: 'Cold Cathode Discharge Tubes', Heywood and Co. Ltd. London 1963.

5) A. Roth 'Vacuum Technology' North-Holland Publishing Co. 1976.

6) R. I. Kelly and I. J. Palumbo: 'Atomic and Ionic Emission Lines Below 2000 Angstroms', US Govt. Printing Office 1973, NRL Report 7599.

7) C. Barat et al. NIM 137 (1976) 559-564.

8) J. Brand 'A Hollow Cathode EUV-Source for the EXOSAT Program; Performance and Applications' Report of the Cosmic ray Working Group, The Royal Dutch Academy of Sciences, Huygens Laboratory, Leiden, The Netherlands.

9) M. A. Barstow Ph.D. Thesis, University of Leicester.

10) J. R. J. Bennett: 'A Review of PIG Sources for Multiply Charged Heavy Ions'; IEEE NS-19 part 2 1972.

11) J. Backus: 'Studies of Cold Cathode Discharges in Magnetic Fields'; J. Appl. Phys. Vol. 30, No. 12, Dec 1959.

12) E. S. Warden and H. W. Moos: 'Penning Discharge as a Photoelectric EUV Spectroscopy Source'; Appl. Opt. Vol. 16, No. 7, July 1977.

13) H. Shulte et al. 'Ion and Electron Flow in Hot-Cathode PIG Sources for Multiply Charged Heavy Ions'; IEEE NS-23, No.2 1976, p.1053.

14) B. H. Wolf: 'Characteristics of a Cold Cathode Type Penning Source and Low Energy Isotope Separation of High Charge States'; IEEE NS-19 No.2 1972, p.74.

Chapter 4.

1) R.W.P. McWhirter 'Review of Methods of Intensity Calibraion in the Spectral Range 10-4000A'; 'New Techniques in Space Astronomy' p 369-385 Ed. Labuker and Lust.

2) E.B. Saloman et al. 'Radiometry using Synchrotron Radiation.' SPIE Vol. 279 Ultraviolet and Vacuum Ultraviolet Systems (1981).

3) M.Kuhne and B.Wende 'Vacuum UV and Soft X-ray Radiometry' J. Phys. E: Sci Instrum. Vol. 18, 1985 p637.

4) L.R.Canfield et al. 'NBS Detector Standards for the Far Ultraviolet' Applied Optics Vol. 12, No.7 July '73 p1611.

5) E.B.Saloman and D.L.Ederer 'Absolute Radiometric Calibration of Detectors Between 200-600A' Applied Optics Vol.14, No.4 April '75 p.1029

6) W.Parkes et al. 'Soft X-ray Studies of Channel Multipliers and Multiplier Arrays.' IEEE Trans. in Nuc. Sci. NS 17 No.3 p.360.

7) L.B.Lapson and J.G.Timothy 'Channel Electron Multipliers: Detection Efficiencies with Opaque MgF2 Photocathodes at XUV Wavelengths.' Applied Optics Vol.15, No.5 May '76 p.1218.

8) J.G.Timothy and R.L.Bybee 'Performance Characteristics of High Conductivity Channel Electron Multipliers.' Rev. Sci. Instrum. 49(8), Aug. '78 p.1128.

9) E.B.Saloman 'Typical Photoefficiency Between 20-250eV of Windowless XUV Photodiodes with Tungsten and Anodized Aluminium Oxide Photocathodes.' Applied Optics Vol. 17 p.1489.

10) Private communication from P.de Korte, via M. Sims.

Chapter 5.

1) R. Willingale, 'The Wide Field Camera Optics for ROSAT.' RAL Symposium on New Techniques in X-ray and XUV Optics. 124–134
2) G. W. Fraser, 'Soft X-ray Detection Efficiency of Coated Microchannel Plates.' Nucl. inst. and Meth. in Phys. Reas. 224(1984)272.
3) J. L. Wiza, 'Microchannel Plate Detectors.' Nuc. Instr. Meth. 162(1979)587-601.
4) Mullard Technical Handbook Part 2 May 1977.
5) M. A. Barstow et al. 'Early Performance Data from the ROSAT XUV Wide Field Camera.' Optica Acta, 1985, Vol. 32, No. 2, 197-207.
6) L. R. Lapson and J. G. Timothy, 'Channel Electron Multipliers: Detection Efficiencies with Opaque MgF2 Photocathodes at XUV Wavelengths.' Applied Optics Vol. 15, No. 5,May 1976, 1218.
7) P. de Korte, Private communication, via G. W. Fraser.
8) C. Martin and S Bowyer, 'Quantum Efficiency of Opaque CsI Photocathodes with Channel Electron Multiplier Arrays in the Extreme and Far Ultraviolet.' Applied Optics Vol. 21, 4206 (1982).
9) G. W. Fraser, 'The Characterisation of Soft X-ray Photocathodes in the Wavelength Band 1-300A: (B) Caesium Iodide and other Insulators of High Photoelectric Yield.' Nucl. Instr. Meths. 206(1983b)265.
10) F. C. Brown et al. Phys. Rev. B 2 (1970) 2126.
11) B. L. Henke et al. Atomic Data and Nuclear Data Tables, Vol.27, No.1, Jan. 1982.

Chapter 6.

1) R. Willingale; 'The Wide Field Camera Optics for ROSAT' Proceedings of the RAL Symposium on New Techniques in X-ray and XUV Optics. 124–134
2) B. Aschenbach; Rep. Prog. Phys. Vol.48, pp. 579-629, 1985.
3) D. Srdoc and B. C. Clark; NIM 78 (1970) 307-313.
4) A. Franks. Sci. Prog., Oxf. (1977) 64, 371–422
5) M. A. Barstow et al. 'X-ray Instrumentation in Astronomy' J. L. Culhane, Editor, Proc. SPIE 597, 352–361.
6) M. A. Barstow et al. Optica Acta Vol. 32, No. 2, 197-207.
7) B. L. Henke et al. Nuclear Data and Atomic Data Tables Vol. 27, No. 1, 1982.
8) H.-J. Hagemann et al. DESY Report No.SR-74/7 May 1974.
9) B. Aschenbach, Rep. Prog. Phys., Vol.48, 577–629, 1985.

10) R. F. Malina and W. Cash; Appl. Opt. Vol. 17, N0. 20,

Chapter 7

1) M. A. Barstow; Ph.D. thesis University of Leicester, 1983, (chapter 1)

2) G. E. Thomas and D. E. Anderson; Planet. Space Sci., Vol. 24, 303-312, 1976.

3) R. R. Meier and P. Mange; Planet. Space Sci., Vol. 18, 803-821, 1970.

4) F. Paresce et al.; Pre-print, University of California, Berkeley

5) S. Chakrabati et al.; Space Research, Vol. 20, 171-174, 1980.

6) J. Daniels; Ph.D. thesis, University of Leicester, in preparation.

7) Whiteley et al.; NIM 224(1984)287

8) H. Kanter Ann. d. Physik.; Vol. 20, 144, 1957.

9) J. Quenby et al.; 'Report on the state of the magnetic diverter design at ICST, June 1984', A report to the WFC consortium.

10) B. Aschenbach et al.; 'Disturbance of the ROSAT telescope by low-energy electrons outside the Van Allen radiation belts.' ROSAT report circulated to the WFC consortium Oct. 1982.

11) G. A. Paulikas; Rev. Geophys. and Space Phys. Vol. 13, No. 5, 1975.

12) G. T. Hill et al. J. Geophys. Res., Vol. 75, 7267, 1970.

13) J. S. Boyd Rev. Geophys. and Space Phys. Vol. 13, No. 5, 1975.

14) M. A. Barstow et al.; Optica Acta, Vol. 32, No. 2, 197-207.

15) M. V. Zombeck; Smithsonian Astrophysical Observatory, Special Report 386.

Chapter 8

1) M. McCaig; 'Permanent Magnets in Theory and Practice.', Pentech 1976.

2) R. Willingale; Private Communication

3) A. Entwistle, T. Sumner, ICST Private Communication.

4) M. Sims; 'Technical Report: Results of STM Magnetic Diverter Testing at Leicester.' Jan.'86 University of Leicester.

5) G. W. Fraser; 'The Electron Detection Efficiency of Microchannel Plates.' NIM Sept' 1982.

6) H. Kanter; Ann. d. Physik 20, 144, 1957.

7) J. Quenby; 'A Note on the Dual need for Magnetic Screening and Low Energy Charged Partical Protection.', WFC Consortium Internal Report, March '83.

8) B. Aschenbach et al; 'Disturbance of the ROSAT telescope by Low Energy Electrons outside the Van Allen Belts.' MPI Report passed to the WFC consortium Oct. '82.

Chapter 9

1) M. A. Barstow, et al., Optica Acta 32(1985)197

2) H.-J. Hagemann, et al., Desy report SR-74/7 May 1974.

3) J. A. R. Samson and R. B. Cairns, Applied Optics. 4(1965)915.

4) M. A. Barstow et al., J. Opt. Am., 73(1983)122D.

5) B. L. Henke et al., Atomic Data, Vol.27, No.1 Jan 1982.

6) P. Shiles et al.,Phys. Rev. B 22(1980)1612.

XUV Calibrations and Electron Background Reduction for the ROSAT Wide Field Camera

S. R. Milward

Abstract

The ROSAT Wide Field Camera (WFC) is an imaging experiment, conducted by a consortium of UK groups, intended to perform the first all sky survey in the XUV wavelength band (6–30nm). As part of the development and flight programmes, XUV calibration and background simulation work has been undertaken at Leicester.

Here, the commissioning and development of an XUV line source and monochromator is described and their use to produce a laboratory detector standard is reported. Subsequent efficiency calibration of a CsI coated prototype WFC Microchannel plate detector is reported and the results shown to be in substantial agreement with a published model of photocathode behaviour. The results fill a gap in the published data between 11.2 and 25.6nm.

Reflectivity measurements on the Wolter-Schwarzschild Type 1 grazing incidence mirrors are reported and compared with the predictions of theory and with published measurements on test flats. Differences between theoretical reflectivities and the empirical results of up to 15% are shown to be consistent with either: low density reflective gold coating, hydrocarbon contamination, or errors in the optical constants assumed for gold. Measurements were found to be broadly in agreement with published results.

In addition to experimental work, the impact of the orbital low energy electron background is assessed on WFC performance and shown to be limiting due to the inclination of the spacecraft orbit. Reduction of this background is shown, by computer simulation, to be feasible by the introduction of a magnetic screen. Preliminary electron beam tests support this view.